2011

ADVANCED STUDIES ON SERIES IMPEDANCE IN WAVEGUIDES WITH AN EMPHASIS ON SOURCE AND TRANSFER IMPEDANCE

Jinghao Liu
University of Kentucky, jinghao.liu@jci.com

ABSTRACT OF DISSERTATION

Jinghao Liu

The Graduate School

University of Kentucky

2011

ADVANCED STUDIES ON SERIES IMPEDANCE IN WAVEGUIDES WITH AN EMPHASIS ON SOURCE AND TRANSFER IMPEDANCE

ABSTRACT OF DISSERTATION

A dissertation submitted in partial fulfillment of the requirements for the degree of Doctor of Philosophy at the University of Kentucky

By

Jinghao Liu

Director: Dr. Tingwen Wu, Professor of Mechanical Engineering
Co-director: Dr. David W. Herrin, Professor of Mechanical Engineering

Lexington, Kentucky

2011

ABSTRACT OF DISSERTATION

ADVANCED STUDIES ON SERIES IMPEDANCE IN WAVEGUIDES WITH AN EMPHASIS ON SOURCE AND TRANSFER IMPEDANCE

Series impedances, including source and transfer impedances, are commonly used to model a variety of noise sources and noise treatment elements in duct systems. Particle velocity is assumed to be constant on the plane where the series impedances are defined. The research reported herein details investigations into measuring source and transfer impedance. Especially, the measurement and prediction of the transfer impedance of micro-perforated panel (MPP) absorbers is considered.

A wave decomposition method for measuring source impedance and source strength was developed that was purely based on acoustic concepts instead of the equivalent circuit analysis. The method developed is a two-load method. However, it is not necessary to know the impedances of either load a priori. The selection of proper loads was investigated via an error analysis, and the results suggested that it was best to choose one resistive and one reactive load.

In addition, a novel type of perforated element was investigated. MPP absorbers are metal or plastic panels with sub-millimeter size holes or slits. In the past, Maa's equation has been used to characterize their performance. However, Maa's equation is only valid for circular perforations. In this research, an inverse method using a nonlinear least square data fitting algorithm was developed to estimate effective parameters that could be used in Maa's theory.

This inverse approach was also used to aid in understanding the effect of dust and fluid contamination on the performance of MPP absorbers. In addition, an approach to enhance the attenuation of MPP absorbers by partitioning the backing cavity was investigated experimentally and numerically. Results indicated that partitioning improved the attenuating of grazing sound waves.

The effect of modifying both the source and transfer impedances on the system response was also studied using the Moebius transformation. It was demonstrated that the Moebius transformation is a mathematical tool that can be employed to aid in determining and understanding the impact of acoustic impedance modifications on a vibro-acoustic system.

KEYWORDS: series impedance, source impedance, transfer impedance, micro-perforated panel absorbers, Moebius transformation

Jinghao Liu

July 11, 2011

ADVANCED STUDIES ON SERIES IMPEDANCE IN WAVEGUIDES WITH AN EMPHASIS ON SOURCE AND TRANSFER IMPEDANCE

By

Jinghao Liu

David W. Herrin
Co-director of Dissertation

Tingwen Wu
Co-director of Dissertation

James M. McDonough
Director of Graduate Studies

July 29, 2011
Date

RULES FOR THE USE OF DISSERTATIONS

Unpublished dissertations submitted for the Doctor's degree and deposited in the University of Kentucky Library are as a rule open for inspection, but are to be used only with due regard to the rights of the authors. Bibliographical references may be noted, but quotations or summaries of parts may be published only with the permission of the author, and with the usual scholarly acknowledgements.

Extensive copying or publication of the dissertation in whole or in part also requires the consent of the Dean of the Graduate School of the University of Kentucky.

DISSERTATION

Jinghao Liu

The Graduate School

University of Kentucky

2011

ADVANCED STUDIES ON SERIES IMPEDANCE IN WAVEGUIDES WITH AN EMPHASIS ON SOURCE AND TRANSFER IMPEDANCE

DISSERTATION

A dissertation submitted in partial fulfillment of the
requirements for the degree of Doctor of Philosophy in the
College of Engineering
at the University of Kentucky

By

Jinghao Liu

Director: Dr. Tingwen Wu, Professor of Mechanical Engineering
Co-director: Dr. David W. Herrin, Professor of Mechanical Engineering

Lexington, Kentucky

2011

ACKNOWLEDGEMENT

I would like to express my deepest gratitude to my mentor, Dr. David W. Herrin, for his guidance, patience, and most importantly, his friendship during my graduate study at University of Kentucky. His advice and support helped me overcome many difficulties and finish this dissertation. He has shown a lot of confidence in me and has helped me grow professionally.

I also want to thank the director of my committee, Dr. Tingwen Wu, for his invaluable insights and support. I would also like to extend my appreciation to my committee members: Dr. Keith Rouch, Dr. John Baker, and Dr. Qiang Ye. I am also grateful to Dr. Jerry Rose for serving as an outside examiner. I also want to thank Dr. Andrew Seybert for his guidance and support during the past few years. He has offered me numerous helpful advices and inspiring discussions.

I want to thank Zeguang Tao and Jun Han, for their kind help, generosity, and friendship. My sincere appreciation also goes to students and scholars that I worked with, Haiping Song, Xin Hua, Limin Zhou, Jiawei Liu, and Srinivasan Ramalingam, who all have made my stay enjoyable.

Most importantly, I dedicate this dissertation to my parents and my wife for their unconditional love and support in every way possible throughout the study, this dissertation and beyond.

TABLE OF CONTENTS

LIST OF TABLES

LIST OF FIGURES

Figure **Page**

CHAPTER 1
INTRODUCTION

1.1 Background

Increasing noise pollution is well-acknowledged as an important hazard to human health. Reducing noise levels is not only a legal restriction but also a major factor in the marketability and competitiveness of industrial products. Meanwhile, the conflict between the need for more powerful equipment and the demand for quieter environments poses a challenging task for noise engineers. To mitigate noise emissions while keeping the equipment powerful and efficient, engineers must understand the principles of noise generation and transmission, and how to apply noise control strategies. (Crocker, 2007, Maling, 2007, Bockhoff, 2007).

Noise control strategies can be classified according to their relationship to noise sources: (1) those that reduce noise and vibration at the source, (2) and those that reduce the noise and vibration in the propagation path. For the first type of approaches, it is possible to reduce noise at the source by reducing the power of the equipment or by redesigning its active components. The second type of approaches reduces noise in its structure-borne and airborne propagation paths by utilizing vibration isolation methods, acoustical enclosures, mufflers and silencers, and reducing radiation efficiency of the radiating surfaces, etc. (Crocker and Ivanov, 1993). Many noise control strategies involve utilizing impedance modification in the sound and vibration energy path. For example, impedance mismatches can be introduced into structures and acoustic waveguides by adding isolators and reactive muffler components, respectively (Fahy, 2001).

In this document, the emphasis will be on reducing noise in waveguides (i.e., mufflers and silencers). Examples include engine exhaust noise, heating, ventilation, and air conditioning (HVAC) noise and fluid induced noise propagation in hydraulic power systems. The energy is produced by a source and is transmitted through a waveguide until it reaches a termination. Sources

include engines, fans, and hydraulic pumps. The waveguide normally consists of straight pipes, and series of muffler and/or silencer components which are intended to either reflect sound back toward the source or absorb the sound. Normally, sound is emitted to the environment through an opening at the termination of the waveguide (Munjal, 1987). Figure 1.1 shows a typical airborne direct path including the source, duct and termination. In the figure, a muffler and a Helmholtz resonator are used to illustrate noise cancelling and absorbing treatments.

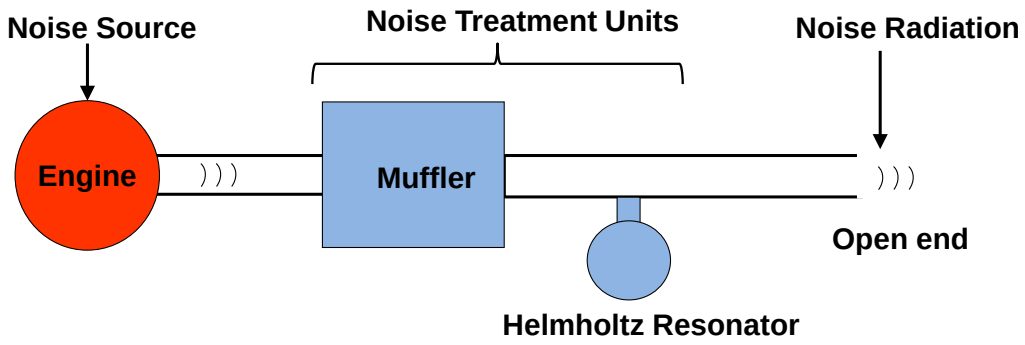

Figure 1.1 A typical source-transmission-radiation path for engine exhaust pipe.

In most case, the boundaries of waveguide models can be simulated by a combination of a source and an impedance. For example, an engine exhaust source can be modeled as a frequency-varying source strength and source impedance. Similarly, a termination can be modeled as an impedance typically denoted as a radiation or termination impedance. Perforated plates or thin layers of absorbing materials divide a waveguide into upstream and downstream sound fields. These sound fields are linked to one another by a transfer impedance.

It is very important for acoustic engineers to be able to model acoustic elements using simplified representations, since computational modeling of these elements can be a formidable task. For example, source characterization of an internal combustion engine based on its thermodynamic processes is difficult. Furthermore, impedance provides a mechanism to model duct elements and acoustic materials.

Each of the aforementioned impedances can be characterized as series impedances because the particle velocity is assumed to constant while there is a sound pressure difference on each side (Munjal, 1987, Melling, 1973). Two types of series impedances, source impedance and transfer impedance, will be reviewed in this dissertation, including their theoretical modeling, measurement techniques and applications (Boden, 1995, Wu, 2003).

The current research is an attempt to investigate the source impedance and transfer impedance as a group, and to improve measurement and modeling of these impedances by utilizing the concepts of series impedance, eventually to apply these impedances to better understand the acoustic performance of the duct system.

1.2 Objectives

The present research focuses on developing new measurement and modeling methods to characterize source impedance and transfer impedance. Specifically, the following objectives were accomplished.

- A new incident wave decomposition method was utilized to model and measure source impedance.
- The transfer impedance was measured by utilizing wave decomposition both upstream and downstream of the sample.
- A process for determining effective parameters of microperforated panel (MPP) absorbers was developed. MPP absorbers are novel acoustical materials that can be modeled as a transfer impedance.
- The influence of modification of both source and transfer impedances on the system response was studied using the Moebius transformation.

1.3 Organization

This dissertation is organized in the following manner. The following chapter reviews the concepts of series and parallel acoustic impedances. Methods for

measuring and modeling series impedance are discussed. Chapter 3 reviews transfer impedance models for ordinary perforated panels and micro-perforated panels. The effect of changing the porosity, hole diameter, thickness and backing cavity depth on the transfer impedance of micro-perforated panels is studied.

The main contributions of this work are summarized in Chapters 4, 5, and 6. In Chapter 4, a wave decomposition approach is developed to measure source impedance. This is followed by an examination of the effect of load impedance on the accuracy of the developed approach.

The emphasis in Chapter 5 is on MPP absorbers. The first half of the chapter focuses on how MPP absorbers can be characterized using measurement and theory. A direct single load method based on a series impedance assumption is used to measure transfer impedance of different perforated panels. Then, effective parameters of MPP absorbers are determined using a nonlinear least square data fitting algorithm.

The second half of the chapter examines how MPP absorbers are best installed and utilized in enclosures and silencers. It is demonstrated that partitioning of the adjoining air cavity enhances the absorptive performance. To better understand the physics, the boundary element method (BEM) is used to model the MPP absorber and backing cavity in a sealed enclosure. The measured and BEM results demonstrate that attenuation of grazing sound waves is enhanced by partitioning the backing cavity.

In Chapter 6, a simple optimization approach selecting impedances is demonstrated. It is shown that that the acoustic response will trace a circle in the complex plane for straight line or circular modifications to mechanical or acoustical impedance. This is due to the fact that the equations relating the acoustic response to the modification are in a form consistent with the Moebius transformation. This is demonstrated for series and parallel mechanical and acoustic impedances.

Conclusions and recommendations for future work are discussed in Chapter 7.

CHAPTER 2
REVIEW OF SERIES IMPEDANCES

In vibro-acoustic analysis, considerable research has focused on utilizing simplified representations to model complicated components and structures (Munjal, 1987, Kinsler, 1999). By applying the simplified models, researchers are able to reduce analysis time for quantifying noise transmission from sources to receivers, and for evaluating the effect of different noise reduction measures. Thus, noise reduction strategies can be assessed without resorting to trial-and-error solutions. (Boden and Glav, 2007).

When modeling acoustic problems, the concept of acoustic impedance is often useful for characterizing boundary conditions. This dissertation specifically focuses on the impedances classified as series impedances. This category of impedance is often utilized for simulating the boundary conditions in waveguides. As a preface, the fundamentals of acoustic wave propagation and impedances will be reviewed.

2.1 Acoustic Impedances

2.1.1 Acoustic Wave Equation

Acoustic waves are one of a variety of pressure disturbances that can propagate through a compressible fluid. When a sound wave passes a point in a compressible fluid such as air, the molecules move back and forth in the direction of propagation, producing adjacent regions of compression and expansion. Thus, it introduces momentary changes to the ambient values of the pressure and density (Seybert, 2000). The ambient pressure and density are assumed to be independent of position of the point, i.e. the fluid is assumed to be homogeneous.

The disturbance to the ambient pressure is called the *acoustic pressure*, which is a scalar. The process of compression and expansion also results in motion of the particle of the fluid about the point. The velocity of this motion is called the *particle velocity*, which is a vector. The term *particle* of the fluid means

a volume element large enough to contain millions of molecules so that the fluid may be thought of as a continuous medium, yet small enough that all acoustic variables may be considered nearly constant throughout the volume element (Kinsler, 1999).

In order to formulating the mathematical description of acoustic waves, several assumptions are commonly employed: (1) viscous forces are neglected, the fluid is inviscid; (2) Body forces such as gravity are neglected; (3) fluid properties are homogeneous, isotropic, and perfectly elastic (or obey the Ideal Gas Law); and (4) the acoustic disturbances are small. In most cases of noise control, acoustic variables such as acoustic pressure and particle velocity are much less than the ambient value. The analysis of small disturbances to the ambient state of a fluid is referred to as linear acoustics (Seybert, 2000).

For small (acoustic) changes about the ambient state of an ideal gas, the pressure-density relationship (or *Equation of State*) can be expressed as:

$$p = \left(\frac{\partial P}{\partial \rho}\right)_0 \rho' \tag{2.1.1}$$

where p is the acoustic pressure fluctuation, P is total value of ambient pressure (P_0) and acoustic pressure (p), ρ is the total density of ambient density ρ_0 and density fluctuation ρ'. For adiabatic processes, this relationship can be simplified as:

$$p = c^2 \rho' \tag{2.1.2}$$

where c is the speed of sound.

The conservation of mass principle states that the net rate with which mass flows into a spatially fixed volume through its surface must equal the rate with which the mass within the volume increases. Based on this principle, the *linearized Equation of Continuity* can be obtained as:

$$\frac{\partial \rho'}{\partial t} = -\rho_0 \nabla \cdot u \tag{2.1.3}$$

where t is time, $\nabla \cdot$ is the divergence operator, and u is the particle velocity.

To obtain the equation of motion for a fluid, Newton's second saw is applied to a moving fluid element which contains a specific mass. According to Newton's second law, the mass of a fluid element times its acceleration is equal to the net force acting on that fluid element. By neglecting the viscosity of the fluid, we can write a linearized inviscid force equation, called the *Euler's Equation of motion*, as:

$$\rho_0 \frac{\partial u}{\partial t} = -\nabla p \tag{2.1.4}$$

By eliminating the density fluctuations from the mass conservation equation using the equation of state, we can combine the three linearized equations: *the equation of state, the equation of continuity, and the Euler's equation of motion*, and obtain the acoustic wave equation as (Kinsler, 1999):

$$\nabla^2 p = \frac{1}{c^2} \frac{\partial^2 p}{\partial t^2}. \tag{2.1.5}$$

In most cases, acoustic waves are time-harmonic waves, i.e., continuous waves at a constant frequency ω. The sound pressure p at any point fluctuates sinusoidally with frequency ω:

$$p = \boldsymbol{p} e^{j\omega t} \tag{2.1.6}$$

where $\boldsymbol{p}$ is the complex amplitude of sound pressure fluctuation at any point.

Substituting equation (2.1.6) into equation (2.1.5) yields:

$$\nabla^2 \boldsymbol{p} + k^2 \boldsymbol{p} = 0 \tag{2.1.7}$$

where $k = \omega / c$ is called the wave number. Equation (2.1.7) is called the *Helmholtz equation* for homogeneous media.

For time-harmonic acoustic waves, the relation between particle velocity and acoustic pressure can be obtained from the linearized equation of continuity:

$$\boldsymbol{u} = \frac{1}{j\omega\rho_0} \nabla \boldsymbol{p} \tag{2.1.8}$$

where $\boldsymbol{u}$ is the complex amplitude of the particle velocity.

2.1.2 Specific Acoustic Impedance

Three common boundary conditions for the solution of the Helmholtz equation are classified into either active or passive boundary conditions. Active boundary conditions are those in which either the motion or sound pressure on the boundary is known (Seybert, 2000).

The first type of active boundary condition occurs when the sound pressure is known. If the sound pressure is defined as p_e on the boundary of the fluid, then the appropriate boundary condition is:

$$p = p_e \text{ on } s_1 \tag{2.1.9}$$

This is called a pressure or Dirichlet boundary condition.

The second type of active boundary condition occurs when the normal velocity is known. If the normal particle velocity is defined as u_n on the boundary of the fluid, then the appropriate boundary condition is:

$$\frac{\partial p}{\partial n} = -j\omega\rho_0 u_n \text{ on } s_2 \tag{2.1.10}$$

This is termed a velocity or Neumann boundary condition.

A passive boundary condition occurs when sound reflects from a passive surface, i.e. absorbing material, in contact with the medium. When acoustic waves contact with the surface of the fluid, the amplitude and the phase of the reflected wave relative to the incident wave depends on the *acoustic impedance* of the surface or boundary. Even though the sound pressure and particle velocity are unknown, their relationship can be described by the acoustic impedance. The appropriate boundary condition for known acoustic impedance is:

$$z = \frac{p}{u_n} \text{ or } \frac{\partial p}{\partial n} = -j\omega\rho\frac{1}{z}p \text{ on } s_3 \tag{2.1.11}$$

This termed an impedance or Robin boundary condition.

Similar to Equation (2.1.11), the *specific acoustic impedance* at any point in the acoustic field is defined as the ratio of pressure to the particle velocity (Kinsler, 1999):

$$z = \frac{p}{u} \tag{2.1.12}$$

It is the property of the medium and of the type of wave that is being propagated. The acoustic impedance determines the acoustic interaction between coupled regions of fluid because it indicates the degree of similarity between the acoustic properties of the regions. This determines the degree to which acoustic waves in one region are reflected and transmitted at the interface. It is also used to analyze the interaction between fluid and solid systems in relation to sound absorption, reflection and transmission.

The acoustic impedance is a vector since it is the ratio of acoustic pressure as a scalar and particle velocity as a vector. The direction of impedance is determined by the direction of particle velocity. However, for acoustic waves in a uniform medium with no reflections or other interferences, the acoustic impedance is often called the *characteristic impedance*, since it is the characteristic property of the medium. The characteristic impedance is not directional. For example, the density of air is 1.21 kg/m^3 and the speed of sound is 343 m/s at 20^oC and atmospheric pressure. Thus the characteristic impedance of air is 415 $pa \cdot s/m$ or *rayls*, which is the unit of acoustic impedance established in honor of Lord Rayleigh.

In general, the acoustic impedance is complex since a phase relation exists between pressure and velocity. Its real part is called acoustic resistance, which represents the loss mechanisms an acoustic wave experiences, i.e. converting acoustic energy into heat; whereas its imaginary part is called acoustic reactance, which represents the ability of the medium to store the kinetic energy of the acoustic waves (Fahy, 2001).

2.1.3 Acoustic Impedances in One-Dimensional (1-D) Waveguides

If all the acoustic variables are functions of only one spatial coordinate, the phase of any variable is a constant on any plane perpendicular to this coordinate. Such a wave is called a *plane wave*.

In duct acoustics, the plane wave assumption is desired because once sound pressure and particle velocity are constant across a plane perpendicular to the direction of propagation of the wave; functions of only one coordinate are

required to represent acoustic variables including acoustic impedance (Kinsler, 1999). This simplifies the problem and reduces the analysis time. In order for plane waves to be present, a 1-D waveguide is required. A 1-D waveguide is usually a long duct with rigid walls and a uniform internal cross section. For circular cross-sections, the duct diameter must be smaller than a half wavelength of the maximum analysis frequency (ISO, 1998). In this document, the plane wave assumption is applied to simplify the duct acoustic problems.

If the coordinate system is chosen so that this plane wave propagates along the x axis, the Helmholtz equation reduces to

$$\frac{d^2\boldsymbol{p}}{dx^2} + k^2\boldsymbol{p} = 0 \tag{2.1.13}$$

The complex form of the harmonic solution for the acoustic pressure of a plane wave is:

$$\boldsymbol{p}(x) = \boldsymbol{A}e^{-jkx} + \boldsymbol{B}e^{jkx} \tag{2.1.14}$$

where $\boldsymbol{A}$ and $\boldsymbol{B}$ are the complex amplitudes of the outgoing and reflected waves, respectively. The associated particle velocity can be derived from Equation (2.1.8) as:

$$\boldsymbol{u}(x) = \frac{1}{\rho_0 c}\left(\boldsymbol{A}e^{-jkx} - \boldsymbol{B}e^{jkx}\right) \tag{2.1.15}$$

The acoustic impedance at any given position x is given by:

$$z(x) = \frac{\boldsymbol{p}(x)}{\boldsymbol{u}(x)} = \rho_0 c \cdot \frac{e^{-j2kx} + \dfrac{\boldsymbol{B}}{\boldsymbol{A}}}{e^{-j2kx} - \dfrac{\boldsymbol{B}}{\boldsymbol{A}}} \tag{2.1.16}$$

where the ratio between reflected wave and incident wave

$$\boldsymbol{R} = \frac{\boldsymbol{B}}{\boldsymbol{A}} \tag{2.1.17}$$

is called reflection coefficient. For two positions $x = 0$ and $x = d$ in the 1-D waveguide shown in Figure 2.1, acoustic impedances at these two positions can be expressed as:

$$z(0) = \rho_0 c \cdot \frac{1+\boldsymbol{R}}{1-\boldsymbol{R}} \tag{2.1.18}$$

and

$$z(d) = \rho_0 c \cdot \frac{e^{-j2kd} + \boldsymbol{R}}{e^{-j2kd} - \boldsymbol{R}} \tag{2.1.19}$$

respectively. The relationship between these two acoustic impedances is given as (Fahy, 2001):

$$z(0) = \frac{z(d) + j \tan kd}{1 + z(d) \cdot j \tan kd} \tag{2.1.20}$$

At position $x = d$, a few special boundary conditions can be summarized as:

1. Closed end or rigid termination boundary condition

$$\boldsymbol{u}(d) = 0 \text{ or } z(d) = \infty \text{ at } x = d. \tag{2.1.21}$$

2. Pressure “release” boundary condition

$$\boldsymbol{p}(d) = 0 \text{ or } z(d) = 0 \text{ at } x = d. \tag{2.1.22}$$

3. Anechoic or no reflection boundary condition

$$z(d) = \rho_0 c \text{ at } x = d. \tag{2.1.23}$$

4. Unbaffled open end boundary condition (Kinsler, 1999)

$$z(d) = \rho_0 c\left[(ka)^2 + j(0.6ka)\right] \text{ at } x = d, \text{ for } ka << 1. \tag{2.1.24}$$

where a is the radius of the duct.

5. Baffled open end boundary condition (Kinsler, 1999)

$$z(d) = \rho_0 c\left[\frac{(ka)^2}{2} + j\frac{8ka}{3\pi}\right] \text{ at } x = d, \text{ for } ka << 1. \tag{2.1.25}$$

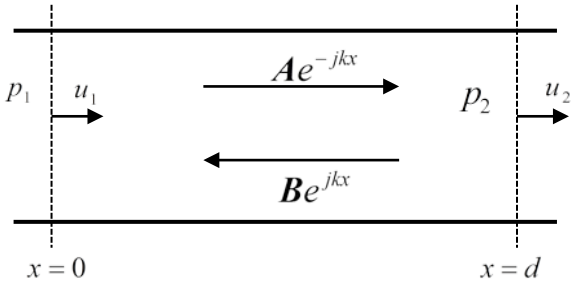

Figure 2.1 Acoustic impedances at two positions in 1-D waveguide.

2.1.4 Series impedance and parallel impedance

Even though the use of specific acoustic impedance to characterize the acoustical behavior of 1-D waveguide is made possible by the plane wave assumption, the concept of the acoustic impedance is more useful when either the sound pressure or particle velocity is discontinuous over a duct cross-section. This occurs when sound waves encounter discontinuities in geometry or fluid properties, like, for example, a sudden area change or a perforated plate.

One type of lumped acoustic impedance is categorized as a parallel impedance or acoustic compliance using an electro-acoustic analogy. Examples of parallel impedance include Helmholtz resonators and quarter wave tubes. A Helmholtz resonator and its electro-acoustic analogy are shown in Figure 2.2.

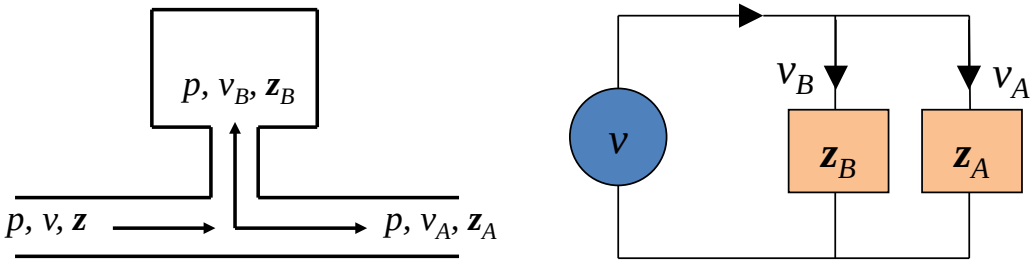

(a) (b)

Figure 2.2 A Helmholtz resonator (a) and its parallel impedance circuit analogy (b).

It is assumed that two or more connected acoustic elements share the same acoustic pressure at the junction while each element has different volume velocity. The volume velocity is related to particle velocity at a surface by

$$v = u \cdot s \tag{2.1.26}$$

where s is the area of the surface.

Assuming that the wavelength is long compared to the extent of the complicated flow pattern near the junction, we can apply the condition of continuity of pressure and obtain

$$p = p_A = p_B \tag{2.1.27}$$

The condition of continuity of volume velocity requires that

$$v = v_A + v_B \tag{2.1.28}$$

Dividing Equation (2.1.28) by (2.1.27) yields

$$\frac{1}{\boldsymbol{z}} = \frac{1}{\boldsymbol{z}_A} + \frac{1}{\boldsymbol{z}_B} \tag{2.1.29}$$

Impedance $\boldsymbol{z}$ in Equation (2.1.29) is defined as pressure divided by volume velocity. It is related to the specific acoustic impedance z at a surface by

$$\boldsymbol{z} = z / s \tag{2.1.30}$$

Another type of lumped acoustic impedance is series impedance or acoustic inertance. It is assumed that the particle velocity is continuous across the element while there exists a sound pressure difference or discontinuity. Thus, the series impedance is defined as the ratio of the pressure difference and the particle velocity. Examples of series impedance include perforated plates and internal engine acoustic impedance (Fahy, 2000, Morse and Ingard, 1987). A perforated plate and its electro-acoustic analogy are shown in Figure 2.3.

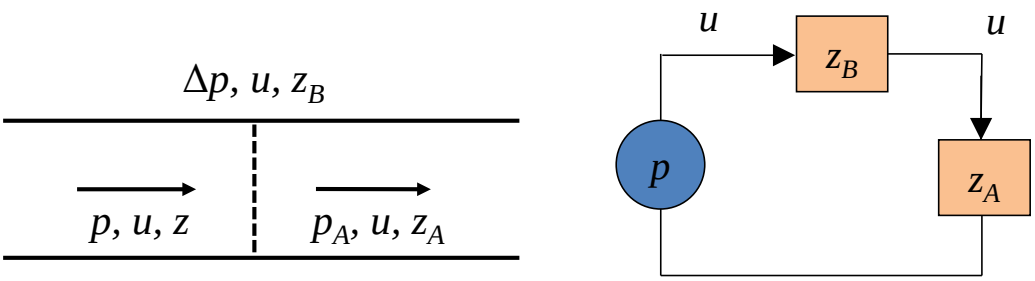

(a) (b)

Figure 2.3 A perforated plate (a) and its series impedance circuit analogy (b).

The following sections will review current measurement and modeling practice for two types of series impedances, namely source impedances and transfer impedances.

2.1.5 Measurement of acoustic impedance

Several measurement techniques involving a plane wave tube and microphones have been developed to determine the acoustic impedance. One method is the standing-wave-ratio (SWR) method where a traversing microphone is used to determine the location and magnitude of successive maxima and minima in a tube terminated by some unknown load impedance, as illustrated in Figure 2.4. The purpose of the measurement is to characterize the load impedance.

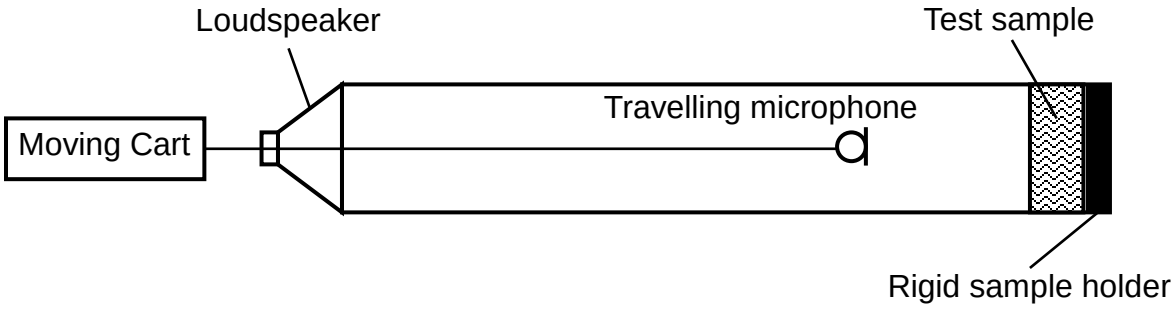

Figure 2.4 Setup for measuring reflection coefficient using SWR method.

As shown in Equation (2.1.17), the reflection coefficient is the ratio of the complex amplitude of the reflected wave ($\boldsymbol{B}$) to that of the incident wave ($\boldsymbol{A}$). It is not possible to measure $\boldsymbol{A}$ and $\boldsymbol{B}$ separately, but only sound pressure amplitude in the tube using one microphone. The maximum sound pressure amplitude ($\boldsymbol{A}+\boldsymbol{B}$) occurs at a pressure antinode, and the minimum sound pressure amplitude ($\boldsymbol{A}-\boldsymbol{B}$) occurs at a node (Kinsler, 1999). The ratio of the amplitude at an antinode to that of a node is the *standing wave ratio*

$$\mathrm{SWR} = \frac{\boldsymbol{A}+\boldsymbol{B}}{\boldsymbol{A}-\boldsymbol{B}} \tag{2.1.31}$$

The amplitude of reflection coefficient can be calculated from the standing wave ratio by

$$\boldsymbol{R} = \frac{\boldsymbol{B}}{\boldsymbol{A}} = \frac{\mathrm{SWR}+1}{\mathrm{SWR}-1} \tag{2.1.32}$$

The phase angle of reflection coefficient can be evaluated from the distance of the first node from the rigid end. Once the reflection coefficient is measured, the acoustic impedance can be deduced from Equation (2.1.18).

There are two standards that provide detailed derivations and guidelines for making the measurements: ASTM C384-03 and ISO10534-1:1996 (ASTM, 2003, ISO, 1996). The technique can be time consuming since the traversing mechanism is usually operated manually and discrete frequency excitation is used.

An alternative method is called the two-microphone random-excitation method (Seybert and Ross, 1977), or transfer function method (Chuang and Blaser, 1980). An acoustic driver with random noise signal is mounted at one end of an acoustic waveguide, and the test specimen or unknown duct system is mounted at the other. The microphones are located at the end of the waveguide opposite the source and are flush mounted to the waveguide, as shown in Figure 2.5.

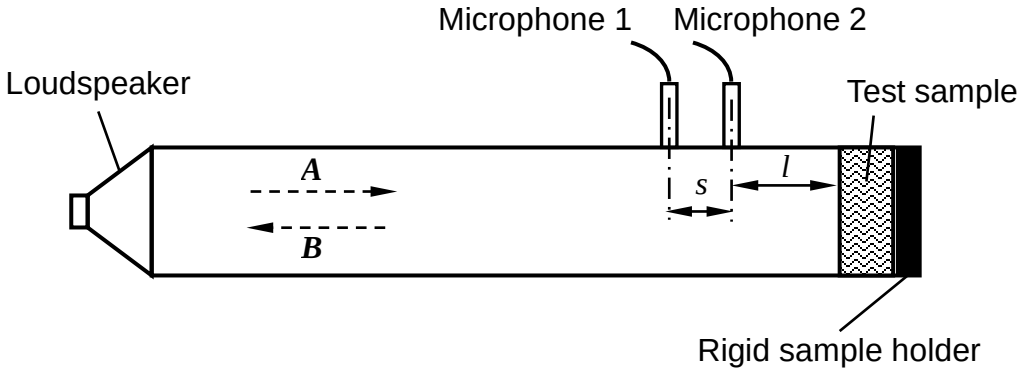

Figure 2.5 Setup for measuring reflection coefficient using two-microphone method.

Sound pressures at two positions ($\boldsymbol{p}_1$ and $\boldsymbol{p}_2$) can be written as the sums of incident waves and reflected waves using Equation (2.1.14). The complex transfer function H_{12} between $\boldsymbol{p}_1$ and $\boldsymbol{p}_2$ is the ratio of these two sums. The transfer function is calculated from the auto-spectrum and cross-spectrum measured using two microphones. The Reflection coefficient can be obtained from the measured transfer function H_{12} by

$$\boldsymbol{R} = \frac{H_{12} - e^{-jks}}{e^{jks} - H_{12}} e^{j2k(l+s)} \tag{2.1.33}$$

The use of random excitation permits the evaluation of properties at all frequencies from a single test. This is a considerable savings of time and labor as compared to the standard SWR method.

When using the two-microphone technique, the phase mismatch between microphones is unavoidable and can introduce considerable error into the impedance calculation. Both amplitude and phase mismatches need to be corrected. The mismatches can be calculated by measuring transfer functions successively with the channels interchanged.

The detailed guidelines can be found in both ASTM E1050-98 (ASTM, 1998) and ISO 10534-2:1998 (ISO, 1998). The measurement accuracy and uncertainty propagation of different error sources, i.e. bias error and random error, has been studied both theoretically and numerically (Boden and Abom, 1986, Abom and Boden, 1988, Seybert and Soenarko, 1981, Schultz, 2007).

2.1.6 Network representations of acoustic impedance

The practical advantage of using lumped acoustic impedances is that acoustic discontinuities can be represented as a black box in an acoustic network (Fahy, 2001, Morse and Ingard, 1987). The acoustic network representation of a duct system is made possible because of the existence of well-established analogies between electrical circuit and acoustical variables. In acoustic network theory, elements can be modeled as acoustic two-ports or one-ports. An example of acoustic network representation of a duct system is shown in Figure 2.6.

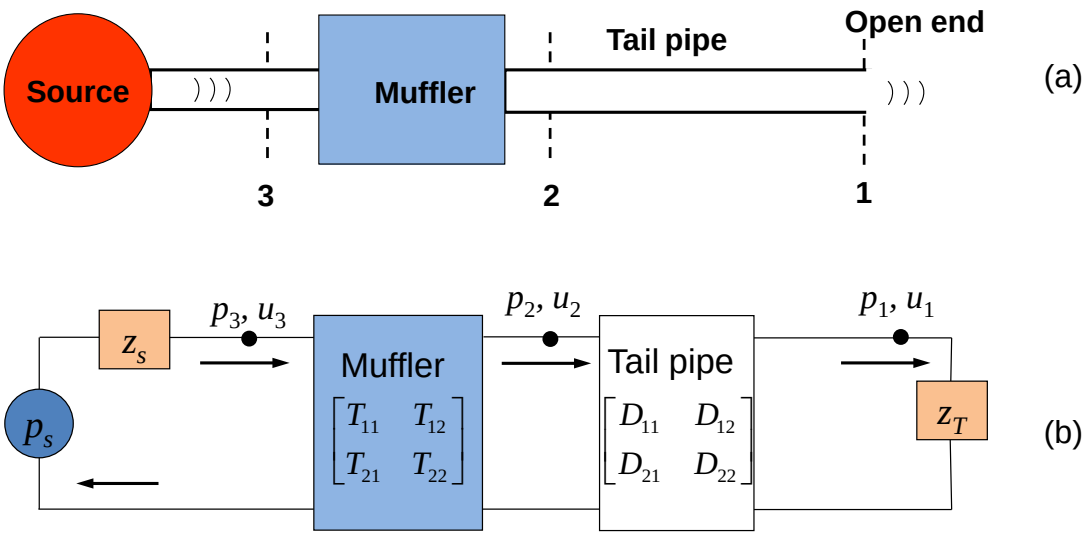

Figure 2.6 A duct system (a) and its acoustic network representation (b) (Munjal, 2006).

A two-port is a black box with one inlet and one outlet. Mufflers, perforated panels and resonators can all be modeled as a two-port (Glav and Abom, 1997). For two-port theory, there are two additional assumptions aside from the plane wave assumption. First, the acoustic field in a duct system is linear; second, the black boxes modeling the inlet and outlet must be passive (Boden and Glav, 2007). Acoustic two ports can be modeled using a transfer matrix or four-pole. The transfer matrix relates the pressure and particle velocity pair at the inlet to the outlet, as shown in Figure 2.7. T_{11}, T_{12}, T_{21} and T_{22} are four poles of the transfer matrix. For example, the transfer matrix of a straight duct with length L can be expressed as:

$$\begin{Bmatrix} p_1 \\ v_1 \end{Bmatrix} = \begin{bmatrix} \cos(kL) & j\rho_o c \sin(kL) \\ (j/\rho_o c)\sin(kL) & \cos(kL) \end{bmatrix} \begin{Bmatrix} p_2 \\ v_2 \end{Bmatrix} \tag{2.1.34}$$

where p_i's are sound pressures, and v_i's are particle velocities. The velocity is selected as a particle, volume, or mass velocity depending on preference and utility.

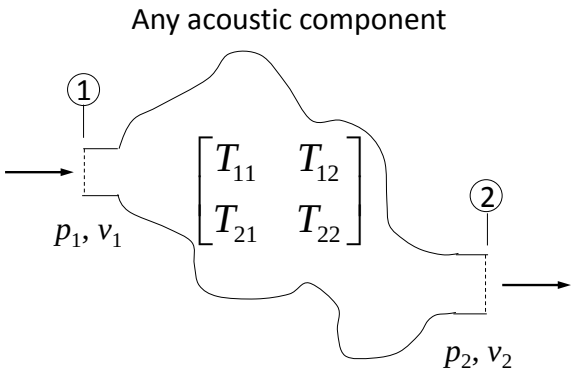

Figure 2.7 Transfer matrix relates pressures and velocities on both sides.

Alternatively, muffler components can be modeled using either a scattering or impedance matrix. A scattering matrix relates the incident and reflected complex wave amplitudes of the inlet to the outlet (Glav and Abom, 1997). An impedance matrix relates the sound pressure to the particle velocity at the inlet and outlet (Wu, 1998). These three models are interchangeable and can be chosen depending on the nature of the problem.

A one-port is an element used to represent an acoustic input or source and its impedance. This element can be used to model sources such as engines or fans that drive a system. In order to describe the one-port element, the impedance, instead of the transfer matrix, is usually used to relate pressure and velocity at the opening of the element. For example, an acoustic one-port can be described by:

$$p_l = p_s - u \cdot z_s \tag{2.1.35}$$

where p_s and z_s are source strength and source impedance, and p_l and u are the resulting acoustic pressure and particle velocity at the port.

If acoustic input p_s is set to zero, the element can also be used to model a duct termination. One-port model of a duct termination can be described as:

$$p_t = u \cdot z_t \tag{2.1.36}$$

where p_t and u are the acoustic pressure and particle velocity at the termination, and z_t is termination impedance.

One-port representations of a source and a termination can also be illustrated using electro-acoustic analogies, as shown in Figure 2.8 (a) and (b).

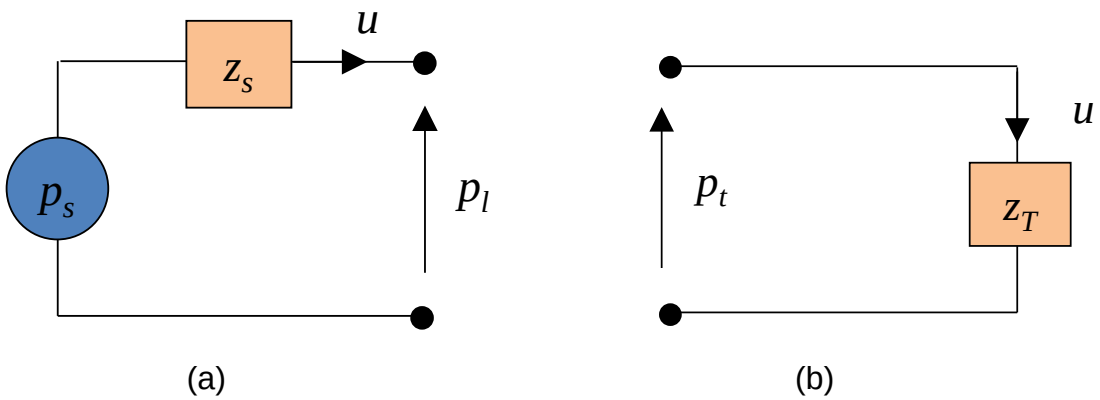

Figure 2.8 One port representations of a source (a) and a termination (b).

In the following sections, two types of series impedances, namely source impedance, and transfer impedance will be introduced. Their modeling and measurement techniques will be surveyed.

2.2 Source impedance

In order to thoroughly investigate the muffler system, HVAC duct, fluid machine or refrigerant line, it is necessary to characterize the acoustic sources (for example, engine, fan, or compressor) (Rammal and Abom, 2007, Boden, 2007, Knutsson 2007, Boden, 1995). These sources are commonly represented by a combination of source strength and source impedance, as illustrated by a source-duct system and its equivalent electro-acoustic 1-port analogy in Figure 2.9. In this figure, p_s and z_s are source strength and source impedance, and p_l and z_l are load pressure and load impedance. $x=0$ is the separation point between source and load. The load impedance represents the downstream duct system including attenuating elements and termination. Based on electro-acoustic analogy, the relationship between source and load can be described as:

$$\frac{p_s}{z_s + z_L} = \frac{p_L}{z_L}. \qquad (2.2.1)$$

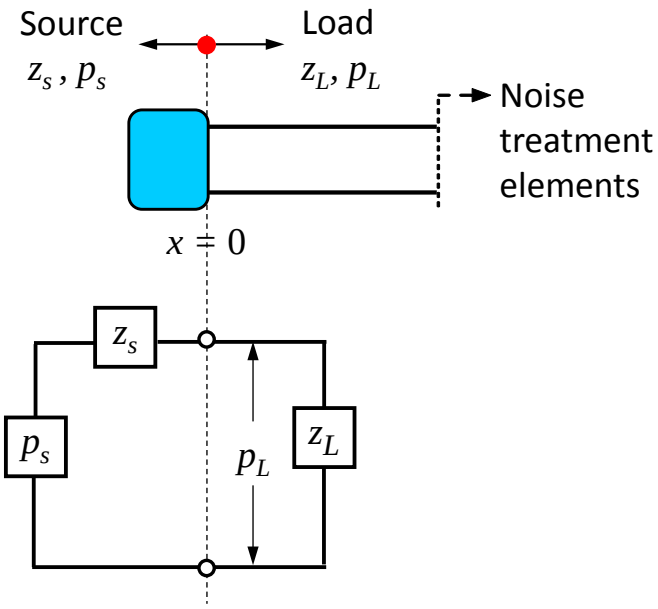

Figure 2.9 Source-duct system and its equivalent electro-acoustic analogy.

The acoustic descriptions of a duct system that requires the knowledge of source characteristics are insertion loss and radiated sound pressure levels (Prasad, 1983, Munjal and Sreenath 1970). Prior to 1975, researchers were aware of the importance of the source impedance, but they tried to model source impedance as a constant for simplicity instead of measuring it (Munjal and Sreenath 1970, Galaitsis and Bender 1975). Three values were commonly assumed: i) an infinite source impedance which assumes a velocity source, ii) the characteristic impedance which assumes a reflection-free source, or iii) zero impedance which assumes a pressure source. These simplifications are still used in the absence of information regarding the source (Herrin, 2006). Researchers have noted insertion loss variations of 10 to 40 dB at medium to high frequencies depending on the assumed source impedance (Munjal and Sreenath 1970, Galaitsis and Bender 1975).

The first reported source impedance measurement was performed by Galaitsis and Bender (1975). In their experiment, source impedance of a six-cylinder diesel engine was measured using the standing wave method. A discrete frequency excitation was used to drive an external source, and a traversing microphone was used to measure the standing wave ratio. It was

observed that the source impedance was irregular at low frequencies and should not be assumed constant. At high frequencies, the source impedance approached the constant characteristic impedance. Ross and Crocker (1983) used a similar technique to measure the source impedance of an eight cylinder engine. In order to eliminate differences between speed and load settings and longtime delay between tests, a random noise source was used to evaluate standing wave parameters. Their test results showed that measured engine internal source impedance appeared to fluctuate around the characteristic impedance, and the measured source impedance had a weak dependence on engine load but a strong dependence on engine speed.

Researchers quickly adopted the two-microphone random excitation method (Seybert and Ross, 1977), which had been developed to measure acoustic material properties, to measure source impedance (Prasad and Crocker, 1983). Instead of traversing a microphone at discrete frequencies, the two-microphone random excitation method allows all frequencies to be excited and measured simultaneously. Additionally, the microphone positions are fixed. However, the two-microphone method requires sufficient signal-to-noise to separate the white noise source signal from the broadband flow noise in the tube. The measured results by Prasad and Crocker (1983) were in opposition to those previously reported by Ross and Crocker (1983). Prasad and Crocker's results showed that variation in engine speed did not seem to have any significant effect on source impedance of an eight-cylinder internal combustion engine.

The measurement techniques mentioned above (Galaitsis and Bender 1975, Ross and Crocker, 1983) can be categorized as a direct method where a secondary source with a much greater amplitude is used to provide excitation to measure the source impedance. Therefore, the noise output from the engine can be neglected. The impedance of the primary source is measured by assuming that it is passive, i.e. a special type of absorbing material. The advantage of the direct method is its measurement accuracy and simplicity. The primary difficulty of the direct method is finding a secondary source that is powerful enough. This is especially difficult for the case of engine combustion. Additionally, the direct

method can only measure source impedance, and is not capable of measuring source strength. Despite these disadvantages, the direct method is still being applied to measure the source impedance of low energy sources due to its simplicity and accuracy (Rammal and Abom, 2007, Edge and Johston, 1990).

Alternative methods that do not require a secondary source and can measure both source strength and source impedance have also been developed. These attractive methods are categorized as indirect methods. Using indirect methods, the source strength and impedance are determined by varying the acoustic load. This can be accomplished by changing the termination or varying the duct length as illustrated in Figure 2.10. For straight ducts, the load impedance can be determined theoretically. However, it is preferred to measure each load experimentally, especially when mufflers or absorptive terminations are used for loads.

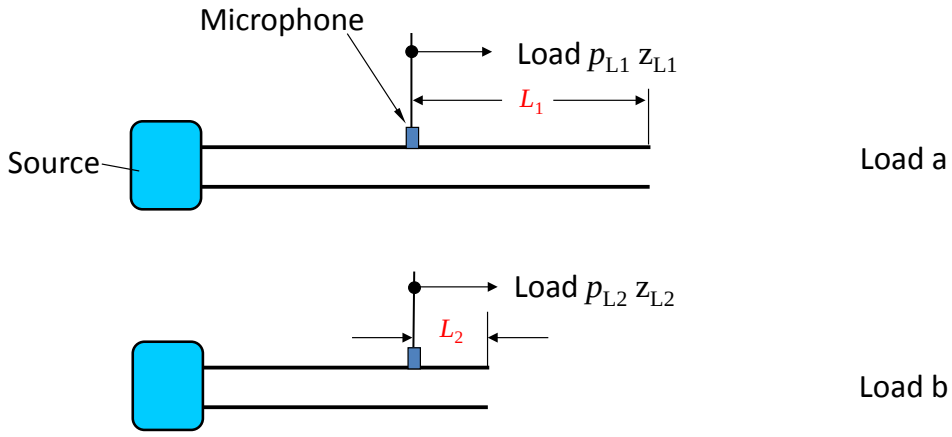

Figure 2.10 Two-load Method for indirect source characteristics measurement.

Since there are two unknowns, two loads are sufficient. This has been called the two-load method (Kathuriya and Munjal, 1979, Boden, 1988, Egolf and Leonard, 1977). Source impedance and source strength are calculated from the measured load pressures and impedances using

$$z_s = \frac{z_{L_1} z_{L_2} (p_{L_1} - p_{L_2})}{z_{L_1} p_{L_2} - z_{L_2} p_{L_1}} \tag{2.2.2}$$

And

$$p_s = \frac{p_{L_1} p_{L_2} (z_{L_1} - z_{L_2})}{z_{L_1} p_{L_2} - z_{L_2} p_{L_1}} \tag{2.2.3}$$

Each of the variables in Eqation (2.2.3) is complex. Accordingly, the phase information measured using each acoustic load must be preserved. Therefore, as Boden stated (Boden, 1995), “a reference signal unaffected by acoustic load variations and related to the sound generating mechanism of the source is needed.” Typical reference signals have included accelerometers placed on the running engine or input voltages. (Tao, 2007).

Alternatively, least squares methods can be used to take advantage of measuring additional loads. Based on Equation 2.2.1, an overdetermined problem can be formed which calculates source impedance and source strength with less sensitivity to the loads (Boden, 1988, 1991, 1992). Nevertheless, care should be taken to insure that the loads are as different as possible to avoid linear dependency. For instance, the combination of an anechoic termination and open-ended tube is preferred to a combination of two open-ended tubes of similar length (Boden, 1988, Liu, 2009).

It is not always practical to have a suitable reference signal. For example, the signal from an accelerometer placed on the engine body can correlate the harmonic components in the engine exhaust noise spectrum but not the broadband components caused by gas flow turbulence. In many situations, microphones cannot be placed inside the duct due to the temperature and flow. It is then desirable to measure outside of the duct.

Alternative methods like the three-load (Alves, 1986, 1987) and the four-load (Prasad, 1987) methods were developed for this very reason. By taking the square magnitude of Equation 2.2.1, four unknowns, the real and imaginary parts of p_s and z_s respectively, are reduced to three; magnitude of p_s and real and imaginary parts of z_s. Meanwhile, the phase information for the load pressure is eliminated from the equation. Therefore, three sound pressure levels measured outside of the duct for three known load impedances are sufficient to determine the source strength and impedance. However, two second-order nonlinear

equations need to be solved in order to obtain the real and imaginary parts of the source impedance. This could lead to more than one real-valued solution. Large measurement error has also been reported for the three-load method.

In order to solve the nonlinear problem, Prasad (1987) proposed a four-load method that reduced three nonlinear equations to two linear equations using a fourth measurement. Several approaches have been developed to improve the three-load and four-load methods (Jang and Ih, 2002, Boden, 1991, Coulon, 1993, Desmons, 1994). Most of the improvement techniques mentioned above involve a least square or optimization algorithm (Desmons, 1994, Jang and Ih, 2000). Regardless of the approach, researchers have concluded that accurate measurement of source strength and impedance is contingent on selecting appropriate load combinations. These studies suggest a few guidelines for selecting appropriate load combinations in order to minimize the measurement error (Jang and Ih, 2002, Desmons, 1995).

All the measurement methods mentioned above are based on the assumption that the source is time-invariant and linear. However, this is not always the case. For example, engine speed and combustion processes may vary over time. In addition, changing the acoustic load will change the pressure drop. This will in turn impact the combustion process. The time variance of the source may lead to large measurement error and negative source resistance which is physically implausible (Lavrentjev, 1992, Peat and Ih, 2001, Ih and Peat, 2002). Time-variant and nonlinear models that include these effects and a time-domain representation of the source were developed to improve the multi-load approaches assuming sufficient data is available. (Rammal and Abom, 2007, Boden, 1995, Peat and Ih, 2001).

Instead of measurement, it is also possible to extract source data from simulation. Hota and Munjal (2008, 2009, 2010), Knutsson and Boden (2007), and Boden (2007) have successfully used numerical multi-load methods to obtain the source impedance and source strength with some accuracy based on the CFD simulations. The pressure time history of the source, usually an engine intake or exhaust, is computed by means of time-domain finite-volume numerical

simulation. From this pressure time history, the source impedance and source strength can be virtually measured using a combination of models (linear or nonlinear, time-invariant or time-variant) and measurement techniques (two-load or multi-load methods). Hota and Munjal (2008, 2009, 2010) performed parametric studies of the engine source as a function of the air fuel ration, engine speed, engine capacity and the number of cylinders, and developed empirical equations for the source characteristics of typical engines which can be immediately applied to muffler performance simulation. This idea could be used to characterize other sources (i.e. fluid machines and HVAC equipment) and develop a database of different sources.

The source impedance and source strength measurement techniques are summarized in Table 2.1.

Table 2.1 Summary of source characteristics measurement techniques.

<table>
<tr><td rowspan="6">Source characterization methods</td><td rowspan="5">Time-invariant and linear model</td><td rowspan="2">With external source, i.e. Direct Measurement</td><td colspan="2">Standing-Wave-Ratio (SWR) method</td></tr>
<tr><td colspan="2">Two Microphone random excitation method</td></tr>
<tr><td rowspan="4">Without external source, i.e. Indirect measurement</td><td colspan="2">With reference signal , i.e. Two-load method</td></tr>
<tr><td rowspan="3">Without reference signal</td><td>Three-load method</td></tr>
<tr><td>Four-load method</td></tr>
<tr><td>Modified Multi-load methods with least square or optimization approaches.</td></tr>
<tr><td colspan="3">Time-variant and nonlinear models</td></tr>
</table>

2.3 Transfer impedance

Transfer impedance, also known as separation impedance (Morfey, 2000) or acoustic flow resistance (Ingard, 1985), is used to acoustically characterize thin permeable materials. This includes protective cloths of muffler linings (Wu, 2003), permeable ceramic walls in Diesel Particulate Filter (DPF) (Allam and Abom, 2005), and perforated plates in HVAC ducts (Wu, 1997). Since the material is thin and permeable, the velocities in front and back of the material can

be assumed to be the same. The two-port representation of a transfer impedance is shown in Figure 2.11 where p_1 and p_2 are the respective sound pressures anterior and posterior to the material and u_1 and u_2 are the respective particle velocities. z_{tr} is the transfer impedance.

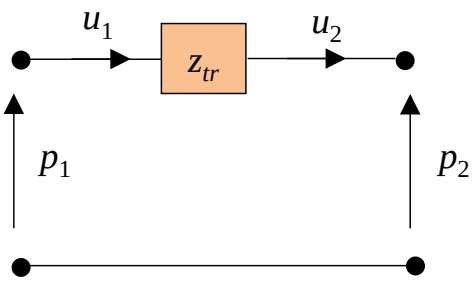

Figure 2.11 Two-port representation of transfer impedance.

By assuming a single particle velocity across the material thickness, i.e. $u = u_1 = u_2$, transfer impedance is defined as the ratio between acoustic pressure drop through the material and the normal particle velocity, and can be written as

$$z_{tr} = \frac{\Delta p}{u} = \frac{p_1 - p_2}{u} \tag{2.3.1}$$

where Δp is the pressure difference in front and back of the material.

The transfer matrix representation of Equation (2.3.1) can be written as: (Wu, 2003, Lee and Kwon, 2004, Tao, 2005)

$$\begin{Bmatrix} p_1 \\ u_1 \end{Bmatrix} = \begin{bmatrix} 1 & z_{tr} \\ 0 & 1 \end{bmatrix} \begin{Bmatrix} p_2 \\ u_2 \end{Bmatrix} \tag{2.3.2}$$

Once transfer impedance is obtained, it can be used to evaluate the acoustic performance of the thin materials and perforates in built-up systems. The representation in Equation 2.3.2 is especially convenient for modeling waveguides. Wu et.al (2003) used the measured transfer impedance of a protective cloth in a direct-mixed body BEM analysis of a packed silencer. Good agreement was obtained with measurement. Lee and Kwon (2004) evaluated the absorption coefficient of multi-layer perforated plates by multiplying transfer matrices of perforated plates and adjoining airspace. Tao et.al (2005) used an identical approach to calculate the absorption coefficient of multi-layer

microperforated panels with good agreement with measured results, and Allam and Abom (2005) used transfer impedance to model the permeable walls of a diesel particulate filter.

The transfer impedance can be obtained by theoretical modeling if the geometry and material properties of the material are known. For example, several models for perforated plates have been developed (Atalla and Sgard, 2007, Melling, 1973, Maa, 1983, Allam et.al, 2009). However, for most materials, exact geometry and material properties are difficult to obtain. Hence, the transfer impedance is best measured in most cases.

Melling (1973) proposed a two-microphone method to measure the transfer impedance of perforates. The first microphone is placed in front of the perforate, and the second microphone is mounted in the back wall of the back cavity posterior to the sample as shown in Figure 2.12.

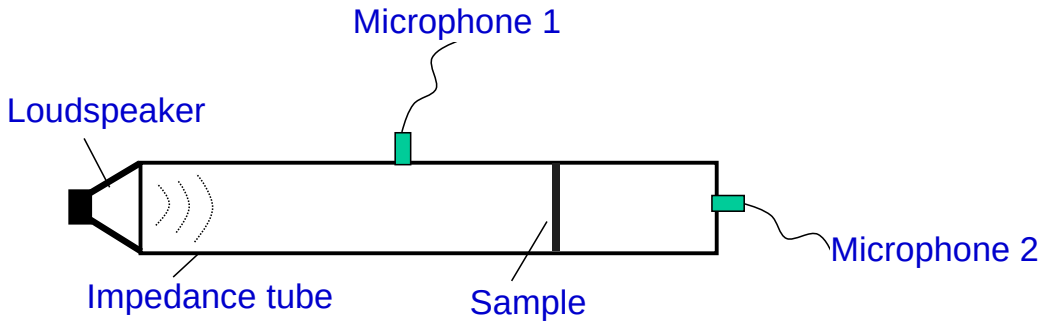

Figure 2.12 Experimental setup for direct measurement of transfer impedance.

Both the particle velocity and the sound pressure directly behind the perforate can be derived the sound pressure measured by the second microphone. The sound pressure anterior to the sample is measured directly using the first microphone. Ingard and Dear (1985) used a similar impedance tube and microphone arrangement to measure the transfer impedance, named acoustic flow resistance in the paper, of a thin piece of porous material. In order to calculate transfer impedance directly from measured sound pressures, the distance between sample and rigid termination was chosen to be an odd number of quarter wavelengths. The major drawback of this approach is that the transfer impedance is only obtained at discrete frequencies. However, Ren and Jacobsen

(1993) further developed this method to measure the dynamic flow impedance as a continuous function of the frequency.

As suggested by Ingard (1985), for a thin layer of material at sufficiently low frequencies, the steady-state flow resistance is expected to be applicable to the fluctuating acoustic field. This approximation provided a different means for characterizing transfer impedance. Mechel et.al (1965), earlier than Ingard, had measured both flow resistance and acoustic flow resistance, i.e. real part of transfer impedance, of a 1 mm thick porous foil. A blower sucked the air through the absorptive wedge at the end of the impedance tube. A loudspeaker was installed at the other end of the tube, and a hot-wire anemometer was placed in front of the sample to measure flow velocity. The difference between the static pressures at front and rear were measured with a pressure gauge. The measurement setup is shown in Figure 2.13.

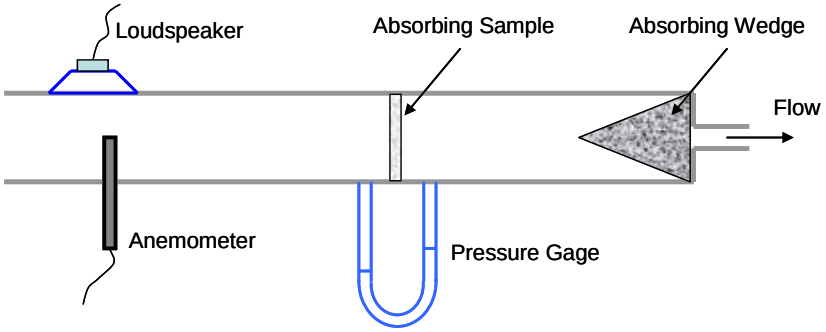

Figure 2.13 Experimental setup for impedance and flow resistance measurement (Mechel, 1965).

Acoustic flow resistance was calculated at a single frequency, i.e. 1000 Hz, using SWR method. Flow resistance is calculated based on static pressure drop and flow velocity. The measurement results comparison shows that error between acoustic flow resistance and flow resistance is about 20 percent. Mechel's research demonstrated that it is possible to use "DC" flow resistance to represent transfer impedance of a thin layer of material at low frequencies. This approach was used by Allam and Abom (2005) to measure real part of transfer impedance, i.e. wall resistance, of DPF. Wall resistance from one channel to another was calculated based on pressure drop through the whole unit, the flow velocity in the transmission line, and number and size of channels. Researchers

at University of Kentucky measured flow resistances of micro-perforated panels using simple weighted-piston device developed by Ingard (2010). The flow resistances were then compared to acoustically measured transfer impedances. It was noticed that the real part of transfer impedance was roughly constant below 2000 Hz, and was correlated but not equal to the measured flow resistance. However, there has not been an empirical equation developed to relate measured flow resistance to transfer impedance for micro-perforated panels.

Since thin permeable materials can also be represented as transfer matrices, as shown in Equation 2.3.2, the transfer impedance can be calculated from the measured transfer matrix. Transfer matrix measurements usually involve two basic measurements with either two different terminations, i.e. Two-load method (Song and Bolton, 2000), or two different sources, i.e. Two-source method (Munjal and Doige, 1990). For each configuration, four sound pressures or three transfer functions are measured and used to calculate four poles. A typical Two-source measurement setup is shown in Figure 2.14. Lee et.al (2004), Tao et.al (2005) and Yoo (2008) measured transfer matrix of perforated plates or micro-perforated panels using Two-load or Two-source method. Once transfer matrix is measured, transfer impedance can be calculated from four poles(Yoo, 2008). For example, if T_{11}, T_{12}, T_{21} and T_{22} are four poles of the transfer matrix, then reflection coefficient of material plus anechoic termination can be expressed as

$$R = \frac{T_{11} + (T_{12}/\rho_0 c) - \rho_0 c T_{21} - T_{22}}{T_{11} + (T_{12}/\rho_0 c) + \rho_0 c T_{21} + T_{22}} \tag{2.3.3}$$

Transfer impedance can be calculated from reflection coefficient using Equation 2.3.4.

$$z_{tr} = \rho_0 c \left(\frac{1+R}{1-R} - 1 \right) \tag{2.3.4}$$

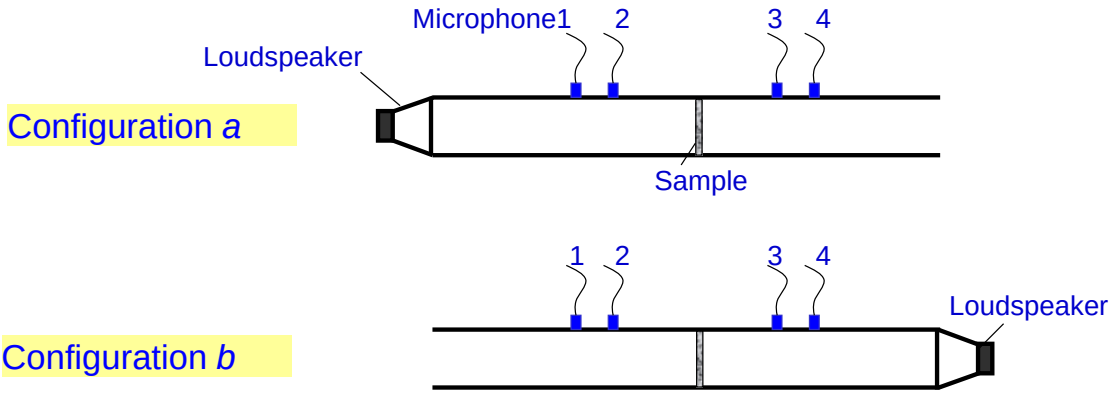

Figure 2.14 Two-source method set up for measuring transfer matrix.

An alternative method to measure the transfer impedance was developed by Wu et.al (2003). The measurement setup is very similar to the two-cavity method (Utsono, 1989) except that the cavity length does not need to be changed. Equation 2.3.1 suggests that transfer impedance is essentially the difference between the impedances in front and back of the panel. Impedance in front of the panel is the impedance combining panel and back cavity, which can be measured using the two-microphone method (Seybert and Ross, 1977). The impedance behind the panel is the impedance of the back cavity which can be calculated theoretically. This method was used to measured transfer impedance of protective cloth and micro-perforated panels with good agreement with theoretical results.

CHAPTER 3
MODELING AND MEASUREMENT OF PERFORATED PANELS

Perforated plates and screens have been used very effectively as tube in mufflers (Allam et al., 2009, Elnady, 2003), insert layers in composite absorptive materials, and as stand-alone absorptive panels (Wu, 1997). If the porosity is high, perforated panels can be used as protective layers with minimal acoustic effect. As has been discussed in the previous chapter, a perforated panel can be modeled as a transfer impedance, which will depend on the porosity, perforation size and panel thickness.

Depending on the perforation size, perforated panels can be divided into two categories. The term *macro-perforated* is adopted to describe panels with diameter of perforations ranging from 1 mm to 1 cm. Panels with sub-millimeter diameter are called *micro-perforated* panels; a term adopted by most researchers in the area (Maa, 1975, Atalla, 2007).

In this chapter, classical models for macro-perforated and micro-perforated panels will be reviewed. This will be followed by a survey of different measurement techniques.

3.1 Modeling and measurement of macro-perforated panels

This section will review the prior research aimed at characterizing the transfer impedance of macro-perforated panels. A typical configuration consists of a flat rigid panel with periodically arranged circular holes. Figure 3.1 shows a stand-alone macro-perforated panel in a plane wave field. Assuming negligible interaction effect between perforations, a macro-perforated panel can be considered as a lattice of short narrow tubes. The classical approaches determine the global properties of the macro-perforated panel by considering the acoustic impedance of a single perforation, and then then using the porosity to determine the impedance for a panel. (Zwikker and Kosten, 1949).

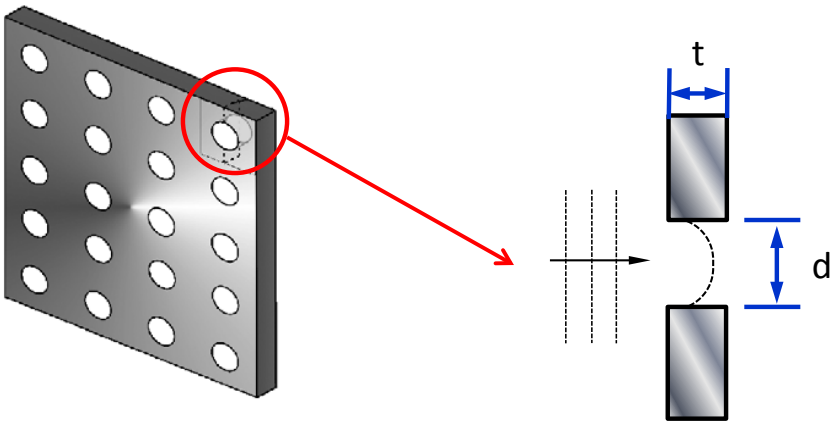

Figure 3.1 Perforated plate in plane wave field (Atalla, 2007).

Crandall (1927) first assumed the perforated hole to be an infinite length tube. He simplified works by Lord Rayleigh (1877) on propagation of sound in a narrow tube, and then added an end correction term to the impedance to account for the finite length of the perforated holes. Depending on the hole size and frequency range, Crandall's simplification yields two types of energy loss mechanisms: Poiseuille and Helmholtz type respectively. For small holes or low frequencies, the loss mechanism is described by Poiseuille's law of resistance for laminar flow of viscous fluids in narrow tubes. These losses are frequency independent.. For large holes or higher frequencies, the energy dissipated is due to the friction between the tube wall and the air moving in the tube. This type of loss is called Helmholtz-type and is frequency dependent (Ingard, 1953).

For perforated panel with small holes, the panel thickness and the hole diameter are small compared to an acoustic wavelength. The air in the hole moves as a rigid piston. The effective mass of this piston will be equivalent to a cylinder of air whose length is slightly longer than the thickness of the panel. This is called the end correction (Elnady, 2003). Sivian (1935) and Ingard (1953) examined this piston effect theoretically and experimentally. The end correction for the resistance term accounts for viscous effects at both sides of the orifice. The end correction for the reactance term accounts for the oscillation of the additional mass.

The previously described physical phenomena in a single hole of a perforated plate are illustrated in Figure 3.2. The left schematic figure shows that

the resistive part of the impedance of the hole is induced by: i) viscous boundary layers inside the hole, ii) viscous boundary layers at the panel surface, and iii) distorted flow at the edge of the hole. The right schematic figure shows that the reactance is induced by: i) motion of the air cylinder in the hole, ii) inertia effects, and iii) viscous effects.

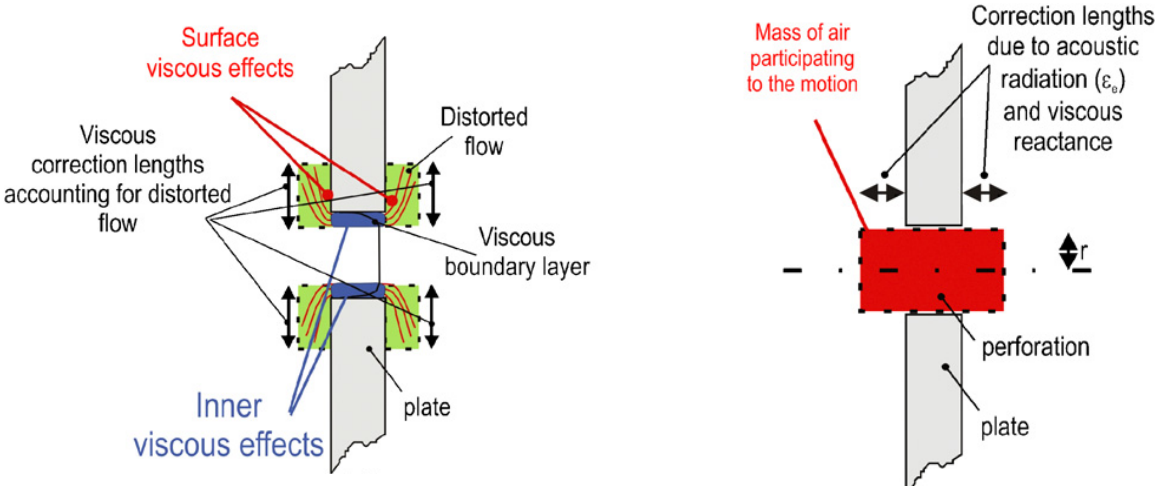

Figure 3.2 Illustration of physical phenomena involved in resistive (left) and reactive (right) parts of impedance in a single hole (Atalla, 2007).

The classical approaches determine the global properties of a perforated panel by generalizing the acoustic impedance of a single hole to the whole panel. It is based on the assumption that the holes are far apart; therefore no interaction exists between adjacent holes. However, for panels with high porosity, the assumption may not be valid. The interaction between adjacent holes was studied by Ingard (1953) and Melling (1973). They found that the interaction reduced the shear region between two interacting holes and resulted in a modification factor for the end correction. For example, the reactive end correction is larger, by a factor of $\sqrt{2}$, for two separate holes than for one hole with area equal to the sum of the two separate holes (Melling, 1973).

In applications such as HVAC ducts and mufflers, perforated panels are usually exposed to the mean gas flow. It is known that flow has an effect on the acoustic performance of the perforated panels (Cummings, 1986). Penetrating flow increases acoustic resistance because more energy is dissipated due to higher particle velocity in perforations (Dean, 1976).

Perforated panels are commonly used in high sound pressure level environments. Once the sound pressure level exceeds 120~130 dB (Ingard, 1953), the acoustic performance is no longer independent of sound pressure. This nonlinear effect becomes significant for particle velocities around 5 m/s. Meling (1973) included nonlinear effects and also showed results.

In the following sections, a detailed description of macro-perforated panel modeling is presented.

3.1.1 Crandall's theory of acoustic propagation in a single tube

Crandall (1927) considered a single hole in a perforated panel as an infinite tube. The fluid can be modeled as a collection of shear layers that result from the viscous retardation near the wall. An exaggerated illustration of these annular rings of fluid at radius r is shown in Figure 3.3.

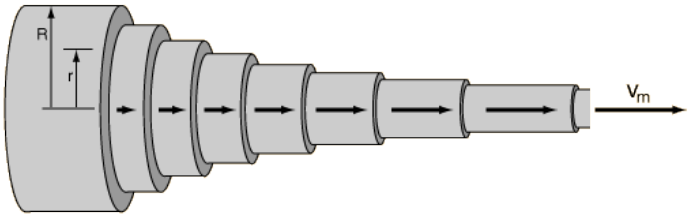

Figure 3.3 Illustration of annular rings of fluid caused by viscous resistive forces near the wall (Kundu, 2004).

Layers move at different velocities and the fluid's viscosity arises from the shear stress between the layers that oppose resistive force. For a plane wave traveling in the x-direction in a tube having radius (R), the viscous resistive force is proportional to the gradient of particle velocity and the contact area between layers. Figure 3.4 illustrates particle velocity and viscous force distribution on a cross section of a tube.

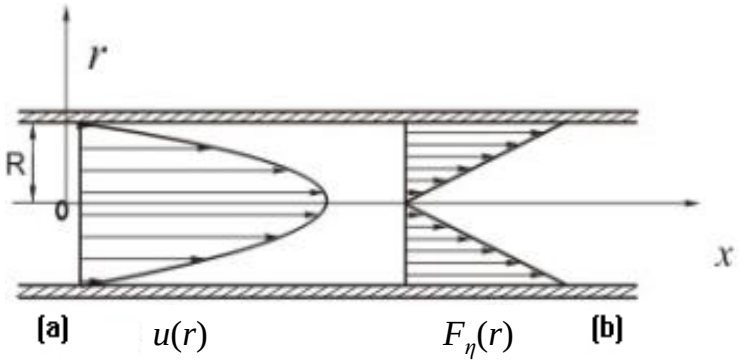

Figure 3.4 particle velocity distribution (a) and viscous force distribution (b) (Kundu, 2004).

The fluid in the tube is assumed to be air, which has a dynamic viscosity coefficient η. The net viscous force dF_η imposed on the fluid can be expressed as:

$$dF_\eta = \eta \frac{\partial}{\partial r}\left(\frac{\partial u}{\partial r} r\right) 2\pi dr dx \tag{3.1.1}$$

where x is the longitudinal axis and r is the radial axis. The driving force produced by pressure difference is

$$dp = -\frac{\partial P}{\partial x} 2\pi r dr dx \tag{3.1.2}$$

and the inertial force of the thin layer of air is:

$$\rho_o dV \frac{\partial u}{\partial t} = \rho_o 2\pi r dr dx \cdot (j\omega u) \tag{3.1.3}$$

where ω is angular frequency and j is the imaginary unit. The combined driving force caused by pressure difference and viscosity is balanced by the inertial force of air:

$$j\omega\rho_o u = \eta \frac{\partial}{\partial r}\left(\frac{\partial u}{\partial r} r\right) - \frac{\partial p}{\partial x} \tag{3.1.4}$$

Equation 3.1.4 above can be rewritten in a form with left side similar to the Bessel's equation of order zero:

$$\left(\frac{\partial^2}{\partial r^2} + \frac{1}{r}\frac{\partial}{\partial r} + k^2\right) u = -\frac{1}{\eta}\frac{\partial p}{\partial x} \tag{3.1.5}$$

where $k^2 = -j\omega\rho_0/\eta$ is the wave number of the viscous Stokes wave (Melling, 1973).

When the length of the tube (thickness of the panel) is much smaller than a wavelength, the pressure difference term $\partial p/\partial x$ can be approximated using the ratio between the pressure drop through the thin plate and the plate thickness $\Delta p/t$. Mean particle velocity across the tube cross-section can be obtained by averaging the velocity solved from Equation 3.1.5. Mean velocity is expressed as

$$\bar{u} = \frac{2}{R^2}\int_0^R urdr = -\frac{\Delta p}{\eta k^2 t}\left(1 - \frac{2}{kR}\frac{J_1(kR)}{J_0(kR)}\right) \tag{3.1.6}$$

where $J_0(x)$ and $J_1(x)$ are Bessel functions of the first kind of order's zero and one, respectively.

Then the specific acoustic impedance of a circular tube can be approximated by (Maa, 1983, Allard, 1993):

$$z = \frac{\Delta p}{\bar{u}} = j\omega\rho_0 t\left[1 - \frac{2}{\sqrt{-j}\beta}\frac{J_1(\sqrt{-j}\beta)}{J_0(\sqrt{-j}\beta)}\right]^{-1} \tag{3.1.7}$$

where $\beta = \sqrt{\frac{\rho_0\omega}{\eta}}R$ is called the shear wave number (Zwikker and Kosten, 1949), the Stokes number (Melling, 1973) or the perforate constant (Maa, 1997). β is proportional to the ratio of the tube radius and viscous boundary layer thickness. The perforate constant β compares the importance of inertial to viscous forces.

Historically, Equation 3.1.7 has not been used to calculate the impedance of a perforate, due to the difficulty in calculating the Bessel function with a complex valued argument, and in separating the real and imaginary components of the impedance function (Elnady, 2003). Simplified equations to approximate the Bessel functions were developed based on ranges for the perforate constant. For small perforate constants ($\beta<1$), i.e. low frequency and small hole size, a series expansion for the Bessel functions can be used, and the first two terms considered. For large perforate constants ($\beta>10$), an approximation to the Bessel function ratio $J_1(\sqrt{-j}\beta)/J_0(\sqrt{-j}\beta) = -j$ is used (Melling, 1973). This results in:

$$z \begin{cases} = \dfrac{8\eta t}{R^2} + \dfrac{4}{3} j\omega\rho_0 t & \beta < 1 \quad (3.1.8) \\ = j\omega\rho_0 t + \dfrac{2\rho_0\eta t}{R}\sqrt{\dfrac{\omega}{2\eta}}(1+j) & \beta > 10 \quad (3.1.9) \end{cases}$$

The real part of Equation 3.1.8 is Poiseuille's law of resistance for laminar flow of viscous fluid in narrow tubes. The real part of Equation 3.1.9 is frequency dependent and named Helmholtz-type resistance. Figure 3.5 compares the resistive impedance calculated using the three different equations. The dashed lines mark the perforate constant values of 1 and 10..

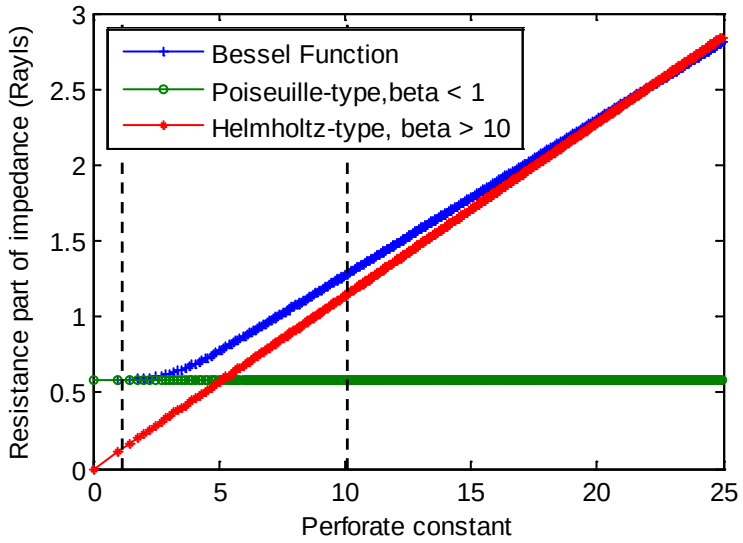

Figure 3.5 Resistances of a single hole calculated using three different equations.

For most of the macro-perforated panels, the condition $\beta>10$ can be satisfied at mid to low frequencies. For example, the perforate constant for a hole of 1 mm radius is geater than 10 above240 Hz.

In recent years, commercial codes such as Matlab can calculate Bessel functions with complex arguments easily using compiled commands (for example, BESSELJ in MATLAB (2009)). Therefore, it is more accurate to use Equation 3.1.7 other than its approximate forms.

For a slit-shaped perforation with length of $2l$ and width of $d = 2a$ as shown in Figure 3.6, Allard (1993) rewote Newton's Second Law as:

$$j\omega\rho_o u = \eta\frac{\partial^2 u}{\partial y^2} - \frac{\partial p}{\partial x} \tag{3.1.10}$$

where y is the slit width direction. This equation is the equivalent of Equation 3.1.4. Following the procedure identical to that for a circular tube, the transfer impedance of a single slit can be obtained as:

$$z = \frac{\Delta p}{\bar{u}} = j\omega\rho_0 t\left[1 - \frac{1}{\sqrt{j}\beta}\tanh(\sqrt{j}\beta)\right]^{-1} \tag{3.1.11}$$

where $\beta = a\sqrt{\frac{\rho_0\omega}{\eta}}$ is the slit perforate constant. Note that this equation is for a single rectangular slit only.

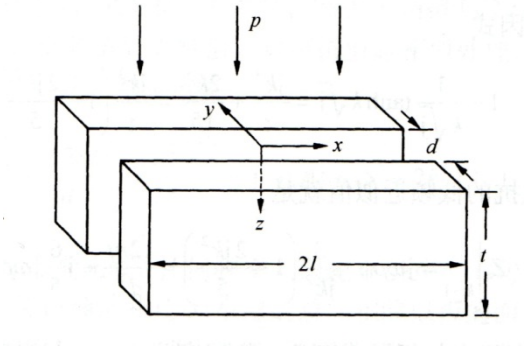

Figure 3.6 A single slit in plane wave field (Maa, 2000).

3.1.2 End corrections

For the case of short tubes, like perforations in plates, the end correction is necessary for both real and imaginary parts of transfer impedance. The resistive end correction accounts for the frictional losses on the surface of the plate, as the airflow is squeezed into the small area of the inlet end of the hole. The reactive end correction is due to the imaginary part of the radiation impedance at the tube's ends, which can be approximated by a circular piston of diameter d mounted in an infinite baffle. This effect can be represented by an effective additional tube length (Maa, 1975, Fenech, 2004). Figure 3.2 illustrates the physical phenomenon of the viscous effect on the plate and motion of additional mass, which result in end corrections for resistance and reactance respectively.

Ingard (1953) calculated the energy dissipation resulting from viscous friction over the parallel plate surfaces on both sides of the hole as:

$$W_v = \frac{1}{2}\int_s R_s |u_r|^2 ds \tag{3.1.12}$$

where s is the plate surface area surrounding the hole, $R_s = \frac{1}{2}(2\omega\eta\rho_0)^{1/2}$ is the surface resistance, and u_r is the tangential velocity over the plate surface. This led to a total end correction length of R.

The reactance of a hole results from the viscous and mass inertia effects in the hole. Ingard (1953) adopted Rayleigh's derivation of vibrating piston for the inertia effect. Rayleigh (1878) derived that a vibrating piston in an infinite baffle is equivalent to an attached mass of $(8R/3\pi)s$ at each end.

Several models for end correction due to resistance and reactance are summarized in Table 3.1 (Elnady, 2003, Thurston, 1952, Stinson, 1985, Bauer, 1977). Figure 3.7 shows comparison of end corrections calculated using different models.

Table 3.1 Summary of different end correction models

End correction models	Resistance	Reactance
Sivian, 1935	$8d/3\pi$	$8d/3\pi$
Ingard, 1953	$0.5d$	$8d/3\pi$
Bauer, 1977	$8d/3\pi$	$0.25d$
Elnady, 2003	$0.2d + 200d^2 + 16000d^3$	$0.5d$

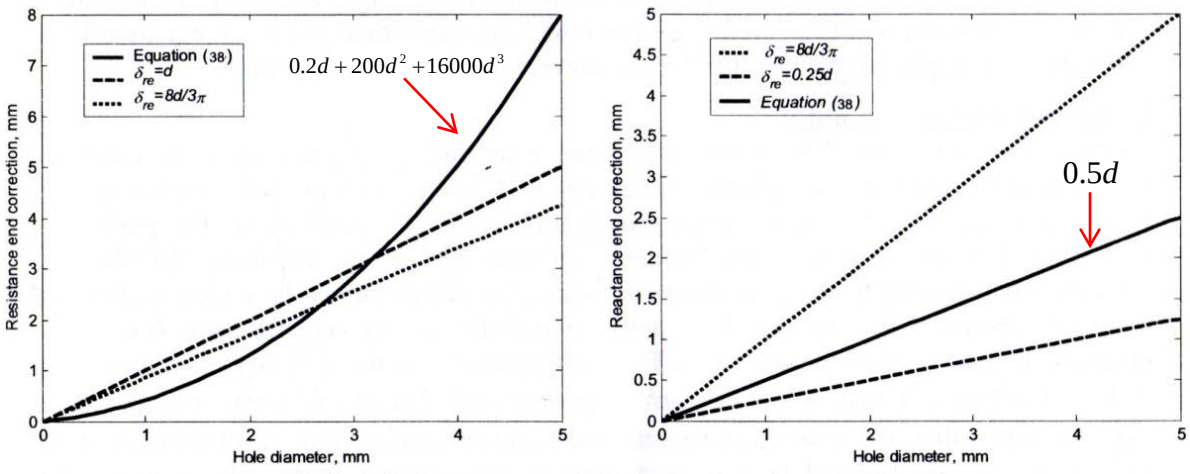

Figure 3.7 Comparison of end corrections obtained from different models (Elnady, 2003).

3.1.3 Interaction between two holes

In prior research efforts, it has been assumed that the behavior of a panel with an array of holes can be determined by the transfer impedance of a single hole and the porosity. The underlying assumption is that there is no interaction between two adjacent holes. This assumption should be appropriate if the two holes are widely separated. However, the interaction cannot be neglected if they are fairly close, which is the case for high porosity. Ingard (1953) considered the case of two adjacent circular apertures interacting and found that the effect of interaction mainly reduces end correction. For resistance, the end correction is reduced by a factor to account of the interaction between adjacent apertures. This affects the shear layer surrounding the apertures. The end correction for the reactive part is reduced by a factor of $\sqrt{2}$. Ingard suggested that the end correction should be multiplied by the factor

$$f_{\text{int}} = 1 - \sqrt{\sigma / 2} \tag{3.1.13}$$

where σ is porosity of perforated panel.

Melling (1973) considered an infinitely thin plate and deduced the Fok function which is function of the porosity and can be expressed as

$$f_{\text{int}} = 1 + a_1\sqrt{\sigma} + a_2\sigma + a_3\sqrt{\sigma^3} + \cdots \tag{3.1.14}$$

where $a_1 = -1.4092, a_2 = 0, a_3 = 0.33818, a_4 = 0, \cdots$

Elnady (2003) referred to Muller who introduced another form of the interaction factor

$$f_{\text{int}} = 1 - 1.47\sqrt{\sigma} + 0.47\sqrt{\sigma^3} \tag{3.1.15}$$

A plot in Elnady's paper compares different interaction factors, and the factors suggested by Melling and Muller produce similar results (Elnady, 2003).

3.1.4 Perforated panel with penetrating or grazing flow

In the present research, flow is neither measured nor considered. Nevertheless, it will be of interest to review the literature on the effect of flow because flow substantially impacts the absorptive properties. Figure 3.8 compares grazing and penetrating flow for mufflers and penetrating tubes.

The existence of penetrating flow (also called through flow or bias flow) will increase resistance while decreasing the reactance. The resistance becomes less dependent on frequency and sound pressure level as the penetrating flow increases.

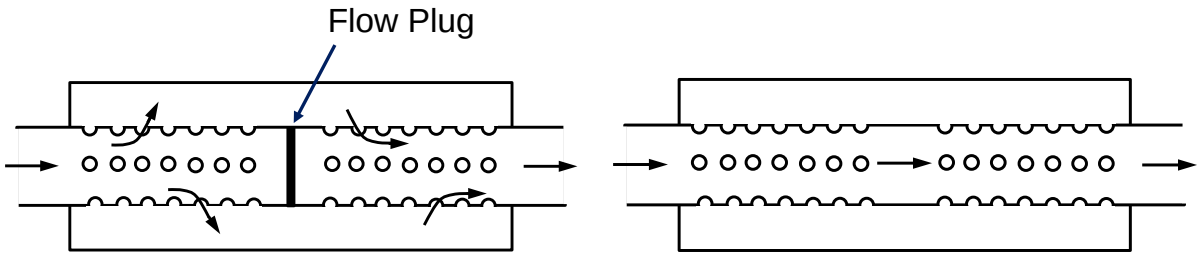

Figure 3.8 Comparison of perforated tubes with penetrating flow (left) and grazing flow (right).

The penetrating flow is usually treated by modifying the acoustic particle velocity in Crandall's theory. Dean (1976) replaced the acoustic particle velocity with the penetrating flow velocity by assuming the flow velocity to be much greater than the acoustic particle velocity. Other researchers used different algebraic summations of particle velocity and flow velocity to replace the particle velocity

(Chung, 1978, Premo, 1999). Bauer's model treated penetrating flow by directly multiplying a factor of 1.15 M to resistance (Bauer, 1977), where M is the Mach number for the penetrating flow through the perforated holes. Sullivan (1979) developed an empirical formula including the effect of the penetrating flow in perforate tubes. The transfer impedance was expressed as

$$z_{tr} = \frac{1}{\sigma}\left[0.514\frac{d_1 M}{l\sigma} + j0.95k\left(t + 0.75d\right)\right] \tag{3.1.16}$$

where d_1 is diameter of the perforated tube, M is the mean flow mach number in tube, l is the length of perforate, σ is porosity, k is wave number, t is thickness of the tube, and d is hole diameter.

Elnady (2003) explained that grazing flow reduces the end effects and results in a decrease of the so-called attached mass. This implies that some of the stored kinetic energy in the oscillating medium across the orifice is lost. This results in an increase in resistance and decrease in the reactance. Lee and Ih (2003) also found that the magnitude of the resistance increases as the mean grazing flow Mach number increases, and that the rate of decrease of resistance with frequency is nearly the same for every Mach number condition. Kooi and Sarin (1981) proposed an empirical equation for an end correction modification factor to represent the effect of grazing flow. The factor is the ratio of end correction length at the grazing flow condition to that in the absence of the grazing flow. Later, Cummings (1986) modified Kooi's empirical impedance model suggest a more general equation.

Rao and Munjal (1986) proposed an empirical model, considering all involved parameters such as diameter and thickness of the perforate, porosity, and grazing mean flow velocity. The grazing flow effect was limited to only the resistive term. The normalized acoustic impedance was given by:

$$z_{tr} = \frac{1}{\sigma}\left[7.337\times10^{-3}\left(1+72.23M\right) + j2.2245\times10^{-5} f\, 0.514\left(1+515\right)\left(1+204d\right)\right] \tag{3.1.17}$$

where f is the frequency.

3.1.5 Nonlinearity under high sound pressure level

In most prior impedance models, linearity has been assumed. Thus, the impedance has been assumed to be independent of the sound pressure level. However, in practice, transfer impedance is sensitive to the incident sound pressure once the sound pressure level reaches a certain level. The exact level will depend on dimensions of the perforate. For most perforated panels, the changes in impedance become apparent when SPL is above 130 dB. High sound pressure levels increase the real part of the resistance and decrease the reactance. (Melling, 1973).

At high sound pressure level, the acoustic particle velocity induces vortex shedding and forms a “jet” at the exit of the aperture. In the nonlinear regime, the pressure difference has a component which is in phase with the particle velocity, resulting in acoustic energy loss. The loss results from the kinetic energy of the jet being dissipated by turbulence (Elnady, 2003).

Based on the measurement of particle velocities and driving sound pressures, Ingard (Ingard and Ising, 1967) observed that for particle velocity above some threshold level, the sound pressure in the opening is proportional to the squared velocity, i.e. $p \approx \rho_0 u^2$. According to Bernoulli’s equation, at low sound pressure levels, the resistive component is proportional to the velocity amplitude

$$R_{tr} \approx \rho_0 u \ . \tag{3.1.18}$$

According to Ingard's equation, this resistance is independent of frequency.

For reactance, Ingard an Ising (1967) proposed that the mass reactance decreases and approaches a value of approximately one-half of the linear value. Melling (1973) derived the nonlinear impedance as a function of velocity:

$$R_{tr} \approx \frac{4\rho_0}{3\pi} u \tag{3.1.19}$$

Melling related the reactance to the perforate constant. He derived function of a combination of three important parameters, namely perforate constant, ratio of plate thickness to hole diameter and square root of porosity. For most samples measured, the mass reactance could be approximated as 220 Rayls for mass reactance of perforated panels.

Perforates are normally characterized by their transfer impedance. Section 2.3 summarized the measurement of transfer impedance. The transfer impedance of perforates has been measured using a variety of approaches. Melling (1973) measured the transfer impedance of perforates at single frequencies using one microphone in front of sample and one microphone at the back wall of the impedance tube. Lee and Kwon (2004) and Tao et.al (2005) calculated the transfer impedance based on measuring four-poles.

An alternative measurement method is impedance subtraction method, which is similar to two-cavity method (Wu, 2003). For instance, transfer impedance of a perforated plate with 1.4 mm hole diameter, 1mm panel thickness and 2.5% porosity was measured using the impedance subtraction method. Measured resistance and reactance are shown in Figure 3.9. Notice that the resistance is usually small for perforated panel with hole diameter larger than 1mm.

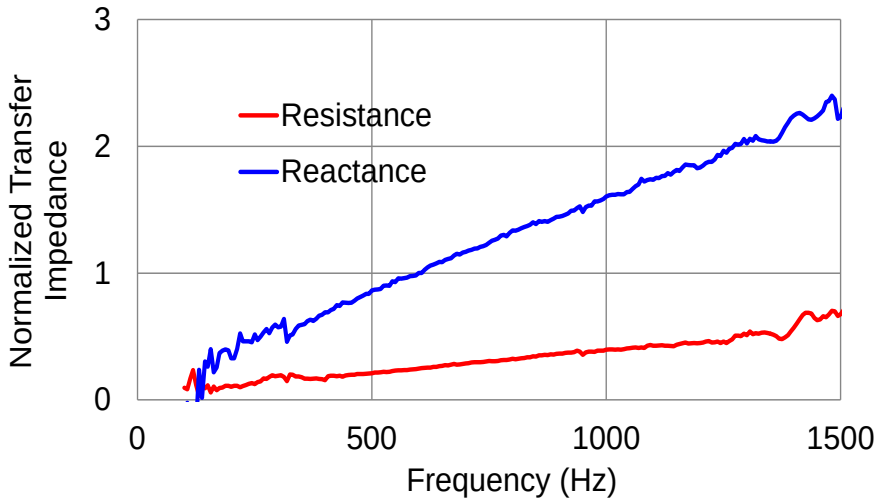

Figure 3.9 Measured transfer impedance of perforated panel using impedance subtraction method.

3.2 Modeling and measurement of micro-perforated panels

Traditional sound absorbing materials like fiberglass and foam deteriorate over time and are non-renewable. Small particles become dislodged travelling through ventilation ducts reducing the air quality inside of buildings. Though the

long term health effects are unknown, it is recommended that exposure to these materials is minimized. Certainly, alternative materials should be used in both health and food processing facilities. Sometimes facings are introduced to fiberglass and foam to prevent deterioration and to guard against dirt and oil being trapped. However, these facings are combustible and typically reduce the sound absorbing capabilities.

One of the more attractive alternatives to fibers and foams are micro-perforated panel (MPP) absorbers. For macro-perforated panels, pore diameters are on the order of millimeters or even centimeters with little acoustic resistance. MPP absorbers have pore diameters sub-millimeter in size. Due to the small holes, MPP absorbers provide acoustic resistance which enhances the sound attenuation.

MPP absorbers are normally manufactured from plastic or metal. In the past, holes were circular in shape and were cut using a laser. Consequently, MPP absorbers were considered to be too costly for commercial uses. Manufacturers have recently developed lower cost micro-slit panel (MSP) absorbers. Slits are non-circular and are cut or pressed into metal or plastic. Maa determined that micro-slit absorbers have a slightly smaller acoustic resistance, but function like MPP absorbers for all practical purposes (Maa, 2000). Figure 3.10 is a photograph showing a MPP and MSP sample.

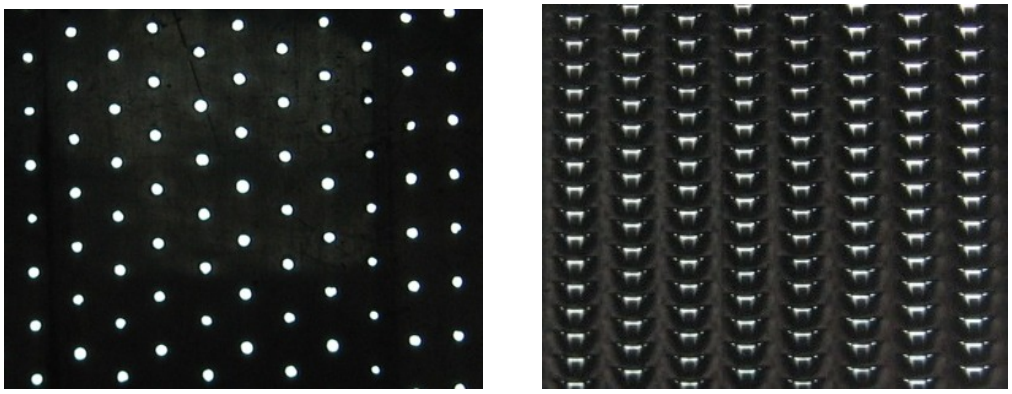

Figure 3.10 Photographs of MPP and MSP under light.

Due to its unique properties, MPP absorbers have been utilized in construction equipment, building interiors, HVAC ducts and mufflers etc.

Probably, the most noteworthy example is their utilization in the Deutscher Bundestag (the New German Federal Parliament Building). Fuchs and Zha (1997) developed an acrylic-glass MPP absorber, the first transparent sound absorber in the world. This novel MPP absorber provided the required diffusivity of the sound field in the parliament hall while preserving the architectural design intention to achieve transparency and 'clarity'. Since MPP absorbers are fiber-free, they can be used to replace fibrous materials in clean environments or equipment. For example, MPP absorbers can be used in HVAC systems in medical, food processing and microelectronics manufacturing facilities (Wu, 1997). Li and Mechefske (2010) reported utilized MPP absorbers to reduce the noise of magnetic resonance imaging (MRI) equipment.

As mentioned earlier, MPP absorbers are rugged, non-combustible and do not deteriorate over time. This makes them a very attractive option for long-term use in harsh and corrosive environments. For example, MPP absorbers have been used in noise barriers on mining sites (Pan, 2004), in engine enclosures as an acoustical heat shield (Corin and Weste, 2005), and inside mufflers (Masson, 2008).

The following sections review MPP absorber theory and measurement.

3.2.1 Theoretical modeling

Similar to macro-perforated panel theory, Maa (1975, 1997, 1998) considered the MPP as a lattice of short narrow tubes, separated by distances much larger than their diameters though small compared to the wavelength of the impinging sound wave. Building on the tube model of Lord Rayleigh (1945), and Crandall's (1927) simplifications for viscous effects in narrow short tubes, Maa developed a theoretical model for the transfer impedance of an MPP.

Maa used the same expression as Equation 3.1.7 for impedance of a single tube. For most micro-perforated panels with hole diameter of 0.1 mm to 1 mm, the perforate constant is between 1 to 10. Thus, neither Equation 3.1.8 nor Equation 3.1.9 is suitable to represent the transfer impedance. Maa developed a

solution based on simplifying the Bessel functions for perforate constants between 1 and 10, written as

$$z = \frac{32\eta t}{d^2}\sqrt{1+\beta^2/32} + j\omega\rho_0 t\left(1+1/\sqrt{9+\beta^2/2}\right) \tag{3.2.1}$$

Maa used Ingard's end correction model for resistance and reactance (see Table 3.1).

For micro-perforated panels with sub-millimeter holes and low porosity, individual holes can be viewed as sufficiently spaced apart. Therefore, interaction between adjacent holes can be ignored in this case. For normal incidence sound waves, the wave motion in all the short tubes is in-phase and additive. By averaging impedance over the entire panel, the normalized transfer impedance of the MPP can be expressed as

$$z_{tr} = \frac{32\eta t}{\sigma\rho_0 c d^2}\left(\sqrt{1+\beta^2/32} + \frac{\sqrt{2}}{32}\beta\frac{d}{t}\right) + j\frac{\omega t}{\sigma c}\left(\left(1+1/\sqrt{9+\beta^2/2}\right)+0.85\frac{d}{t}\right) \tag{3.2.2}$$

where ω is the angular frequency, c is the speed of sound, d is hole diameter, t is panel thickness, σ is porosity, and β is a perforate constant dependent on the properties of the fluid. β is given as $\beta = d\sqrt{\omega\rho/4\eta}$, where η is the viscosity and ρ is the mass density of air.

MPP absorbers always require a rigid wall and a spacing D as shown in Figure 3.11. By arranging a plate containing holes smaller than 1 mm in front of this "air cushion", the vibration of the air (i.e. the sound) in the very small holes is damped by shearing forces and a relatively broadband absorber can be created. The surface impedance for a MPP plus air cavity combination can be expressed as

$$z = z_{tr} - j\cot\frac{\omega D}{c} \ . \tag{3.2.3}$$

Once the surface impedance is determined, the reflection coefficient and absorption coefficient can be calculated.

The cavity depth (D) determines the frequency range in which the MPP is most effective. MPP absorbers have maximum attenuation when the particle velocity

in the pore is high. This will occur at approximately one-quarter acoustic wavelength from a rigid wall. (when the particle velocity is maximized). Therefore, Thus, MPP absorbers are easily tuned by varying the cavity depth.

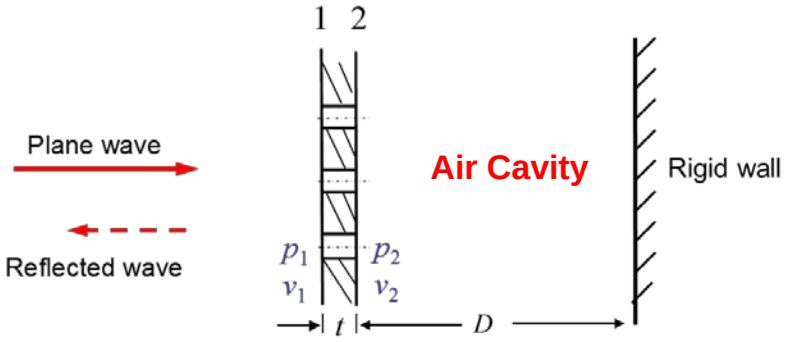

Figure 3.11 Schematic of MPP and adjoining air cavity.

For slit-shaped perforated panels, Allard (1993) developed exact formulae for the acoustical impedance. Maa (2000) applied the formulae and developed an expression for the transfer impedance of MPP absorbers with slit-shaped perforations. The transfer impedance of a single micro-slit with length and width of $2l$ and $2a$, respectively is shown in Equation 3.1.11. For perforate value between 1 and 10, the approximate equation is

$$z = \frac{12\eta t}{d^2}\sqrt{1+\beta^2/18} + j\omega\rho_0 t\left(1+1/\sqrt{25+2\beta^2}\right) \tag{3.2.4}$$

Maa used Ingard's end correction model for the resistance, which is $\frac{1}{2}\sqrt{2\omega\eta\rho_0}$. For the reactance, Maa treated the rectangular opening with length of $2l$ and width of $2a$ as an elliptical opening. The added length of a rectangular opening can be approximated by:

$$\delta = \frac{1}{2}d \cdot F(e) \tag{3.2.5}$$

where e is the eccentricity for an ellipse which can be calculated as $\sqrt{1-\frac{a^2}{l^2}}$, and F is the incomplete elliptic integral of the first kind and is expressed as

$$F(e)=\int_0^{\frac{\pi}{2}}\frac{d\theta}{\sqrt{1-e^2\sin^2\theta}}\ . \qquad (3.2.6)$$

By averaging impedance over whole panel, the normalized transfer impedance of the MPP with slit-shaped perforation can be expressed as

$$z_{tr}=\frac{12\eta t}{\sigma\rho_0 c d^2}\left(\sqrt{1+\beta^2/18}+\frac{\sqrt{2}}{12}\beta\frac{d}{t}\right)+j\frac{\omega t}{\sigma c}\left(1+1\Big/\sqrt{25+2\beta^2}+\frac{1}{2}F(e)\frac{d}{t}\right) \qquad (3.2.7)$$

the transfer impedance for circular and slit shaped perforations (Equations 3.2.2 and 3.2.7 respectively) , it is evident that the resistive part for slit-shaped perforations is smaller whiled the reactive part is larger. This change in transfer impedance usually results in a lower sound absorption coefficient. In order to improve the acoustic performance of MPP absorbers with slit-shaped perforations, Maa (2000) proposed an improved design with smaller slit widths and larger panel thicknesses to compensate for the lower resistances.

Maa (2000) also developed equations for slit-shaped perforations in high sound pressure environments. High sound intensity/pressure levels lead to high particle velocity (u_0) in and around the hole, which leads to “jet” loss in the hole. Particle velocity in the hole can be calculated as a function of the sound pressure and is expressed as:

$$u_0=\frac{\sigma c}{2}\left(\sqrt{(1+r_0)^2+\frac{8p}{\rho_0\sigma^2c^2}}-(1+r_0)\right) \qquad (3.2.8)$$

where r_0 is the resistive part of the transfer impedance as shown in Equation 3.2.2.

“Jet” losses increase the resistance end correction by $\frac{u_0}{\sigma c}$, and reduce the reactance end correction by $\left(1+\frac{u_0}{\sigma c}\right)^{-1}$. The transfer impedance for MPP absorbers under high sound pressure level is given by:

$$z_{tr}=\frac{32\eta t}{\sigma\rho_0 c d^2}\left(\sqrt{1+\beta^2/32}+\frac{\sqrt{2}}{32}\beta\frac{d}{t}\right)+\frac{u_0}{\sigma c}+j\frac{\omega t}{\sigma c}\left(\left(1+1\Big/\sqrt{9+\beta^2/2}\right)+0.85\frac{d}{t}\left(1+\frac{u_0}{\sigma c}\right)^{-1}\right) \qquad (3.2.9)$$

For a MPP absorber with 0.25 mm diameter, 0.3 mm thickness, 1% porosity and 25 mm cavity depth, the transfer impedance and absorption coefficient under different sound pressure levels are simulated using Equation 3.2.9. The results are compared in Figure 3.12 and measured results are shown in Figure 3.13. It can be observed from the simulated and measured results that high sound pressure levels increase transfer resistance and compromise the absorbing ability of a MPP absorber.

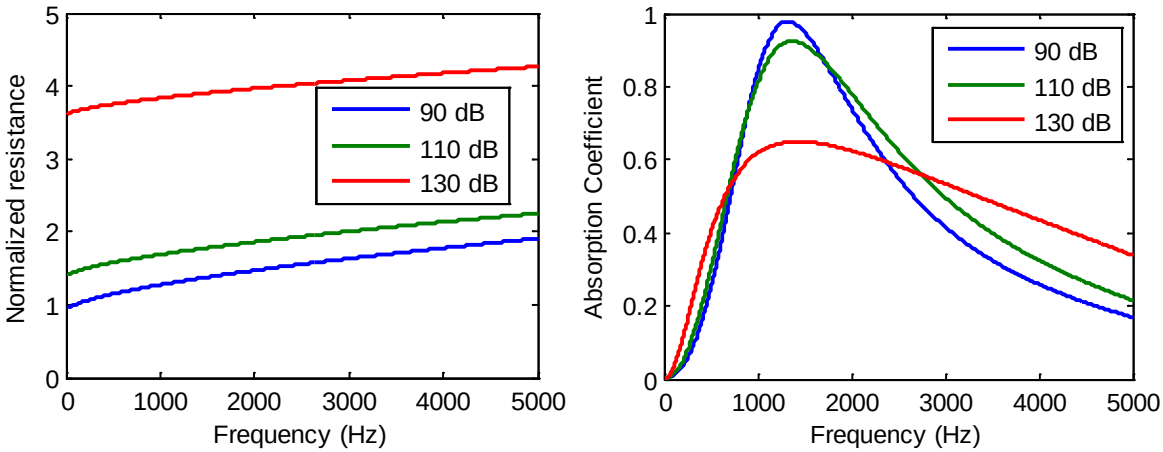

Figure 3.12 Simulated transfer resistance (left) and absorption coefficient (right) of MPP absorber under different sound pressure levels.

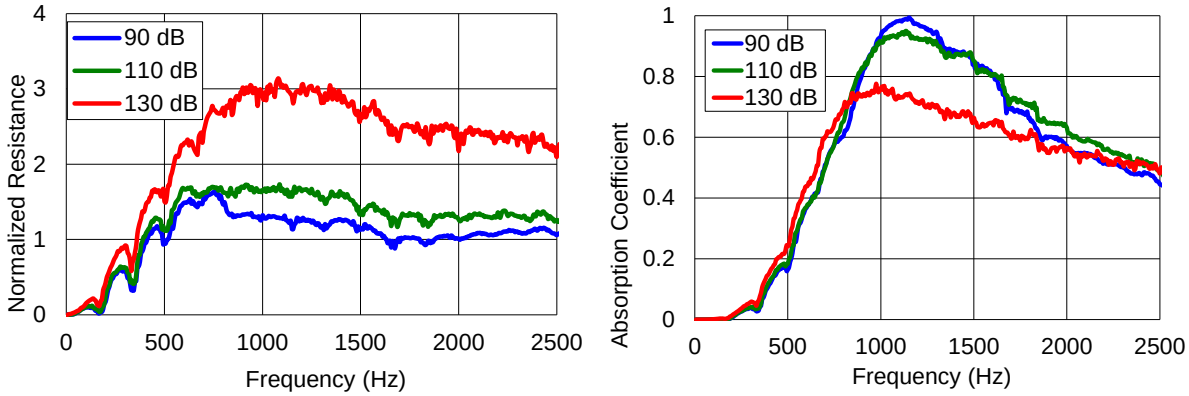

Figure 3.13 Measured transfer resistance (left) and absorption coefficient (right) of MPP absorber under different sound pressure levels.

Since micro-perforated panels can be categorized as a special type of transfer impedance, measurement methods of transfer impedance described in chapter 2 can be applied to micro-perforated panels. The simplest method to measure the transfer impedance was the impedance subtraction method developed by Wu et.al (2003).

Alternatively, transfer impedance can be calculated from reflection coefficient using Equation 2.3.3 and 2.3.4 once transfer matrix is measured using two load or two source methods (Yoo, 2008).

3.2.2 The Transfer matrix of For MPP Absorbers and its applications

Once the transfer impedance is either predicted or measured, the transfer matrix can be expressed as

$$T = \begin{bmatrix} 1 & z_{tr} \\ 0 & 1 \end{bmatrix} \tag{3.2.10}$$

This matrix can be utilized to estimate the performance of composite absorbers and can also be used in numerical models. For example, Lee and Kwon (2004) and Tao (2005) calculated the sound absorption of multiple MPP absorbers separated by air cavities. Liu (2008) calculated the sound absorption of composite absorbers consisting of foams and micro-perforated panels. For example, a multiple-layer micro-perforated panel absorber is shown in Figure 3.15. Its overall transfer matrix can be obtained by multiplying the individual transfer matrices for each perforated panel and airspace. The overall transfer matrix can be expressed as

$$T_{\text{overall}} = T_{\text{MPP1}} \cdot T_{\text{Airspace1}} \cdot T_{\text{MPP2}} \cdot T_{\text{Airspace2}} \tag{3.2.11}$$

where T_{MPP1} and T_{MPP2} are transfer matrices for the first and the second panel, respectively. $T_{\text{Airspace1}}$ and $T_{\text{Airspace2}}$ are transfer matrices for the cavities behind the first and the second panel, respectively. Since this absorber is placed against a rigid termination, the particle velocity at the termination is zero ($u_0 = 0$).The surface impedance can be expressed as

$$z_1 = \frac{p_1}{u_1} = \frac{T_{11}}{T_{21}} \tag{3.2.12}$$

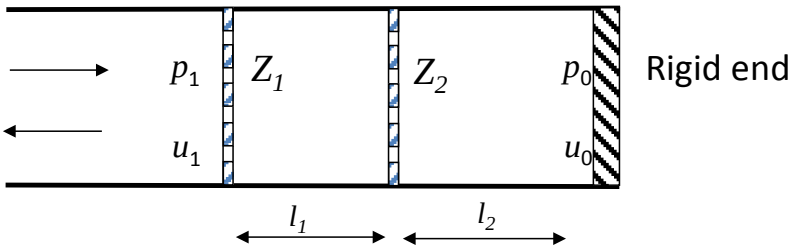

Figure 3.15 Configuration of multiple-layer micro-perforated panel absorber.

Once the surface impedance is obtained, the absorption coefficient can be calculated. Figure 3.16 compares the measured and predicted absorption coefficient for the double-layer MPP absorber. The predicted results agree well with the measured.

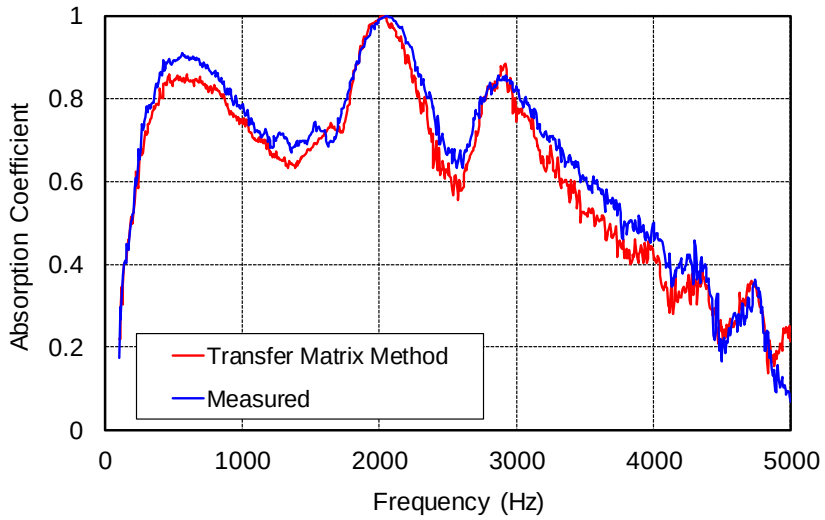

Figure 3.16 Absorption coefficients of double layer micro-perforated panel absorber (Tao, 2005).

3.2.3 Effect of geometric parameters

For a single layer MPP absorber with air cavity behind it, as illustrated in Figure 3.11, its transfer impedance and surface impedance are calculated using Equations 3.2.2 and 3.2.3, respectively. By examining these two equations, it can be shown that the performance of a MPP absorber depends mainly on the hole

diameter, panel thickness, porosity and cavity depth. Wu (1997) conducted a parametric study experimentally. In the current work, the different parameters are varied using Equation 3.2.3The trends from both studies were comparable. Naturally, the advantage of the simulation is that a wide range of parameters can be examined without conducting time-consuming experiments. Each of the design parameters were varied while holding the other parameters constant.

Figure 3.17 shows the effect of varying hole diameter with all other parameters held constant. All other parameters were held constant (D = 25 mm; t = 0.4 mm; σ = 1.5%). The left plot is a contour map of absorption coefficient with respect to frequency and hole diameter. The right plot shows absorption coefficient curves for three distinct hole diameters extracted from the contour map. Notice that the attenuation band can be broadened by reducing the hole diameter. Smaller holes increase the viscous friction which in turn improves the sound absorption. For the parameters selected, the optimum range for hole diameter is between 0.4 and 0.6 mm.

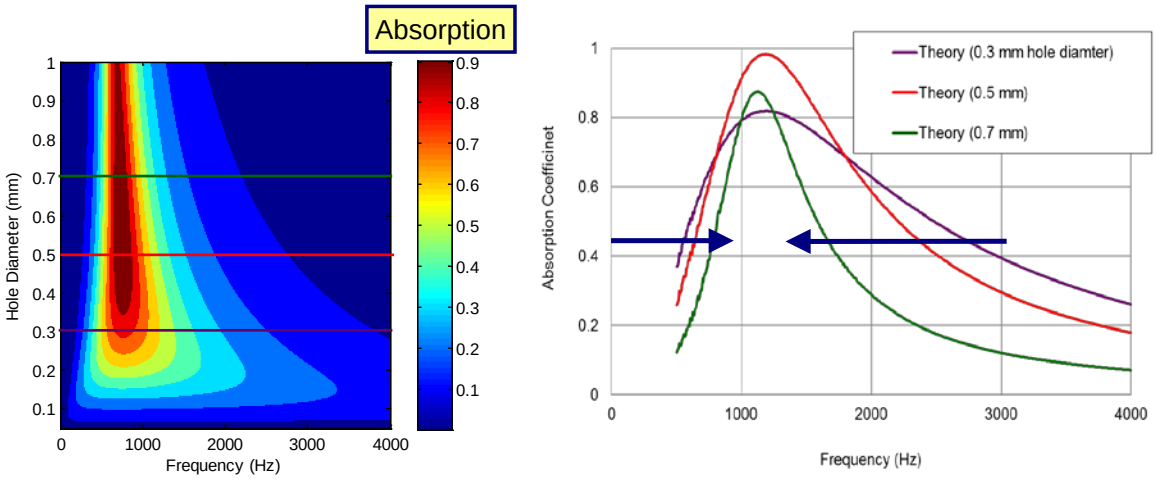

Figure 3.17 Effect of hole diameter on absorption coefficient: contour map (left) and absorption coefficient curves for several diameters (right).

Figure 3.18 shows the impact of porosity on the absorption. Other parameters were held constant and the porosity was varied from 0 to 3 percent. Notice that the increasing porosity forces the central frequency of the absorption

coefficient band higher in frequency. However, porosity will not greatly impact the absorption coefficient provided that modifications are small.

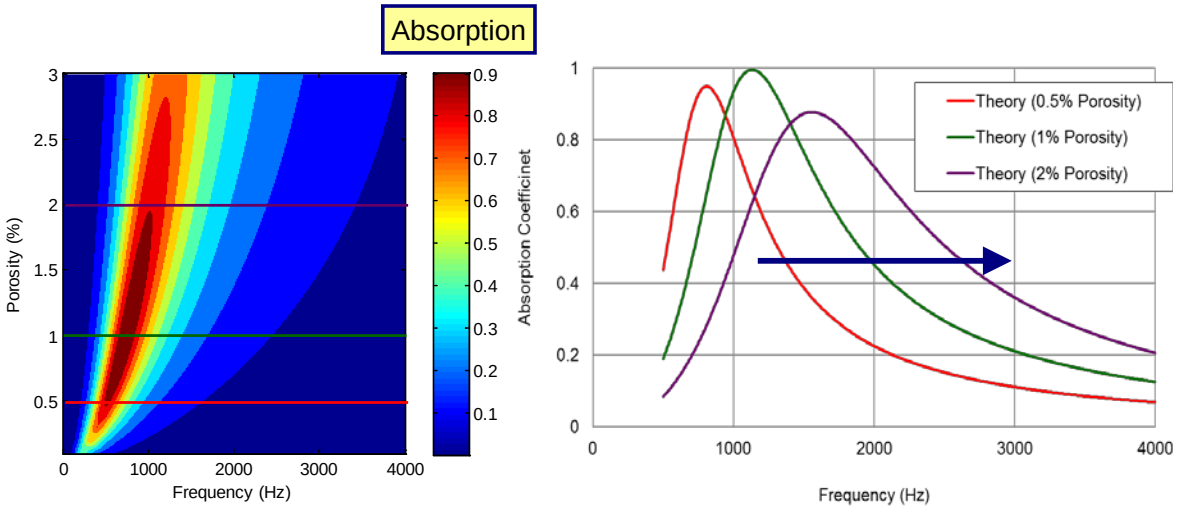

Figure 3.18 Effect of perforation porosity on absorption coefficient: contour map (left) and absorption coefficient curves for several porosities (right).

Figure 3.19 shows the impact of panel thickness on the absorption. Other parameters were held constant and the thickness was varied from 0 to 2 mm. Notice that increasing thickness forces the central frequency of the absorption coefficient band slightly lower in frequency. However, thickness will not greatly impact the absorption coefficient provided changes are small. Wu (1997) explained that the end correction is on the same order or larger than the thickness for most MPP absorbers. Since the thickness of micro-perforated panels is usually very close to the hole diameter, the total thickness including end correction is 1.7 times the geometric length of the orifice. As a result, doubling the panel thickness only increases the total effective thickness of the panel by 37%. Therefore, increasing or reducing the panel thickness has a small effect on the acoustic panel resistance.

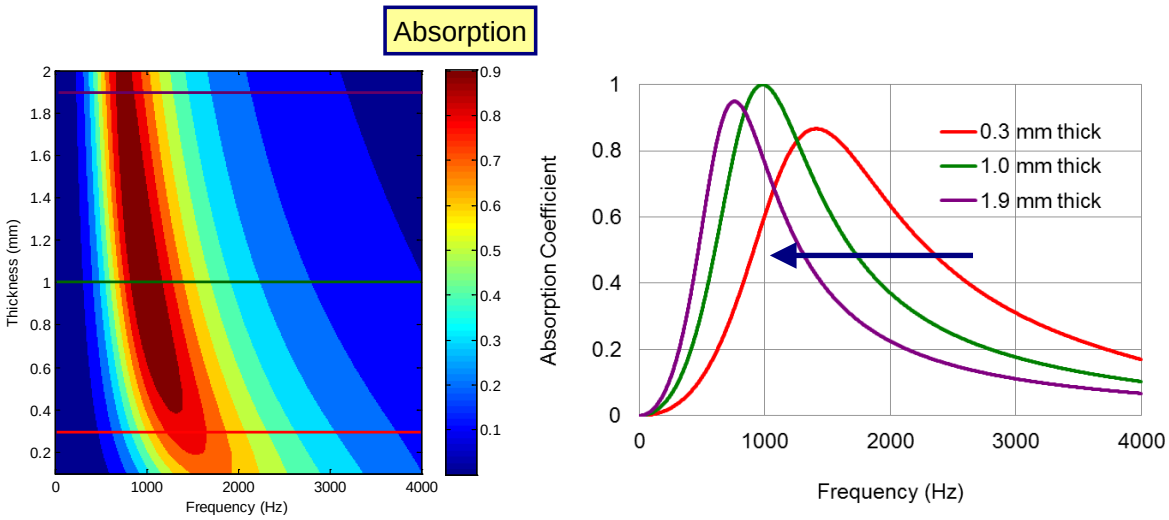

Figure 3.19 Effect of panel thickness on absorption coefficient: contour map (left) and absorption coefficient curves for several panel thicknesses (right).

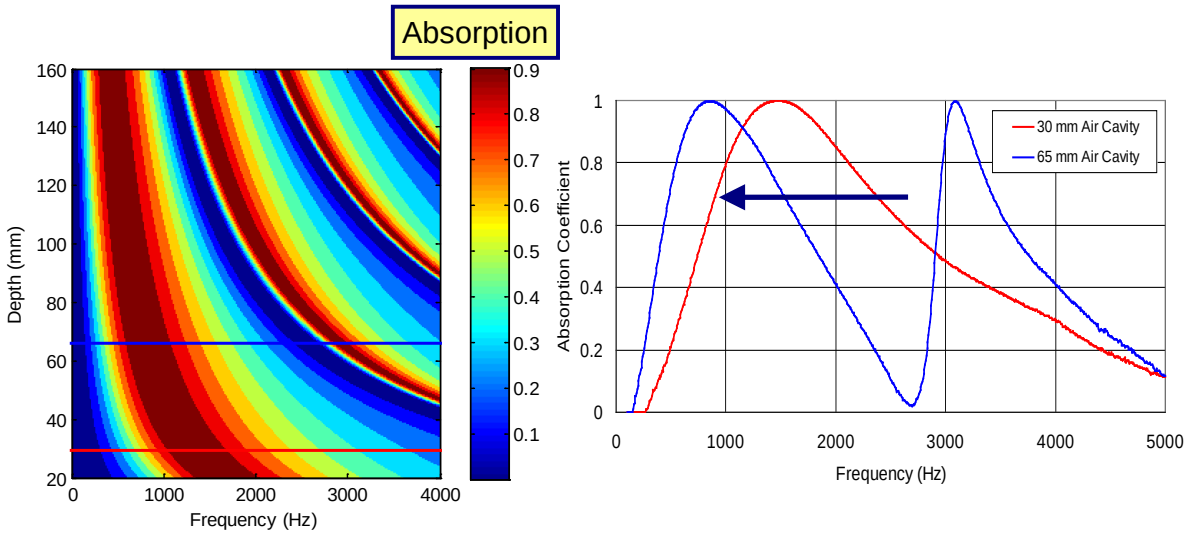

Figure 3.20 Effect of cavity depth on absorption coefficient: contour map (left) and absorption coefficient curves for two cavity depths (right).

Figure 3.20 shows the effect of varying the depth of the air cavity from 0 to 160 mm. As the figure indicates, cavity depth determines the frequency range in which the MPP is most effective. Increasing cavity depth forces the central frequency of the absorption coefficient band dramatically lower in frequency. The MPP absorber will have the maximum attenuation when the particle velocity in the pore is high. The first attenuation peak is approximately one-quarter

wavelength from the rigid wall (when the depth of the cavity is one-quarter wavelength) if it is assumed that the MPP is a purely resistive locally reacting element. Higher order peaks occur for cavity depths that correspond to odd numbers of quarter wavelengths. In practice, the peak is always shifted a little to lower frequency because of the reactive part of the impedance.

CHAPTER 4
SOURCE IMPEDANCE

4.1 Introduction

In duct acoustics, Transmission Loss (TL) is defined as the difference between the power incident to a muffler (or more generally any sound attenuating element) and that transmitted downstream. In the plane wave regime, it is a property of the attenuating element itself and not the complete exhaust system. In fact, the reported transmission loss for an attenuating element may bear little resemblance to its performance as a component in an actual exhaust system.

In practice, insertion loss, defined as the difference between the radiated sound power with and without the attenuating element, is preferred for assessing the performance. Insertion loss is dependent on the attenuating element, but is also sensitive to the source and termination characteristics.

While transmission loss in many instances can be easily predicted using plane wave theory or simulation, insertion loss is more easily measured. For example, in small engine applications, a number of different attenuation elements are fabricated, placed into the exhaust system, and then their corresponding radiated sound pressures are measured in order to compare their respective insertion losses.

Though an analytical procedure would be preferred, this is predicated on not only obtaining a realistic model of the attenuating element, but also a realistic representation of the source and termination. Insertion loss of an attenuating element is a function of transfer matrix, and source and termination impedances. The insertion loss (IL) of an attenuating element is expressed as (Munjal, 2006):

$$IL = 20\log\left|\frac{T_{11}\cdot z_T + T_{12} + T_{21}\cdot z_s z_T + T_{22}\cdot z_s}{D_{11}\cdot z_T + D_{12} + D_{21}\cdot z_s z_T + D_{22}\cdot z_s}\right| \tag{4.1.1}$$

where T_{11}, T_{12}, T_{21}, T_{22} are transfer matrix elements of the attenuating element, and D_{11}, D_{12}, D_{21}, D_{22} are transfer matrix elements of the replaced straight duct,

and z_T and z_s are the respective termination and source impedances. Note that both source and termination impedances are series impedances.

Sound pressure level at the outlet of the duct system can be calculated based on overall transfer matrix, source strength, source impedance, and termination impedance, as

$$L_{outlet} = 20\log\left|\frac{p_s \cdot z_T}{\left(T_{11} \cdot z_T + T_{12} + T_{21} \cdot z_s z_T + T_{22} \cdot z_s\right) \cdot 2\times 10^{-5}}\right| \tag{4.1.2}$$

where p_s is source strength (Munjal, 2006).

While the termination can often be estimated using handbook equations, source characteristics are determined experimentally. Realistic sources, such as internal combustion engines, fans, or even loudspeakers can be characterized by their source impedance and source strength, as described in chapter 2. Both quantities are determined experimentally assuming that the source is time invariant and propagates sound according to the plane wave assumption. While measuring the source strength is essential when predicting the radiated power, source strength is unimportant for predicting insertion loss.

The acoustic source impedance concept was initially developed by making an analogy to electrical systems (Munjal, 1987). The source strength and the source impedance are analogous to the voltage and the internal impedance respectively of an electrical source. Referencing Figure 4.1, the relationship between source and load is:

$$\frac{p_s}{z_s + z_L} = \frac{p_L}{z_L} \tag{4.1.3}$$

where p_s and z_s are the source strength and source impedance, respectively; p_L and z_L are the load sound pressure and load impedance, respectively.

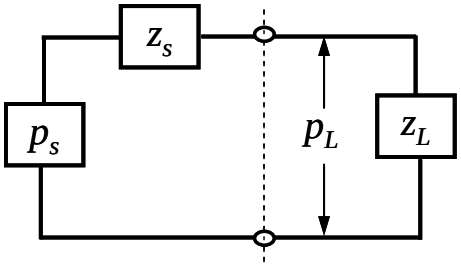

Figure 4.1 Equivalent circuit analogy for acoustic source impedance.

While useful, this analogy is not an ideal representation of the acoustic system. First of all, the source strength (p_s) must be measured or simulated except in the case of idealized sources. In addition, sound pressure, using the electric analogy, cannot be decomposed into incident and reflected sound waves (Davies, 1991).

In order to develop the source model based on acoustical concepts, an intermediate model based on the mechanical-acoustical coupling analogy is introduced. As shown in Figure 4.2, the source can be represented by a spring-mass-damper system driven by the source pressure on the left side. On the right side, the mass acts like a piston, which drives the acoustic system.

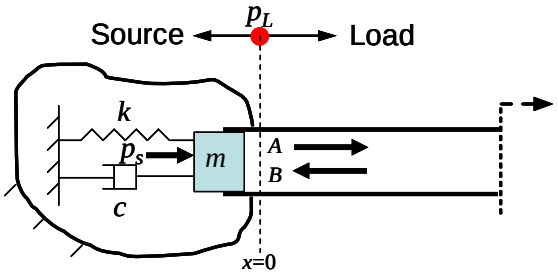

Figure 4.2 Schematic illustrating the mechanical analogy of a source.

The coupled system shown above can be described as:

$$\left[c + j\left(\omega m - \frac{k}{\omega}\right) + \frac{s \cdot p_l}{u_0}\right] \cdot u_0 = s \cdot p_s \quad . \tag{4.1.4}$$

By defining source impedance using mechanical concepts, as shown in Equation 4.1.5, and load impedance based on acoustical concepts, as shown in Equation 4.1.6, Equation 4.1.4 can be proven identical to Equation 4.1.3. Therefore, instead of using equivalent circuit analogy, the mechanical-acoustical

coupling analogy can be employed in the future to aid in better understanding the source impedance. The source and load impedances can be expressed as

$$z_s = \frac{z_m}{s} = \frac{\left[c + j\left(\omega m - \frac{k}{\omega} \right) \right]}{s} \tag{4.1.5}$$

and

$$z_l = \frac{p_l}{u_0} \ . \tag{4.1.6}$$

respectively. Figure 4.3 illustrates the effect of source impedance inside of a waveguide. The sound waves generated by the source propagate along the duct. While a portion of the energy propagates through the attenuating element, some of the energy is reflected by the attenuating element back towards the source. The reflected sound waves though partially absorbed by the source also reflect back from the source. The amount of sound energy reflected or absorbed by the source is a function of the source impedance.

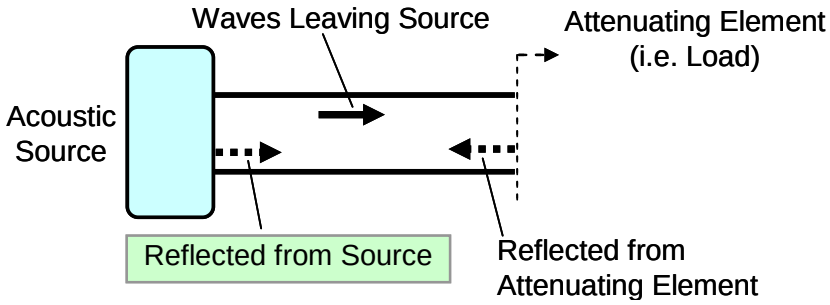

Figure 4.3 Schematic illustrating the behavior of a realistic source.

4.2 Measurement methods based on electrical analogy

As described in Chapter 2, due to the practical difficulties of a direct measurement, indirect methods are often preferred. Figure 4.4 shows a schematic for the indirect measurement approach. Referring to Figure 4.1 and Equation 4.1.3, the source sound pressure and impedance can be solved if two sets of load impedances (z_L) and acoustic pressures (p_L) are known. This is

known as the two-load method in which the minimum of two loads is used to solve for the unknown source sound pressure and impedance. If more than two loads are used, one obtains an overdetermined problem which can be useful for reducing the dependence on the load.

The load impedance is most easily changed by adjusting the length L_i. However, the load impedance can also be changed by adding side branches, or adding absorption at the termination. The load impedances (z_{Li}) are normally determined using plane wave theory, but may also be measured. On the other hand, the acoustic pressures (p_{Li}) at the load are measured. Due to temperature and flow concerns, the pressures (p_{ri}) may be alternatively measured outside the pipe. The acoustic pressures (p_{Li}) at the load can be calculated using plane wave theory from the pressures (p_{ri}) measured outside the pipe.

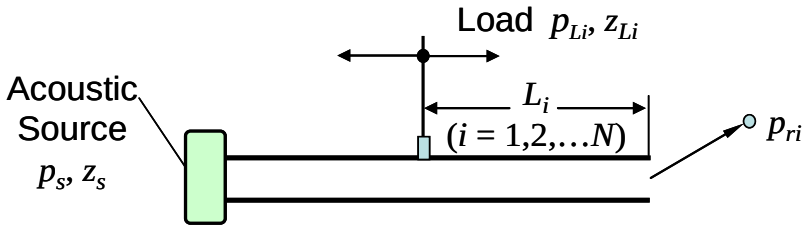

Figure 4.4 Schematic showing the indirect measurement concept.

4.2.1 Two-Load Method

Referencing Equation 4.1.3, with two known load pressures (p_{L1} and p_{L2}) and load impedances (z_{L1} and z_{L2}), the source impedance and source pressure can be expressed as

$$z_s = \frac{z_{L1} z_{L2} (p_{L1} - p_{L2})}{z_{L1} p_{L2} - z_{L2} p_{L1}} \tag{4.2.1}$$

and

$$p_s = \frac{p_{L1} p_{L2} (z_{L1} - z_{L2})}{z_{L1} p_{L2} - z_{L2} p_{L1}} \tag{4.2.2}$$

respectively (Munjal,1987).

Both the load impedance (z_{Li}) and sound pressure (p_{Li}) are complex. In order to establish the phase for the sound pressure (p_{Li}), a non-acoustic reference signal related to the sound-generating mechanism of the source, such as the vibration signal of the engine, is required.

4.2.2 Least Squares Method

Similar to the two-load method, the least squares method takes advantage of additional loads and consequently additional measurement data (Desmons, 1994). It should be noted that other multiple load methods have been developed (Prasad, 1987, Boden, 1995) though the phase of the load pressure (p_{Li}) is often ignored in those approaches.

For the least squares method, the expression for the source impedance is given as

$$z_s = \frac{-\sum_{i<j}\left(\left|u_{L_i} - u_{L_j}\right|^2 \cdot \frac{p_{L_i} - p_{L_j}}{u_{L_i} - u_{L_j}}\right)}{\sum_{i<j}\left|u_{L_i} - u_{L_j}\right|^2} \tag{4.2.3}$$

where u_{Li} is the particle velocity at the load and can be expressed as the ratio of the load pressure (p_{Li}) to the load impedance (z_{Li}). Notice that the load pressures (p_{Li}) should be referenced to a source mechanism since the phase cannot be ignored. Similarly, the source sound pressure can be expressed as

$$p_s = \frac{1}{N}\sum_{i=1}^{N}\frac{p_{L_i}(z_s + z_{L_i})}{z_{L_i}} \quad . \tag{4.2.4}$$

The advantage of the lease squares method is that the source impedance and source sound pressure are less sensitive to the loads because the measurement error is minimized. Nevertheless, care should be taken to insure that the loads are as different as possible.

4.2.3 Move source position

The source impedance provided by the 2-load method or least squares method is usually determined at the microphone position, as shown in Figure 4.5a. However, this source impedance includes the source itself as well as the straight duct between the source and microphone. It is suggested that it is more appropriate to transfer the impedance measured at the microphone position to the actual source position (Figure 4.5b).

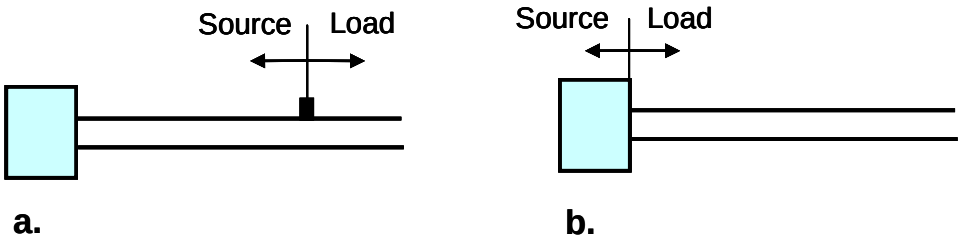

Figure 4.5 Schematic showing how the source position can be moved along a duct.

It is well known that the relationship between the impedances at two positions along the duct, shown in Figure 4.6, can be described using transfer matrix theory (Munjal, 1985, Fahy, 2001). Notice that the source should be regarded as downstream to the load when using the convention described by Fahy (2001) due to the direction in which source impedance is measured.

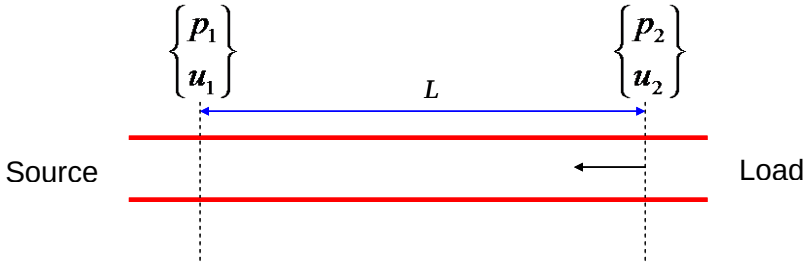

Figure 4.6 Transfer matrix between two positions in a duct.

Thus, the impedance at point 1 (z_1) can be written in terms of the impedance at point 2 (z_2) via

$$z_1 = \frac{z_2 - j\rho c \tan kL}{-z_2 \cdot j\frac{1}{\rho c}\tan kL + 1} \tag{4.2.5}$$

where L is the length shown in Figure 4.6, ρ is the density of air, c is the speed of sound, and k is the wave number. For the case of source impedances, this

amounts to transferring the impedance in the negative direction of incident wave propagation.

4.2.4 Experimental validation

The aforementioned procedure was validated for a loudspeaker. The loudspeaker was connected to an impedance tube as shown in Figure 4.7. The source impedance was measured using the two-load approach and was verified using the direct measurement approach. The load was varied by simply opening and closing the tube at the termination thereby changing the load.

Figure 4.7 Photograph showing the experimental setup.

The measured source impedance comparisons are shown in Figures 4.8 to 4.11 at the microphone and loudspeaker positions respectively. Notice that the source impedance at the microphone position (Figures 4.8 and 4.9) has several peaks as a result of resonances in the tube. In contrast, the source impedance exhibits less resonant behavior when it is measured close to the source itself (Figures 4.10 and 4.11). Also, notice the agreement between the direct and two-load methods. It is believed that the discrepancy at lower frequencies is due to the external source (in this case another loudspeaker) not being powerful enough. It is our opinion that the two-load method is more accurate in this case since the curves in Figures 4.10 and 4.11 are much smoother.

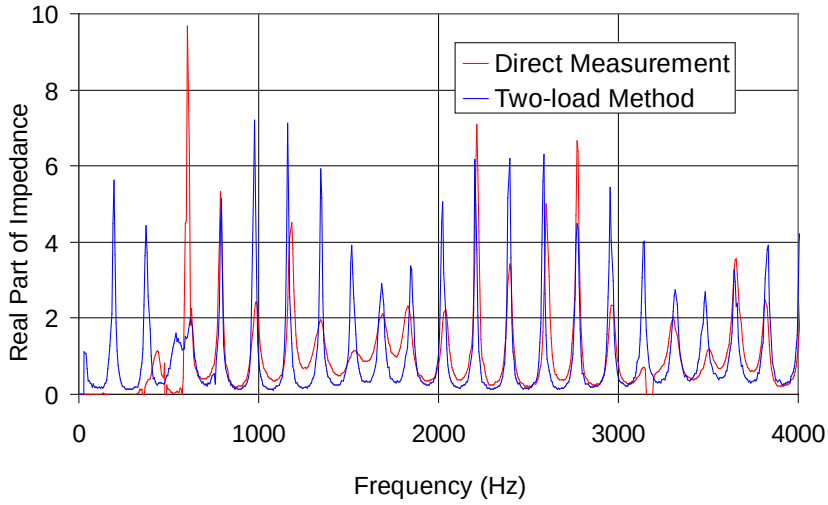

Figure 4.8 Normalized real part of source impedance at microphone position.

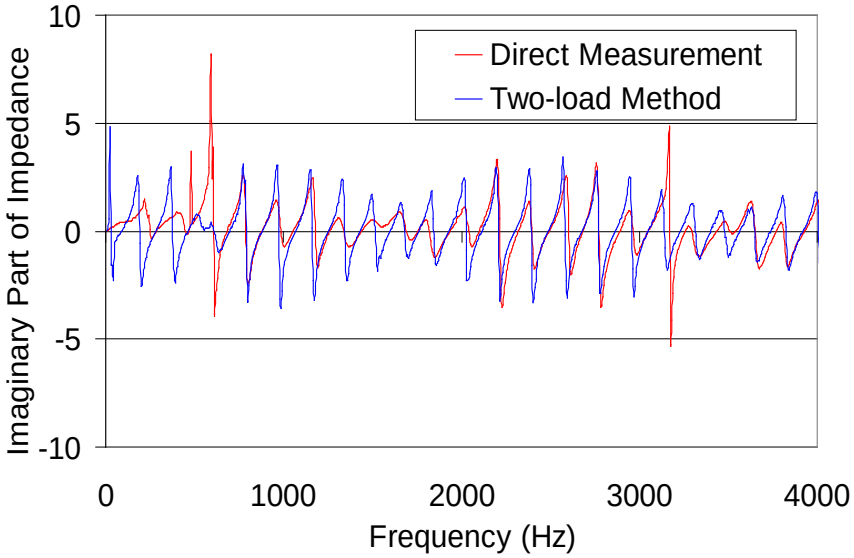

Figure 4.9 Normalized Imaginary part of source impedance at microphone position.

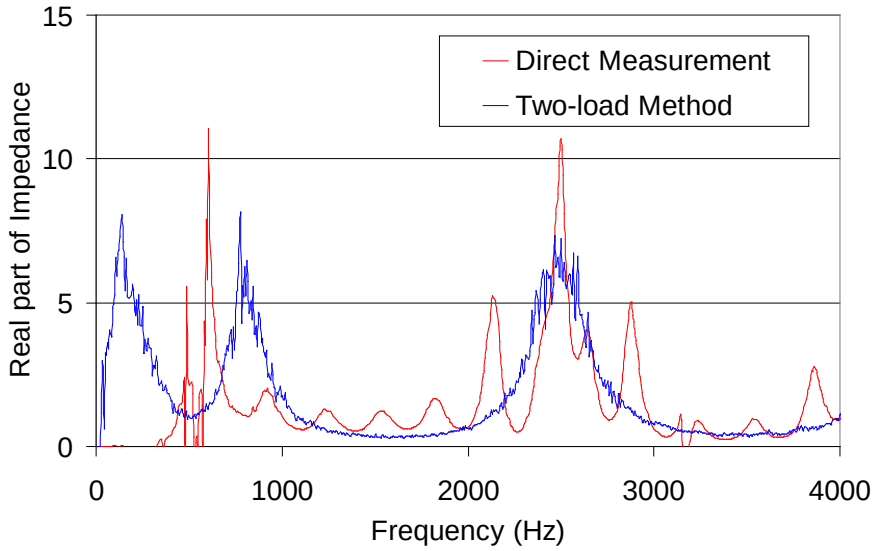

Figure 4.10 Normalized real part of source impedance at loudspeaker position.

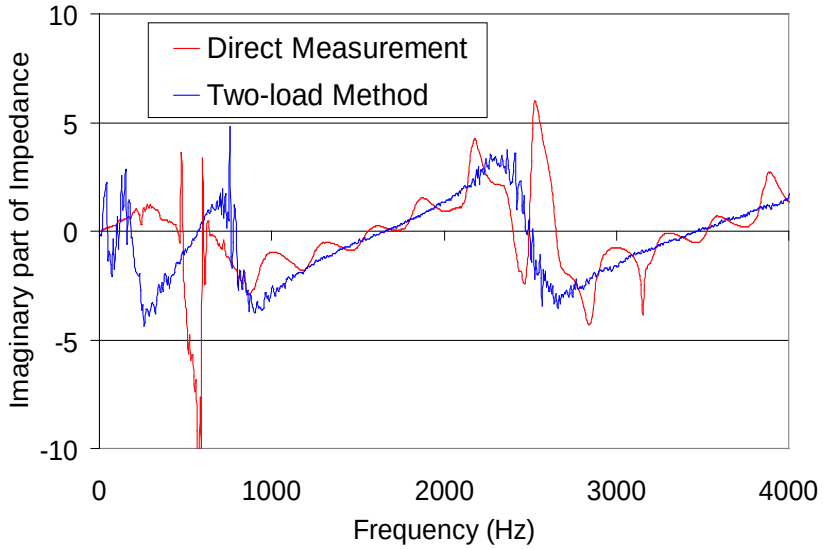

Figure 4.11 Normalized imaginary part of source impedance at loudspeaker position.

4.2.5 Source impedance measurement of engine intake system

The source impedance was measured for a 4-cylinder diesel engine for marine purposes running at 1800 RPM. The intake pipe length is varied to adjust the load. Lengths of 22, 29, 34 and 41 inches were selected. Due to the high

temperature and flow turbulence inside of the pipe, a pressure transducer was used to measure the sound pressure instead of a microphone. The sound pressure measurements were referenced to an accelerometer placed on the engine. Additionally, the sound pressure was measured at the termination so that it could be compared with the sound pressure predicted at the termination using the source strength and the source impedance as a check. The test setup is shown in Figures 4.12 and 4.13.

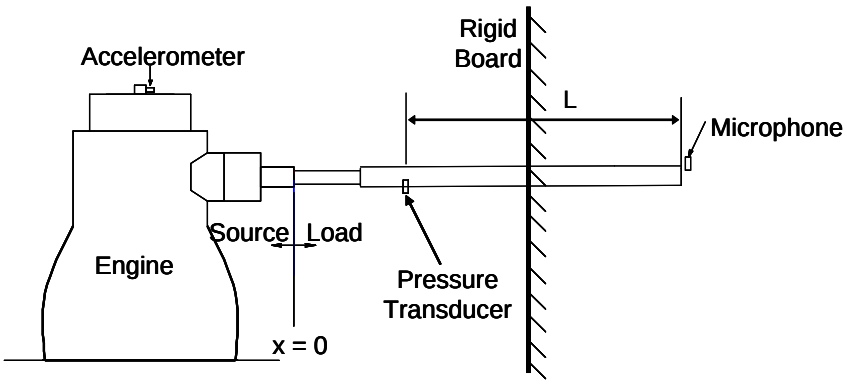

Figure 4.12 Engine intake source impedance measurement setup.

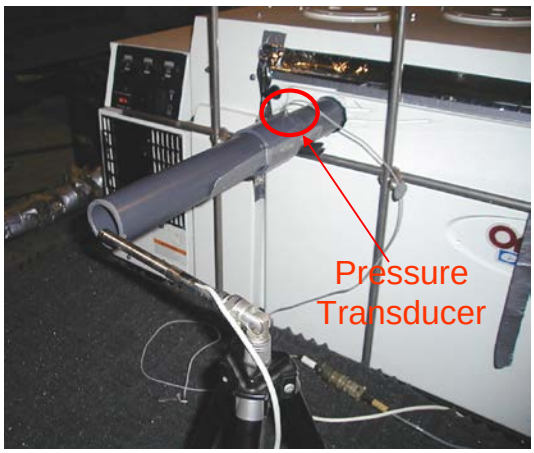

Figure 4.13 Engine intake source impedance measurement.

Four different loads were used which provided 6 different combinations of measurements for the two-load method. This produced six independent predictions for the source impedance. Those results were averaged and compared to the least squares method. For the least squares method, the same measured data from the four different load cases was processed. The source

impedance results measured at the pressure transducer position are shown in Figures 4.14 and 4.15. Notice that the two different processing schemes produce similar results. The measured source strength level is shown in Figure 4.16.

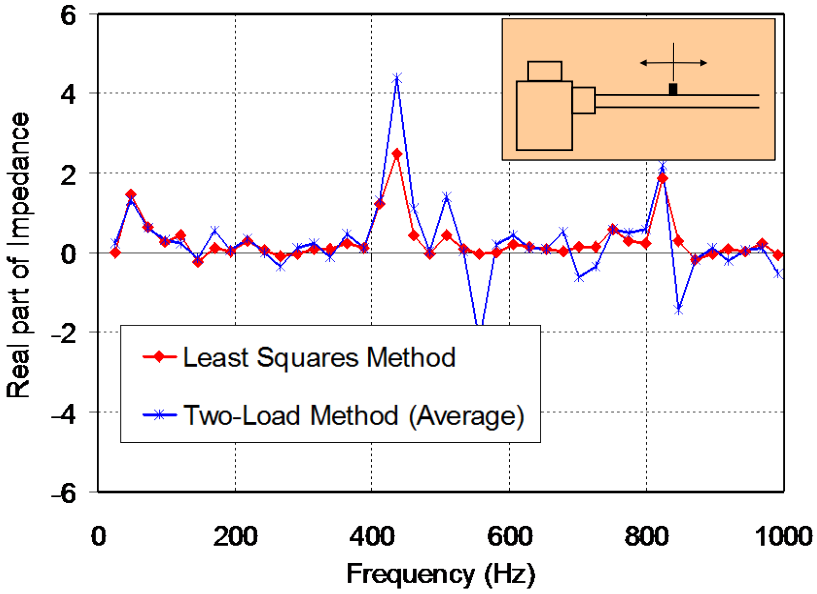

Figure 4.14 Source resistance comparison for the engine intake system.

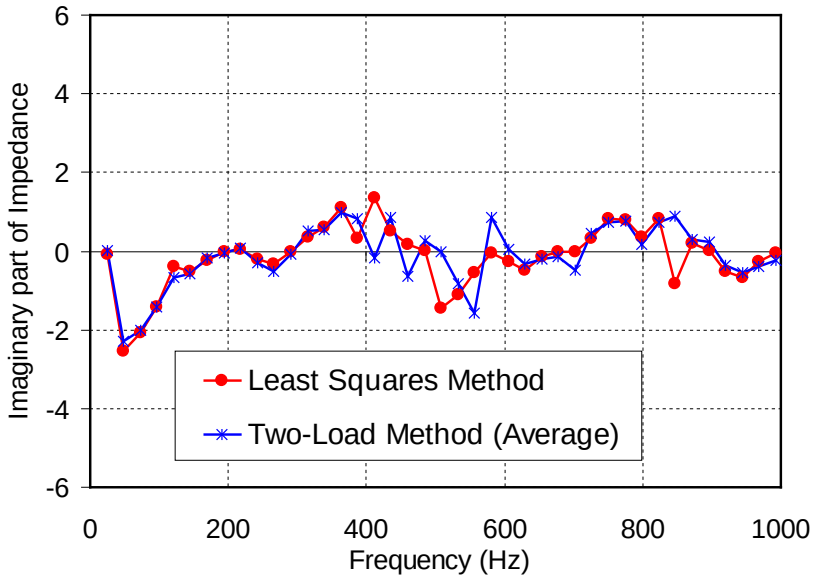

Figure 4.15 Source reactance comparison for the engine intake system.

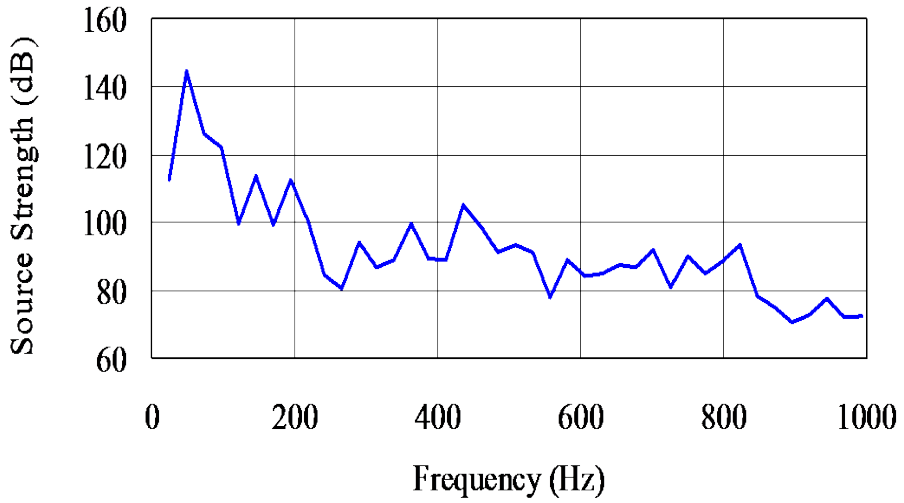

Figure 4.16 Measured source strength level of the engine intake system.

Once the source impedance and source strength are measured, the sound pressure at the termination of the pipe can be predicted using plane wave theory. This is predicated on knowing the length of the pipe and the termination impedance. In this case, the termination was an unflanged pipe opening. Figure 4.17 show the comparison between measured and predicted sound pressure level outside the 6" pipe.

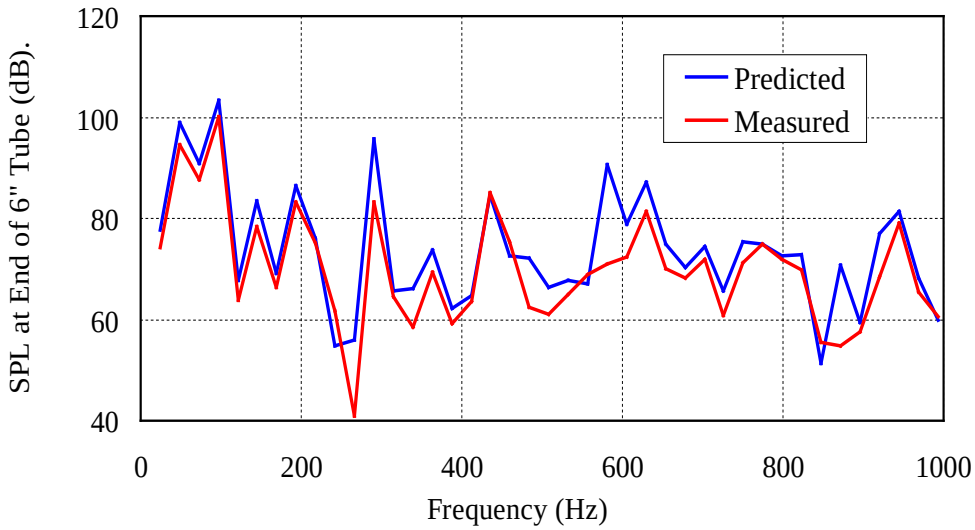

Figure 4.17 Measured and predicted sound pressure level outside of the pipe.

4.3 Incident Wave Decomposition Method

4.3.1 Background of Wave Decomposition

As discussed in Chapter 2, the solution to Helmholtz Equation consists of a positive- traveling or incident wave, and a negative-traveling or reflected wave. This can be expressed as

$$p(x) = Ae^{-jkx} + Be^{jkx} \quad . \tag{4.3.1}$$

where A and B are the complex amplitudes of the incident and reflected waves, respectively. Total pressure at a point is simply the linear superposition of the incident and reflected waves (Fahy, 2001). Based on Equation 4.3.1, the complex amplitudes, A and B, can be determined if there are two measured complex pressures. This requires two transfer function measurements between sound pressures inside the tube and a reference signal. Several duct acoustic measurement techniques has been developed based on wave decomposition.

For instance, two wave decomposition approaches have been used to measure the reflection coefficient in a tube. The reflection coefficient can be used to determine the impedance at a point in the tube or the sound absorption. The standing-wave-ratio (SWR) method, the earliest approach, calculates the ratio of the reflected to incident complex wave amplitudes by determining the positions of the maximum and minimum sound pressures in a tube. On the other hand, the two-microphone method (illustrated in Figure 4.18) utilizes the measured transfer function between two positions in the tube (Seybert, 1977). The measured transfer function (H_{12}) can be related to the reflection coefficient (R) using

$$H_{12} = \frac{P(x_2)}{P(x_1)} = \frac{Ae^{-jkx_2} + Be^{jkx_2}}{Ae^{-jkx_1} + Be^{jkx_1}} = \frac{e^{-jkx_2} + Re^{jkx_2}}{e^{-jkx_1} + Re^{jkx_1}} \quad . \tag{4.3.2}$$

Material properties such as the acoustic impedance and sound absorption coefficient can be derived from the reflection coefficient.

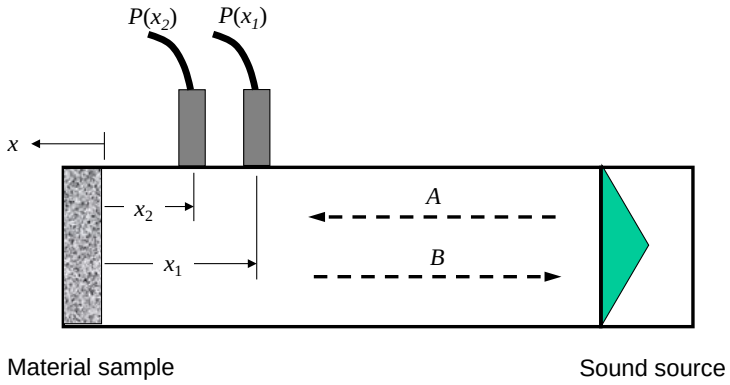

Figure 4.18 Schematic of the experimental setup for two-microphone method

Recently, Bonfiglio (2008) used similar wave decomposition approaches to develop a single-load approach to measure the normal incidence transmission loss. The schematic of the experimental setup is shown in Figure 4.19. In order to derive the transmitted wave C*, the travelling wave B in the upstream and the travelling wave C in the downstream are decomposed.

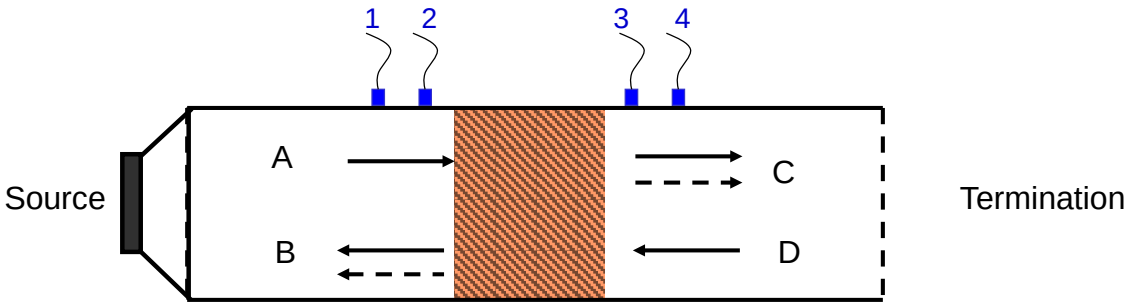

Figure 4.19 Schematic of the experimental setup for single load TL measurement.

The negative-travling wave B in the upstream can be decomposed into: the reflected wave from the surface of sample (A*R) and the transmitted contribution from the end termination (D*T). This is expressed equationally as

$$B = A \cdot R + D \cdot e^{jkd} \cdot T_{eff} \tag{4.3.3}$$

where d is the thickness of the sample, T_{eff} is the transmission coefficient of the sample, and R is the reflection coefficient. A similar analysis can be considered on the right hand side of the specimen. The downstream positive-traveling wave having complex amplitude C is the summation of the transmitted contribution of the positive-traveling wave through the specimen ($A*T$) and the reflected contribution of the negative traveling wave ($D*R$). This can be expressed as

$$C = A \cdot e^{-jkd} \cdot T_{eff} + D \cdot R \tag{4.3.4}$$

Bonfiglio assumed that the reflection coefficient was the same on each side. If that is the case, the transmission coefficient can be solved using the complex amplitudes obtained by wave-decomposition. In this thesis, the approach developed by Bonfiglio is modified and applied to measuring the source strength and source impedance.

4.3.2 Theoretical Development

Instead of using the equivalent circuit analogy, the source impedance can be obtained using wave decomposition. Boden and Abom (1995) related this wave decomposition concept in a manner similar to the following discussion. However, they did not apply the concept to the measurement of source impedance via the 2-load method. As illustrated in Figure 4.20, the major premise is that the incident sound wave (A) consists of two parts.

a. The outgoing wave from the source (P_{s+}).
b. The reflected wave from the source boundary ($B\overline{R_s}$).

Thus, A can be expressed as

$$A = P_{s+} + B \cdot R_s \tag{4.3.5}$$

The incident wave A and the reflected wave B can be obtained from the measured sound pressure at two locations (P_1, P_2) via wave decomposition (Seybert, 1977).

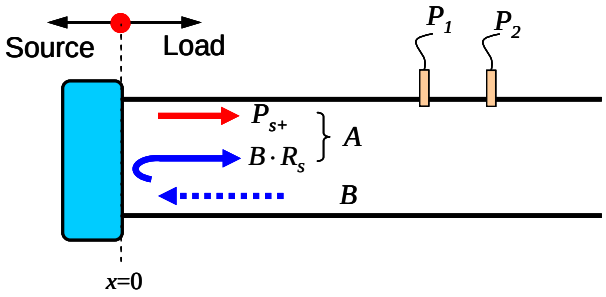

Figure 4.20 Schematic illustrating the wave decomposition premise.

By applying two different acoustic loads and measuring the sound pressures (P_1, P_2), two different sets of A's and B's are determined. Then, the two unknowns P_{s+} and R_s can be solved using

$$R_s = \frac{A_1 - A_2}{B_1 - B_2} \tag{4.3.6}$$

and

$$P_{s+} = \frac{B_1 A_2 - B_2 A_1}{B_1 - B_2} \quad . \tag{4.3.7}$$

If multiple loads are applied, then a least squares algorithm can be utilized to achieve smoother and more accurate results. The source impedance can be obtained from the reflection coefficient R_s and expressed as

$$Z_s = \frac{1 + R_s}{1 - R_s} = \frac{(B_1 - B_2) + (A_1 - A_2)}{(B_1 - B_2) - (A_1 - A_2)} \, . \tag{4.3.8}$$

With source impedance and reflection coefficient known, the source absorption coefficient can be calculated using

$$\alpha_s = 1 - \left| R_s \right|^2 \tag{4.3.9}$$

4.3.3 Relation to Two-load Method

If the equivalent circuit analogy is compared to the wave decomposition approach, a relationship between P_{s+} and P_s can be developed. Figure 4.21 places the equivalent circuit analogy side by side with the wave decomposition

approach. Notice that the load pressure (p_L) and load impedance can be expressed in terms of the incident and reflected waves as

$$p_L = A + B \tag{4.3.10}$$

and

$$Z_L = \frac{p_L}{u_0} = \frac{B + A}{B - A} \tag{4.3.11}$$

respectively. Substituting Equations 4.3.8, 4.3.10 and 4.3.11 into Equation 4.1.3 yields:

$$\frac{p_s}{\left(\frac{1 + R_s}{1 - R_s} + \frac{B + A}{B - A}\right)} = \frac{B + A}{\left(\frac{B + A}{B - A}\right)} \tag{4.3.12}$$

which can be simplified to

$$A = P_s \cdot \left(\frac{1 - R_s}{2}\right) + B \cdot R_s \ . \tag{4.3.13}$$

Comparing equation 4.3.13 to equation 4.3.5, it is evident that the source reflection coefficient (R_s) obtained by the 2-load and wave decomposition approach are identical. However, the source impedance will differ between the two approaches because of dissimilar data processing approaches. The 2-load method requires the load impedances to be known and a load pressure for each condition. In contrast, the wave decomposition approach does not require the load impedance to be known, but instead requires two sound pressures to be measured for each acoustic load.

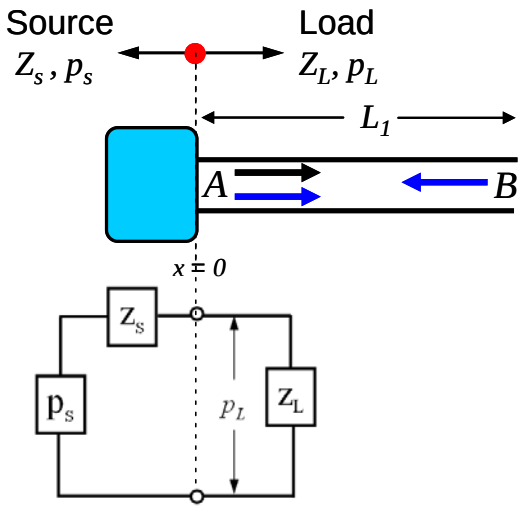

Figure 4.21 Schematic comparing wave decomposition and circuit analogy.

As noted earlier, the outgoing source strength (P_{s+}) is determined using the wave decomposition approach. This can be related to the source strength (P_s) via

$$P_{s+} = P_s \cdot \left(\frac{1 - R_s}{2} \right). \tag{4.3.14}$$

Note that P_{s+} is outgoing source strength and it can be physically defined as the sound pressure P_L (or outgoing wave A) at the source-load separation position when there is no reflection B (i.e., with an anechoic termination), as illustrated by Figure 4.22.

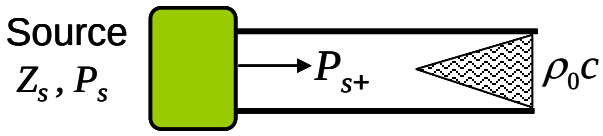

Figure 4.22 Schematic comparing source strength and outgoing source strength.

As shown in Figure 4.2, the source can be represented by a spring-mass-damper system driven by the source pressure on the left side. On the right side, the mass acts like a piston, which drives the acoustic system. By replacing the acoustic part by a unit damper, as shown in Figure 4.23, the outgoing source strength can be related to source strength by

$$P_{s+} = \frac{P_s}{1+z_s} \tag{4.3.15}$$

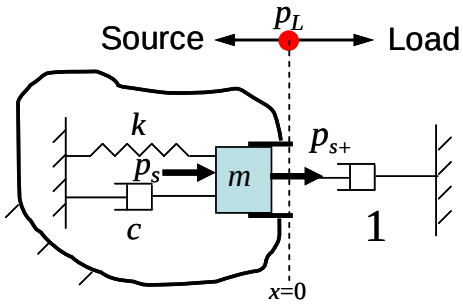

Figure 4.23 Mechanical analogy of source strength and outgoing source strength.

4.3.4 Experimental Validation

A simple experiment was conducted to investigate the utility of the wave decomposition method. The source impedance of a loudspeaker was measured using the direct, 2-load, and wave decomposition methods. The loudspeaker is rated for use above 500 Hz. Thus, the low frequency cut-off is 500 Hz. For both the two-load and wave decomposition approaches, three different loads were employed (open end, closed end, and closed end with absorbing material). Then a least squares algorithm was used to smooth the result. Figure 4.24 shows a photograph of the measurement setup.

Figure 4.24 photograph showing measurement setup

Figures 4.25 and 4.26 compare respectively the real and imaginary parts of the source impedance. Notice the excellent agreement between the approaches. However, it is notable that results obtained by the wave decomposition method exhibit less noise. Figure 4.27 compares the outgoing source strength between

two-load and wave decomposition methods. Similarly, the source strength acquired using wave decomposition method has less noise. Figure 4.28 shows the source absorption coefficient of the loudspeaker.

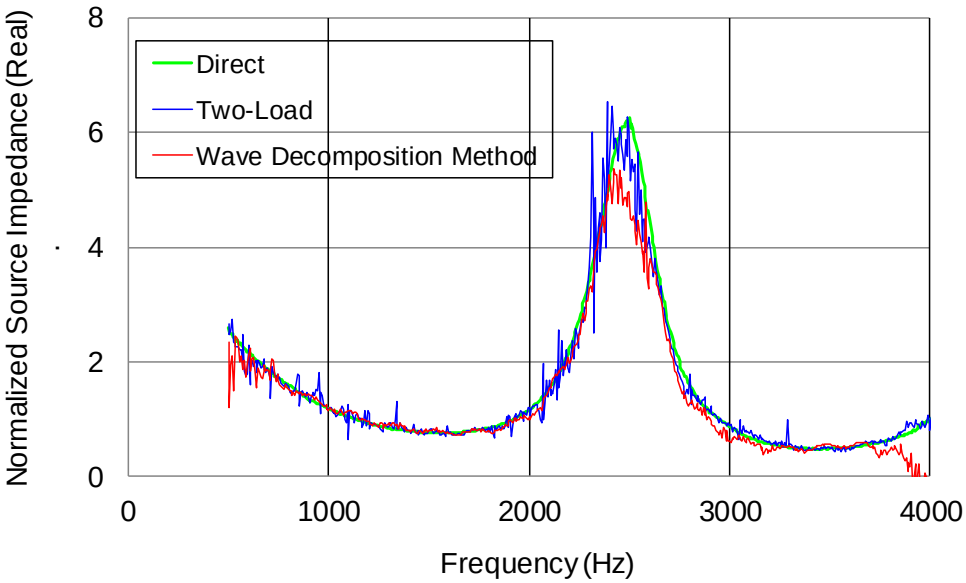

Figure 4.25 Source resistance comparison

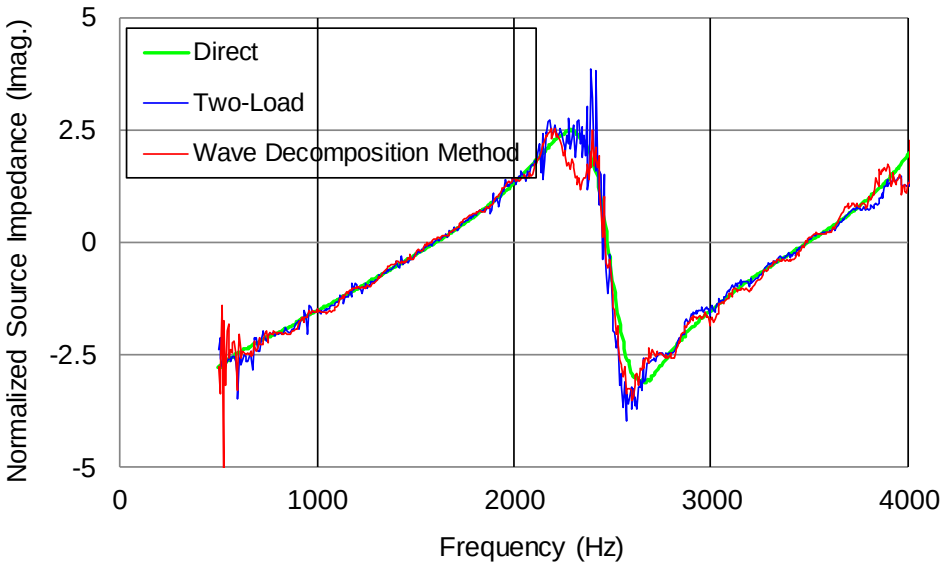

Figure 4.26 Source reactance comparison

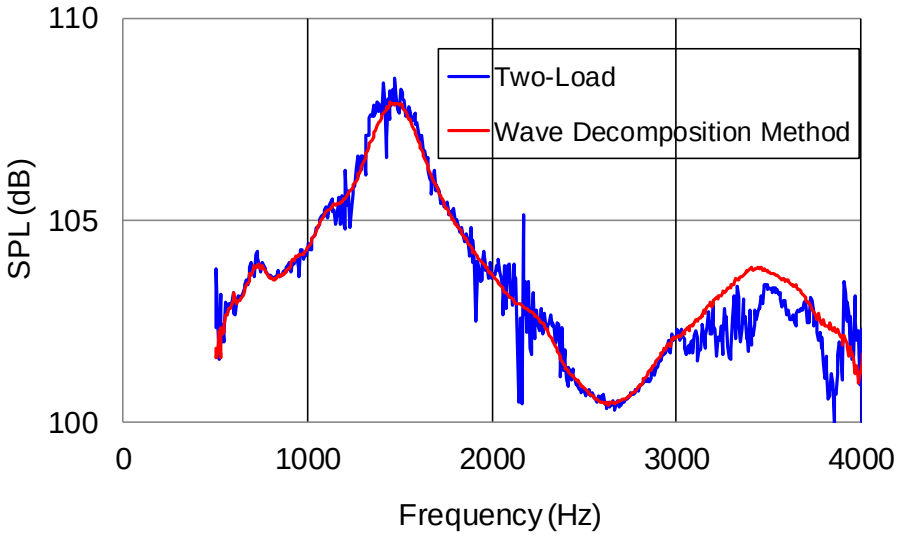

Figure 4.27 Outgoing Source Strengths comparison

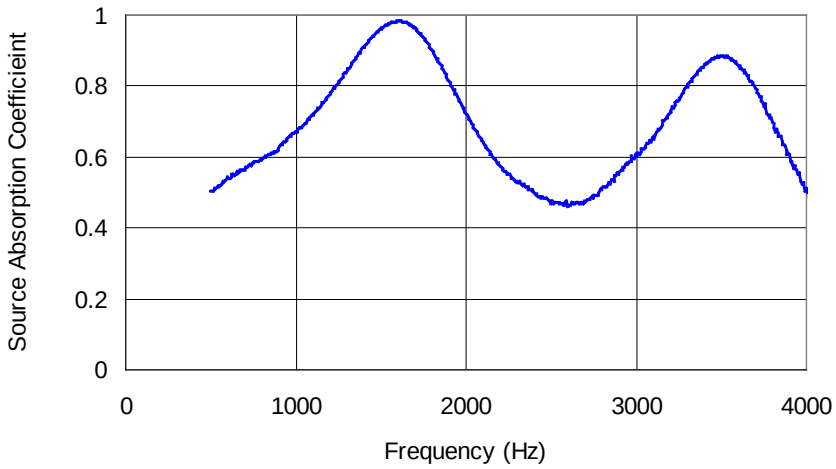

Figure 4.28 Source absorption coefficient

4.4 Study of Load Effect and Error Analysis of Measurement

4.4.1 Study of Load Effect

For a direct measurement (Ross, 1983), the source to be measured must be excited by a more powerful external source downstream. Consequently, direct measurement of the source impedance of an engine is problematic at low

frequencies because the source sound pressure is higher than the acoustic signal generated by most off-the-shelf external sources (Lavrentjev, 1992). This is the predominant source of error when using a direct measurement approach.

In contrast, indirect measurements are prone to errors which are commonly manifested as a negative resistance (Ih and Peat, 2002). Researchers have suggested that these problems are caused by the presumed linear and time-invariant model (Lavretjev, 1992) and have recommended the linearity coefficient as a "source coherence" index to check model validity (Lavretjev, 1992, Boden, 2007). Others have suggested that the error is introduced by the load combinations being too similar at some frequencies (Ih and Peat, 2002). In the discussion that follows, this second source of error is investigated.

A significant difference between the incident wave decomposition and two-load methods is that the former does not require the load impedance to be known. Thus, there is no error introduced by measuring or calculating the load impedance. However, different load impedances impact the magnitude and phase of the incident and reflected waves which in turn influence the calculation of source strength and impedance.

In order to investigate the choice of load, a constant source impedance (z_s) and outgoing source strength (p_{s+}) of $\sqrt{2}/2(1-i)$ and $5(1+i)$, respectively were selected. The termination impedance (z_{tr}) was assumed to be that of an unflanged opening. By varying the tube lengths L_1 and L_2, the incident wave A and reflected wave B can be calculated from z_s, p_{s+} and z_{tr}. By writing the wave decomposition equation for two different tube lengths, two simultaneous equations can be expressed in matrix form as

$$\begin{bmatrix} B_1 & 1 \\ B_2 & 1 \end{bmatrix} \begin{Bmatrix} R_s \\ p_{s+} \end{Bmatrix} = \begin{Bmatrix} A_1 \\ A_2 \end{Bmatrix} . \tag{4.4.1}$$

As introduced in perturbation theory (Demmel, 1997), the condition number of matrix D for an equation of the form $[D]\{x\} = \{y\}$ can be expressed as

$$\kappa(D) = \|D\|^{-1} \cdot \|D\| \ . \tag{4.4.2}$$

The condition number can be used to relate measurement errors in A and B to the error in source impedance. Figure 4.29 shows a contour plot of the reciprocal of the condition number $(1/\kappa(D))$ as a function of the lengths L_1 and L_2.

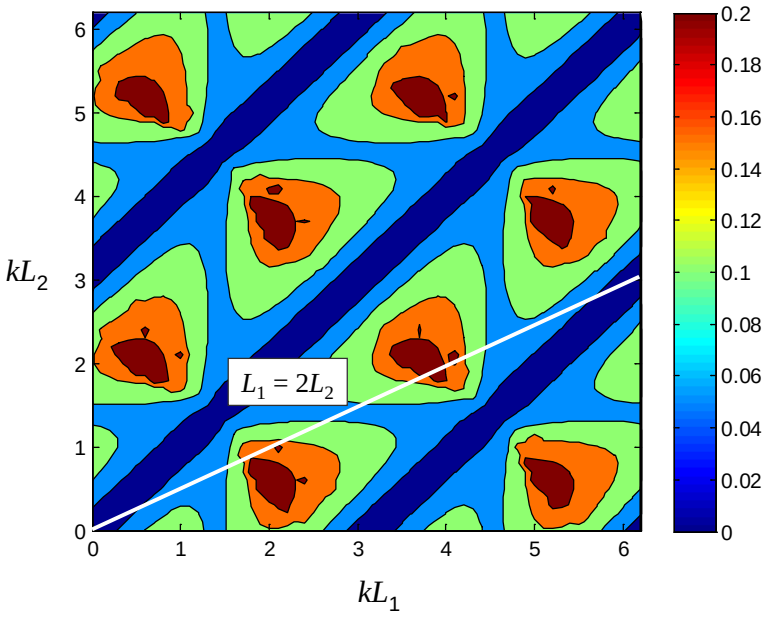

Figure 4.29 Reciprocal of Condition Number $(1/\kappa(D))$ for Equation (4.4.1) as a function of kL_1 and kL_2.

Notice the ill-conditioning in the bands (Notice the dark blue diagonal bands) where

$$kL_2 = kL_1 + n\pi, \quad n = 0,1,2... \tag{4.4.3}$$

where k is the acoustic wavenumber. This implies that the load conditions are overly similar. Similarly, ill-conditioning is also evident for tube resonances which occur when

$$kL_i = \frac{2n+1}{2}\pi, \qquad i = 1,2 \;\; and \;\; n = 0,1,2... \tag{4.4.4}$$

Excluding the two bands specified by Equations 4.4.3 and 4.4.4, notice that the matrix is well-conditioned when

$$kL_2 = kL_1 + \frac{2n+1}{2}\pi, \qquad n = ...-2,-1,0,1,2... \tag{4.4.5}$$

This occurs when the load impedances are out of phase by 90 degrees (indicated in dark red).

Additionally, notice that any length combination can be represented by a line beginning at the origin. For example, the condition number for a length combination $L_2 = 2L_1$ is shown on the contour plot in Figure 4.29. Notice that traversing the line amounts to varying the frequency. Thus, most length combinations will exhibit both well- and ill- conditioning in several frequency bands. The condition number analysis aids in choosing appropriate tube lengths in order to avoid ill-conditioning in frequency bands of interest.

4.4.2 Error Analysis

The different methods to determine source impedance and source strength will not give the same results due to the different processing schemes and input data used (Boden, 1988). Seybert (1970) and Soenarko (1980) investigated the effect of error in the spectra and microphone spacing. They provided recommendations to minimize the error. Boden (1988) investigated the effect of errors in the input spectra if the two-load method is used. The sensitivity to errors was calculated using first order Taylor expansions and direct numerical simulation.

For the two-load method, the errors in measured source impedance and source strength are a result of 1) the errors in the measured sound pressures and the measured or calculated load impedances, and 2) the sensitivity of the calculation to errors in the input data. Errors in the measured load impedances can be determined using the approach suggested by Seybert (1981). Boden developed equations to determine the sensitivity of the two-load method equations to errors in the input data. If the errors in the input data are assumed to be small, then Equations 4.2.1 and 4.2.2 can be expanded as a first order Taylor series. The relative errors of the source impedance and source strength can be expressed as:

$$\frac{\Delta z_s}{z_s} = \frac{z_s + z_{L2}}{z_{L2} - z_{L1}} \frac{\Delta z_{L1}}{z_1} + \frac{z_s + z_{L1}}{z_{L1} - z_{L2}} \frac{\Delta z_{L2}}{z_2} + \frac{(z_s + z_{L2})(z_s + z_{L1})}{z_s(z_{L1} - z_{L2})} \frac{\Delta p_{L1}}{p_{L1}} + \frac{(z_s + z_{L2})(z_s + z_{L1})}{z_s(z_{L2} - z_{L1})} \frac{\Delta p_{L2}}{p_{L2}} \tag{4.4.6}$$

and

$$\frac{\Delta p_s}{p_s} = \frac{z_s}{z_{L2} - z_{L1}} \frac{\Delta z_{L1}}{z_1} + \frac{z_s}{z_{L1} - z_{L2}} \frac{\Delta z_{L2}}{z_2} + \frac{(z_s + z_{L1})}{(z_{L1} - z_{L2})} \frac{\Delta p_{L1}}{p_{L1}} + \frac{(z_s + z_{L2})}{(z_{L2} - z_{L1})} \frac{\Delta p_{L2}}{p_{L2}}. \tag{4.4.7}$$

It can be observed from the above equations that the relative errors of source impedance and source strength are small when one load impedance is on the same order as the source impedance while the other one is very different. The relative errors increase dramatically when the two load impedances are approximately equivalent. Alves (1986) suggested that the two-load method is less sensitive to errors when an absorptive and open-ended termination is used instead of using two open ended terminations.

An error analysis of the wave decomposition approach is presented in this section. In order to solve source strength and source impedance using Equation 4.3.7 and 4.3.8, the complex wave amplitudes should be calculated from the measured sound pressures at two locations. The complex amplitudes (A and B) can be expressed as

$$A = \frac{p_1 e^{jkx_2} - p_2 e^{jkx_1}}{e^{jk(x_2 - x_1)} - e^{jk(x_1 - x_2)}} \tag{4.4.8}$$

and

$$B = \frac{p_2 e^{-jkx_1} - p_1 e^{-jkx_2}}{e^{jk(x_2 - x_1)} - e^{jk(x_1 - x_2)}} \tag{4.4.9}$$

where p_1 and p_2 are measured complex pressures at the two the microphone positions, and x_1 and x_2 are distances from the microphone positions to the source-load separation point. By substituting equations 4.4.8 and 4.4.9 into

equation 4.3.8, source impedance and source strength can be expressed in terms of the four measured sound pressures as

$$z_s = \frac{(p_{1b} - p_{1a})\left(e^{-jkx_2} - e^{jkx_2}\right) + (p_{2a} - p_{2b})\left(e^{-jkx_1} - e^{jkx_1}\right)}{(p_{1a} - p_{1b})\left(e^{-jkx_2} + e^{jkx_2}\right) + (p_{2b} - p_{2a})\left(e^{-jkx_1} + e^{jkx_1}\right)} \quad (4.4.10)$$

where p_{1a}, p_{1b}, p_{2a} and p_{2b} are sound pressures at microphone positions 1 and 2, respectively. The indices a and b indicate the two different loads..

The errors in the wave decomposition method depend on the errors in the measured sound pressures and the sensitivity of the equations to errors in the input data. The approach used is similar to that used by Boden (1988). The source impedance's sensitivity to errors in each of the measured sound pressures can be expressed as:

$$\frac{\partial z_s}{\partial p_{1a}} = \frac{2 \cdot (p_{2a} - p_{2b})\left(e^{jk(x_1 - x_2)} - e^{jk(x_2 - x_1)}\right)}{\left[(p_{1a} - p_{1b})\left(e^{-jkx_2} + e^{jkx_2}\right) + (p_{2b} - p_{2a})\left(e^{-jkx_1} + e^{jkx_1}\right)\right]^2} \quad (4.4.11)$$

$$\frac{\partial z_s}{\partial p_{1b}} = \frac{2 \cdot (p_{2a} - p_{2b})\left(e^{jk(x_2 - x_1)} - e^{jk(x_1 - x_2)}\right)}{\left[(p_{1a} - p_{1b})\left(e^{-jkx_2} + e^{jkx_2}\right) + (p_{2b} - p_{2a})\left(e^{-jkx_1} + e^{jkx_1}\right)\right]^2} \quad (4.4.12)$$

$$\frac{\partial z_s}{\partial p_{2a}} = \frac{2 \cdot (p_{1a} - p_{1b})\left(e^{jk(x_2 - x_1)} - e^{jk(x_1 - x_2)}\right)}{\left[(p_{1a} - p_{1b})\left(e^{-jkx_2} + e^{jkx_2}\right) + (p_{2b} - p_{2a})\left(e^{-jkx_1} + e^{jkx_1}\right)\right]^2} \quad (4.4.13)$$

and

$$\frac{\partial z_s}{\partial p_{2b}} = \frac{2 \cdot (p_{1a} - p_{1b})\left(e^{jk(x_1 - x_2)} - e^{jk(x_2 - x_1)}\right)}{\left[(p_{1a} - p_{1b})\left(e^{-jkx_2} + e^{jkx_2}\right) + (p_{2b} - p_{2a})\left(e^{-jkx_1} + e^{jkx_1}\right)\right]^2} \quad (4.4.14)$$

Consider a case when the measured sound pressures are similar for two different loads. This results in a singularity since the denominators in Equations 4.4.11-4.4.14 approaches zero. This result is similar to Boden's error analysis of the two-load method. Additionally, the effect of errors due to the microphone locations can be analyzed. The respective sensitivity coefficients for the two microphone distances are:

$$\frac{\partial z_s}{\partial x_1} = \frac{jk\left(p_{2a}-p_{2b}\right)\left[2\left(p_{1a}-p_{1b}\right)\left(-e^{jk\left(x_1-x_2\right)}-e^{jk\left(x_2-x_1\right)}\right)+4\left(p_{2a}-p_{2b}\right)\right]}{\left[\left(p_{1a}-p_{1b}\right)\left(e^{-jkx_2}+e^{jkx_2}\right)+\left(p_{2b}-p_{2a}\right)\left(e^{-jkx_1}+e^{jkx_1}\right)\right]^2} \tag{4.4.15}$$

and

$$\frac{\partial z_s}{\partial x_1} = \frac{jk\left(p_{1a}-p_{1b}\right)\left[2\left(p_{2a}-p_{2b}\right)\left(-e^{jk\left(x_1-x_2\right)}-e^{jk\left(x_2-x_1\right)}\right)+4\left(p_{1a}-p_{1b}\right)\right]}{\left[\left(p_{1a}-p_{1b}\right)\left(e^{-jkx_2}+e^{jkx_2}\right)+\left(p_{2b}-p_{2a}\right)\left(e^{-jkx_1}+e^{jkx_1}\right)\right]^2} \tag{4.4.16}$$

The sensitivity coefficients for distances are directly proportional to the frequency via the wavenumber. This suggests that measurements at high frequencies will be prone to error. The total error for measuring source impedance can be determined based on the errors in the input data and error propagation rules as

$$\Delta z_s = \left[\left|\frac{\partial z_s}{\partial p_{1a}}\right|^2 \cdot \Delta {p_{1a}}^2 + \left|\frac{\partial z_s}{\partial p_{1b}}\right|^2 \cdot \Delta {p_{1b}}^2 + \left|\frac{\partial z_s}{\partial p_{2a}}\right|^2 \cdot \Delta {p_{2a}}^2 + \left|\frac{\partial z_s}{\partial p_{2b}}\right|^2 \cdot \Delta {p_{2b}}^2 + \left|\frac{\partial z_s}{\partial x_1}\right|^2 \cdot \Delta {x_1}^2 + \left|\frac{\partial z_s}{\partial x_2}\right|^2 \cdot \Delta {x_2}^2\right]^{1/2} \tag{4.4.17}$$

The analytical approach of error analysis is suitable for drawing general conclusions, while direct numerical simulation is the simplest way to estimate the error sensitivity for a given measurement situation. The effect of measurement error was investigated by introducing random perturbation to the incident and reflected waves A and B. This error is averaged over the frequency range. The error for a selected length combination is compared to the case in which one of the loads is anechoic. The anechoic load is expected to be very different from a tube length with flanged opening. Input errors of 0.01%, 0.1%, 1%, 10% and 100% are applied to incident and reflected waves A and B since they are the only sources of measurement error. As shown in Figure 4.30, utilizing an anechoic load should reduce the effects of measurement errors.

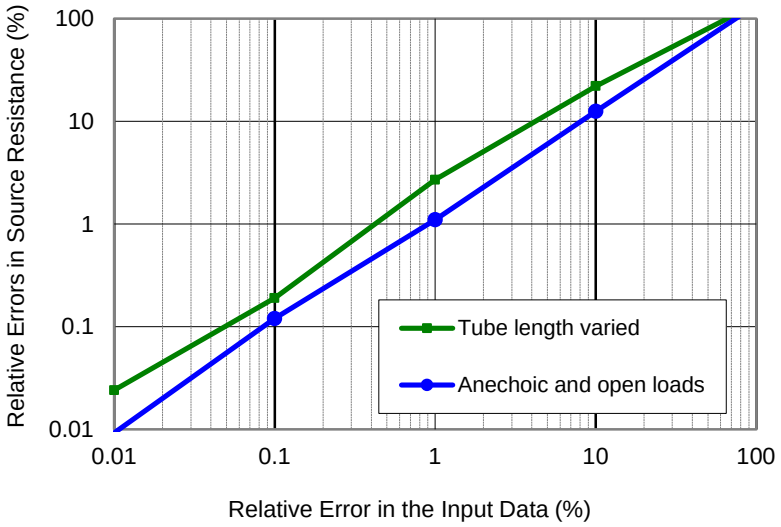

Figure 4.30 Comparison of relative error for different acoustic loads.

4.4.3 Negative Source Resistance

The measured source resistance of an internal combustion engine is frequently found to be negative. For example, the source resistance of the internal combustion engine intake shown earlier (Figure 4.31) was negative at some frequencies. Negative source resistance is related to negative source absorption coefficient, which suggests that more energy is reflected than is incident. It follows that negative source resistance is physically impossible. In most cases, proper measurement of source impedance by the direct method will yield a positive resistance. Negative source impedance normally occurs in the case of indirect measurements (Ih, 2002).

A positive source resistance implies a positive absorption coefficient or a source reflection coefficient having an absolute value smaller than 1. According to Equation 4.3.6, the reflection coefficient can be replaced by incident and reflected waves. The source resistance will be positive when

$$\left|A_1 - A_2\right| \leq \left|B_1 - B_2\right| \tag{4.4.18}$$

This criterion suggests that changing the load should affect the reflected wave more than the incident wave. For example, Figure 4.32 shows the incident and

reflected wave amplitudes for a loudspeaker source impedance measurement. Clearly, the difference between the two reflected waves is much greater than that of the two incident waves. This insures that the measured source resistance will be positive as shown in Figure 4.26.

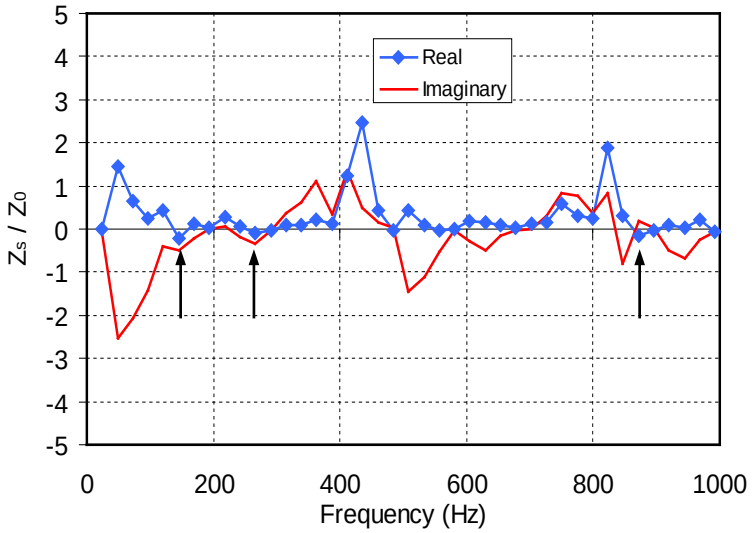

Figure 4.31 Source impedance of an internal combustion engine intake.

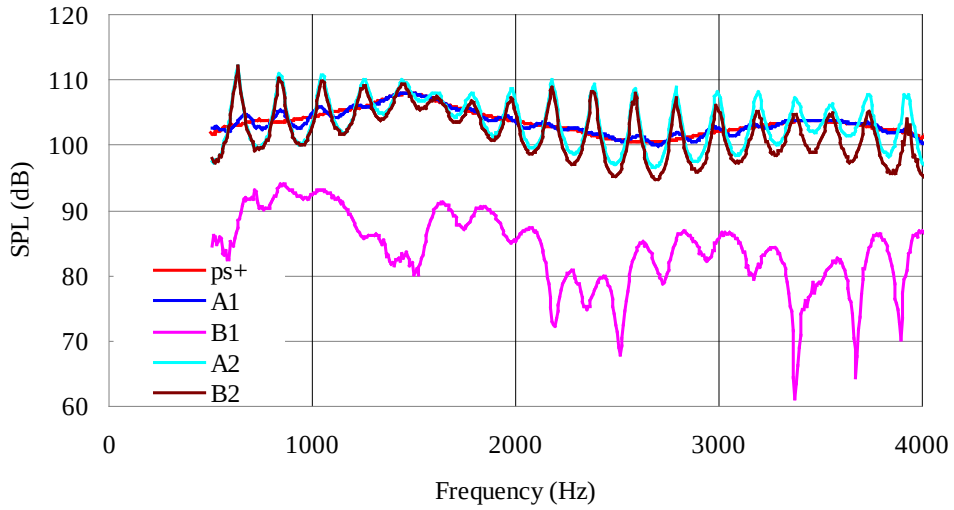

Figure 4.32 Comparison between incident and reflected waves for two loads.

4.5 Applying the Measured Source Impedance to Insertion Loss Prediction

Insertion loss is defined as the change in the radiated sound pressure resulting from the insertion of the attenuation element. Insertion loss is generally more useful to noise control engineers since it evaluates how well an attenuation device will perform in the actual system. It provides an insight into the coupling between the source, termination, and the attenuating elements.

Based on its definition, the measurement of insertion loss is straightforward. It requires a sound pressure level measurement at a given position for the system with and without the attenuating element. It is common to use a straight duct have the same length as the system with attenuation element as a reference (the "without attenuation element" case). The measurement approach is illustrated in Figure 4.33. The insertion loss of a muffler equals the difference between the two sound pressure levels (SPL_1 and SPL_2) in dB.

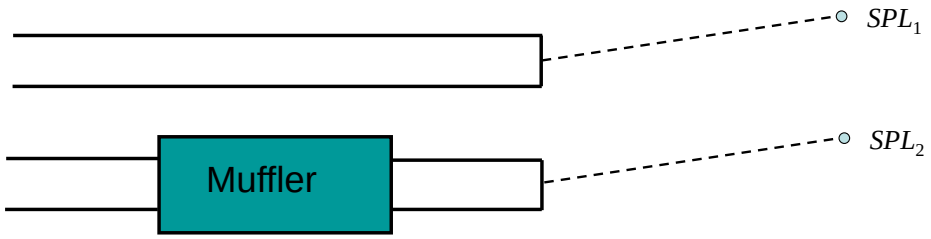

Figure 4.33 Schematic of insertion loss measurement.

During the design stage, it is desirable to predict the performance of the attenuation element before the prototype is made. However, this is difficult because the source impedance is often unknown.

To show explicitly the importance of source impedance, insertion loss of an simple expansion chamber was predicted for various assumed source impedances and then compared with that predicted for a measured source impedance. The various values assumed for source impedance are zero, anechoic and infinity. The source impedance for the engine intake shown in Figures 4.14 and 4.15 is used as the measured data. Figure 4.34 shows a schematic of the simple exhaust system that was considered. Predictions of the

insertion loss are shown in Figure 4.35 for different source impedances. It is notable that the source impedance has a large impact on the insertion loss. Additionally, the insertion loss can sometimes be negative due to resonances in the pipe.

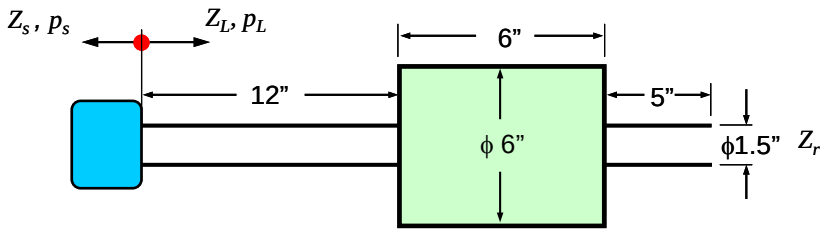

Figure 4.34 Schematic showing example exhaust system.

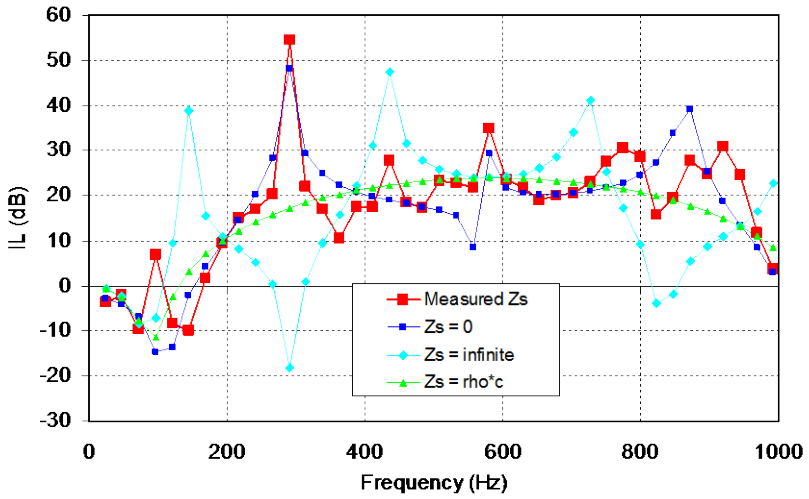

Figure 4.35 Insertion loss comparisons as a function of source impedance.

A small engine muffler was used to demonstrate the prediction of insertion loss from measured data. A loudspeaker and an unflanged open pipe were used as the source and termination conditions. The transfer matrix for the muffler was measured using the two-source method, and Figure 4.36 shows the setup for the two-source method. The measured four-pole parameters are shown in Figure 4.37. Real parts are shown in blue, and imaginary parts are shown in green. The transfer matrix for a reference duct having the same length was determined theoretically using Equation 2.1.35.

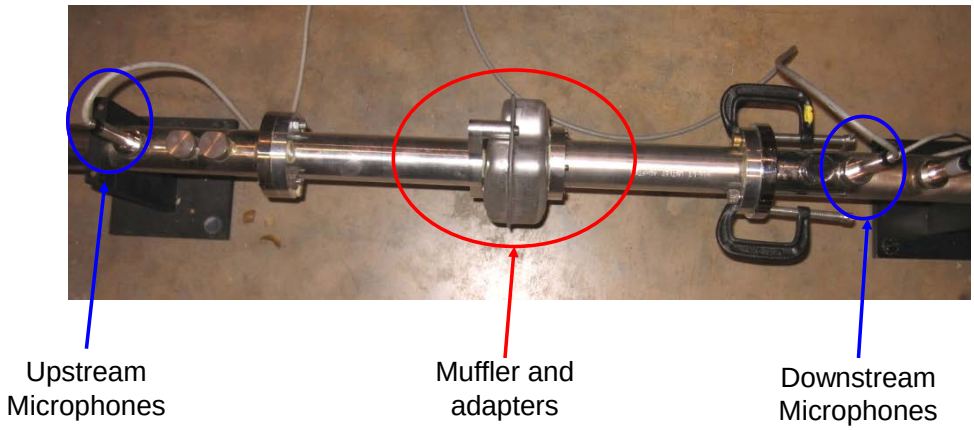

Figure 4.36 Muffler in transfer matrix measurement setup.

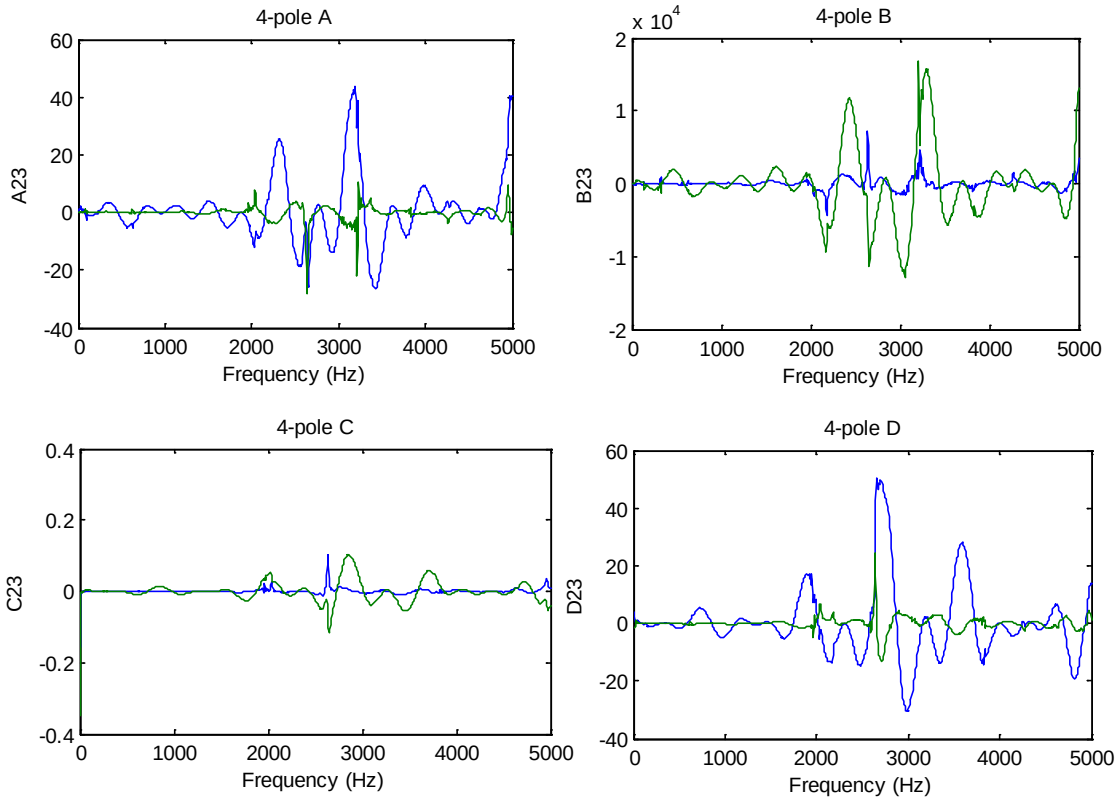

Figure 4.37 Measured four pole parameters of the muffler.

The source impedance for the loudspeaker was measured using the wave decomposition approach, as shown in Figure 4.38. The impedance is normalized by the characteristic impedance ($\rho_0 c$) in the figure. The termination impedance of the unflanged open duct was measured using the two-microphone method as shown in Figure 4.39.

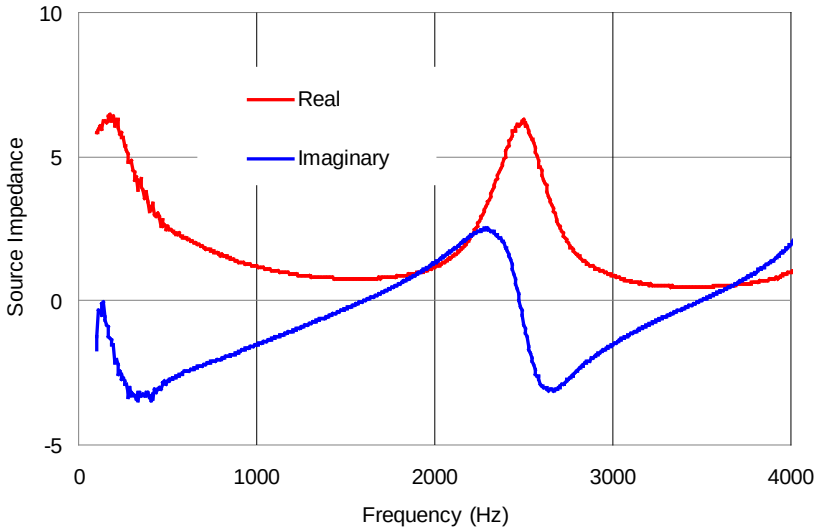

Figure 4.38 Measured source impedance of the loudspeaker.

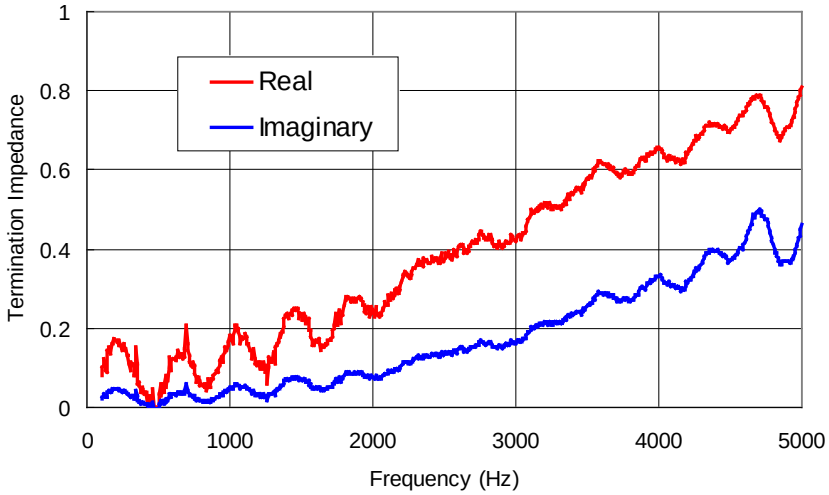

Figure 4.39 Measured termination impedance of the unflanged open pipe.

Using the measured source and termination impedances, and the measured transfer matrix for the muffler; the insertion loss was predicted using Equation 4.1.1. Figure 4.40 compares the measured to the predicted insertion loss. The results compare well and demonstrate how insertion loss can be predicted accurately if the source and termination impedances are known in advance.

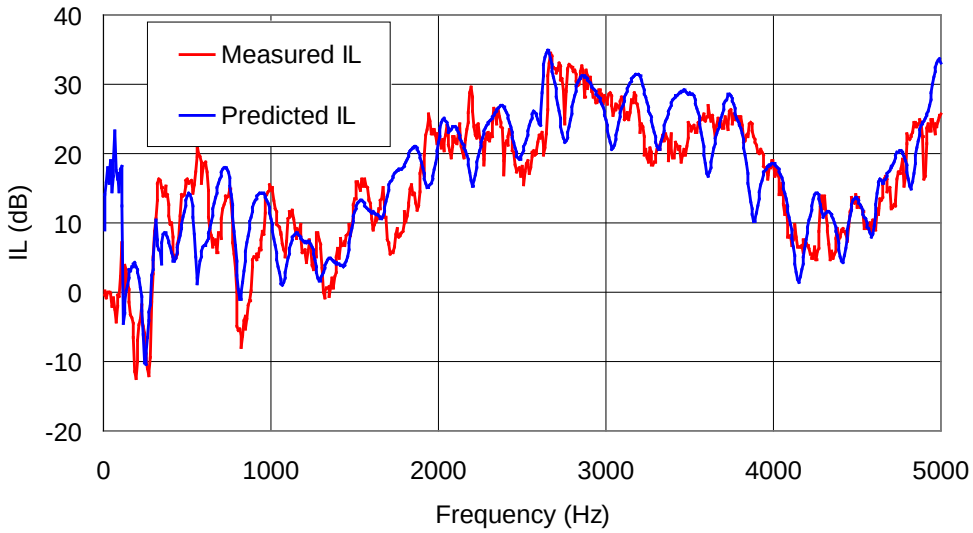

Figure 4.40 Insertion loss comparison.

4.6 Summary

The source impedance of an engine intake system was determined using both the two-load and least squares methods. The load was varied by using different lengths of pipe affixed to the intake. The results were similar for both techniques particularly when the source impedance results from the two-load method were averaged.

A wave decomposition method has been developed and compared with the existing 2-load approach. It has been demonstrated that this simplified method uses the reflection of the primary source energy as an external source. In that sense, it is similar to the direct method. The primary source itself can be used as the reference signal. This may be advantageous since the source itself can be used to obtain the desired data without the necessity of adding a 20 dB higher external source (typically required for the direct method). This similarity to the direct method may also explain why the simplified 2-load method produces smoother results than the existing 2-load approach.

The error analysis shows that selecting different tube lengths to modify acoustic load has little effect on the frequency wide source impedance accuracy.

However, tube lengths could be strategically selected so as to enhance measurement accuracy in particular frequency bands. Changing the termination configuration can improve measurement accuracy if the two terminations produce very different acoustic loads. If possible, near anechoic and open-flange load combinations should improve measurement accuracy reducing the possibility of negative source resistance.

The importance of source impedance was demonstrated by examining the impact of varying the source impedance on the insertion loss for a simple exhaust system. Measured source impedance was used to predict the insertion loss of a small muffler with good agreement with measured data.

CHAPTER 5
TRANSFER IMPEDANCE AND MICRO-PERFORATED PANELS

5.1 Transfer Impedance Measurement for Micro-perforated Panel

Micro-perforated panel (MPP) absorbers can be modeled using a series impedance or transfer impedance. It is assumed that the volume velocity will be the same on both sides of the panel. The simplest method to measure the transfer impedance is the impedance subtraction method developed by Wu et al. (2003). The measurement setup is shown below in Figure 5.1. The impedance is measured with and without the perforated panel placed in the tube.

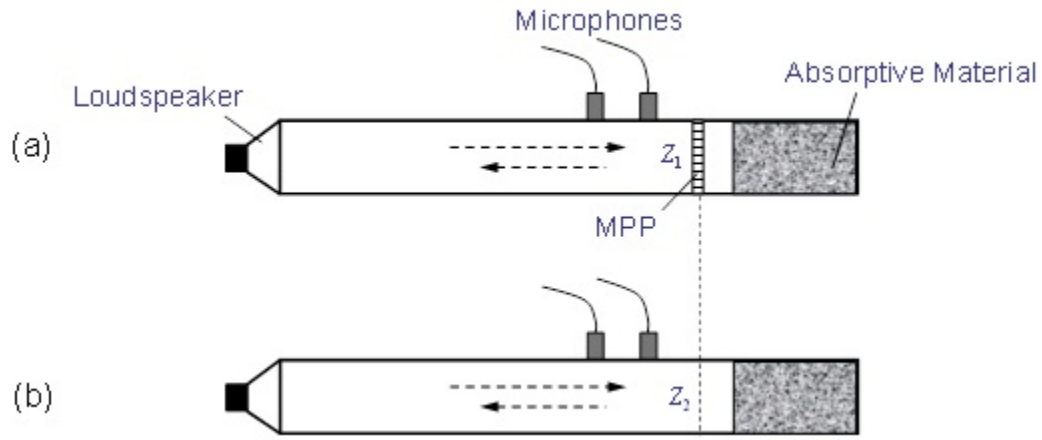

Figure 5.1 Experiment setup for impedance subtraction method. (a) with MPP, (b) without MPP.

The transfer impedance is the difference between the impedances in front and back of the panel. The impedance in front of the panel (Z_1) is that of the combined panel and backing cavity while the impedance behind the panel (Z_2) is that of the backing cavity alone. Both impedances can be measured using the two-microphone method (Seybert, 1977). Absorptive material is often added to the end of the tube in order to reduce the sound reflection from the termination. The transfer impedance can be expressed as

$$z_{tr} = \frac{p_1 - p_2}{u} = Z_1 - Z_2 \tag{5.1.1}$$

where p_1 and p_2 are the sound pressures in front and back of the panel, and u is the particle velocity which is assumed to be the same on both sides of the panel. Z_1 and Z_2 are the impedances with and without the MPP. Alternatively, the transfer impedance can be calculated from reflection coefficient using Equations 2.3.3 and 2.3.4 after the transfer matrix is measured using either the two-load or two-source method (Yoo, 2008).

In this section, an explicit equation is developed for the transfer impedance of micro-perforated panels based on impedance tube measurements with four microphones. In this case, the transfer matrix is not measured. The measurement setup, which is identical to the two-load method, is shown in Figure 5.2.

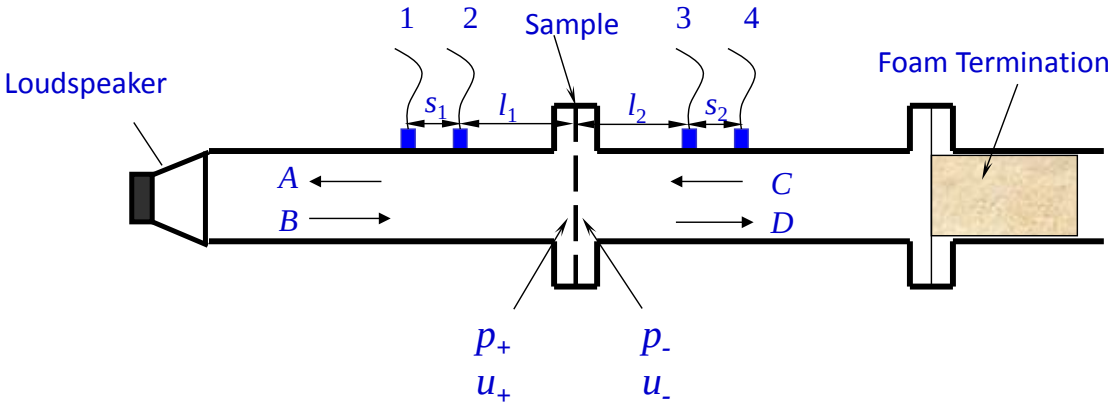

Figure 5.2 Setup for four microphone transfer impedance measurement.

Wave decomposition pairs in front and back of the MPP can be expressed as

$$A = \frac{p_1 e^{-jkl_1} - p_2 e^{-jk(l_1+s_1)}}{2j\sin(ks_1)} \qquad B = \frac{p_2 e^{jk(l_1+s_1)} - p_1 e^{jkl_1}}{2j\sin(ks_1)}$$
$$C = \frac{p_3 e^{jk(l_2+s_2)} - p_4 e^{jkl_2}}{2j\sin(ks_2)} \qquad D = \frac{p_4 e^{-jkl_2} - p_3 e^{-jk(l_2+s_2)}}{2j\sin(ks_2)} \tag{5.1.2}$$

where l_1 is the distance between microphone 2 and the sample, l_2 is distance between the microphone 3 and the sample, s_1 is the distance between microphones 1 and 2, s_2 is the distance between microphones 3 and 4 (ASTM,

2009). Based on wave decomposition approaches, the sound pressures and particle velocities can be calculated as:

$$\begin{aligned} p_+ &= A + B & u_+ &= (A - B)/\rho_0 c \\ p_- &= C + D & u_- &= (C - D)/\rho_0 c \quad . \end{aligned} \tag{5.1.3}$$

The transfer impedance can be calculated by taking the ratio of the difference between the sound pressures on both sides of the panel, and the particle velocity. The particle velocity on each side of the panel should theoretically be equal according to the transfer impedance assumption. In practice, there will be differences between the particle velocities and they should be averaged in order to calculate the transfer impedance. Thus, the transfer impedance can be expressed as

$$z_{tr} = \frac{p_+ - p_-}{(u_+ + u_-)/2} = \rho_0 c \cdot \frac{A + B - C - D}{(A - B + C - D)/2} \quad . \tag{5.1.4}$$

Though the transfer impedance can be measured using a number of different approaches, the impedance subtraction method was selected for this dissertation.

5.2 Effective Geometric Parameters Estimation

Cutting circular-shaped perfortions is normally accomplished by using either a laser or a drill press (Yoo, 2008). As a result, high manufacturing costs preclude their use in most products. However, lower cost MPP absorbers with slit-shaped perforations are being produced that perform similar. Figure 5.3 shows a magnified view and an illustrated cross-section view of a single slit. Notice that the slit shape is complicated, slit dimensions vary with thickness, and the slit is angled through the metal. Consequently, geometric parameters, namely slit size and porosity, are difficult to measure, and difficult to relate to Maa's equation directly.

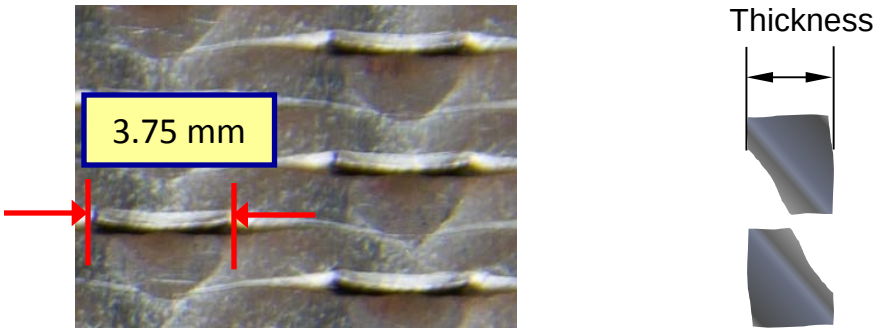

Figure 5.3 Magnified view and illustrated cross-section view of a single slit.

Efforts have been made to measure these geometric parameters. For example, the porosity has been estimated by measuring the light intensity through the panel. Slit size has been calculated by averaging the measured widths of many holes at different depths. However, substituting these approximate geometric parameters into either Equation 3.2.2 or Equation 3.2.7 yields transfer impedances that do not correlate well with measured results. As a result, the absorption coefficient and transmission loss cannot be predicted and used in models using estimated geometric parameter.

In order to provide these necessary geometric parameters for noise control engineers during the design and simulation stage, an effective parameter estimation method for MPP absorbers having slit-shaped perforations is proposed. The slit parameters are calculated backward using measured absorption data and a nonlinear least square data fitting algorithm. The estimated parameters can be directly used in the commonly adopted Maa's equation. The feasibility of this approach is considered in the section that follows.

5.2.1 Feasibility of Data Fitting

When the MPP absorber thickness and cavity depth are known, two geometric parameters, hole size and panel porosity, determine the acoustic performance. In order to study the feasibility and uniqueness of an inverse calculation, the effect of these two parameters on absorption is investigated. For a single layer MPP absorber, a parametric study was reported in Chapter 3. Detailed results were

shown in Chapter 3. Figures 3.17 and 3.18 are revisited in this section. Figure 3.17 shows the effect of varying the hole diameter with the other design parameters held constant. Notice that the hole diameter controls the band width and peak value of the absorption. However, hole diameter has no effect on the center frequency of the absorption band. Figure 3.18 shows that the panel porosity affects both the center frequency and the peak value of the absorption. Increasing porosity moves the central frequency of the absorption band higher in frequency. It can be observed that a unique combination of hole diameter and panel porosity will produce an absorption curve that has a unique combination of peak absorption value, band width, and center frequency. Figure 5.4 shows different porosity and hole diameter combinations that produce the resulting absorption coefficients at a single frequency (1000 Hz). Notice that for a given absorption, there are numerous candidate porosity and hole diameter combinations.

However, the absorption curve is frequency dependent. Accordingly, there will be multiple porosity and hole diameter combinations at each frequency. For example, the measured absorption coefficient of a micro-perforated panel is 0.44 at 850 Hz, and the porosity and hole diameter combinations that produce sound absorption coefficients within 1% error are shown as a strip of red circles. The absorption coefficient is 0.52 at 3250 Hz, and the porosity and hole diameter combinations that can produce a sound absorption coefficient within 1% error are shown as a strip of blue circles. Notice that the overlap region is very small for only two absorption coefficient values, and the exact solution is shown as a black dot. When there are 800 absorption coefficient values to fit, the overlap region can be narrowed down into a small region within the error criteria.

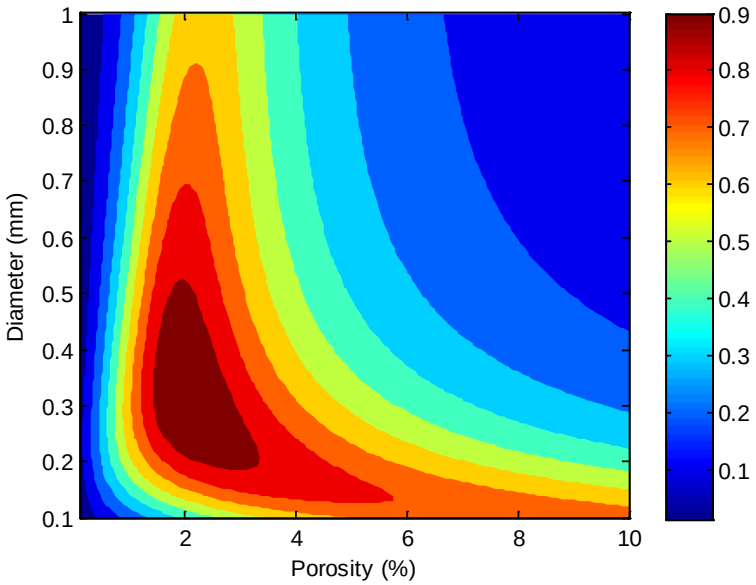

Figure 5.4 Absorption coefficient dependency on porosity and hole diameter.

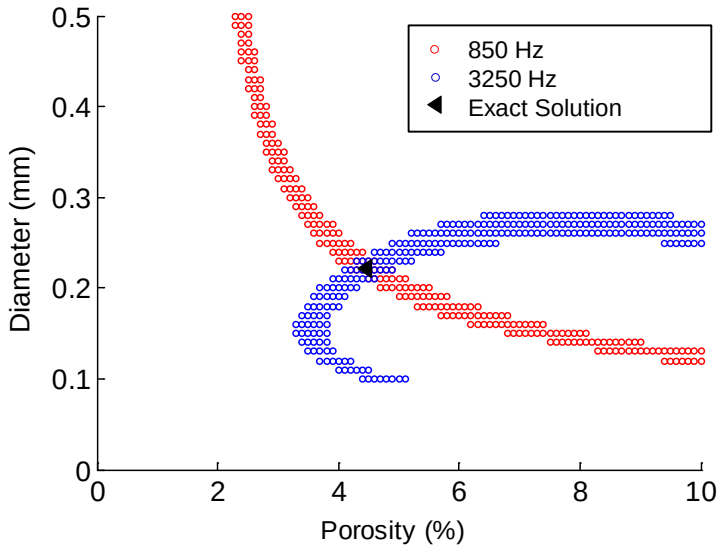

Figure 5.5 Overlap of candidates of porosity and hole diameter combination.

5.2.2 Nonlinear Least Square Data Fitting Algorithm

In order to calculate perforation diameter and panel porosity based on the measured absorption coefficient, two assumptions are made. First of all, the acoustic performance of an irregular-shaped slit can be represented by a circular or rectangular shaped hole with effective geometric parameters. That is, either Equation 3.2.2 or Equation 3.2.7 can be used to represent the transfer

impedance of an MPP with slit-shaped perforations. Of cause, the estimated geometric parameters will be different when different models are used. Second, measurement error of normal incidence absorption coefficient can be ignored. Thus, it is desirable to have small error in the measured sound absorption over the frequency range used for the curve fit. That being the case, measured data below 100 Hz and above 4000 Hz was discarded (measured using the 1.375 inch diameter tube).

The objective is to determine a combination of porosity and hole diameter that can minimize the difference between measured absorption coefficients and calculated absorption coefficients using equation 3.2.2 and 3.2.7 over the whole frequency range. The basic algorithm takes some function, $\alpha(\sigma, d)$ as shown in Equation 3.2.2, and a series of measured data points, and determines a vector (σ^*, d^*) of fitted geometric parameters such that the sum of the squares of the residues (i.e., the differences between the function and the measured data points). The least square data fitting problem can be stated as:

$$\min_{(\sigma,d)} \left\| \alpha(\sigma,d) - \alpha_{measured} \right\|_2^2 = \min_{(\sigma,d)} \sum_i \left(\alpha(\sigma,d,f_i) - \alpha_{measured}(f_i) \right)^2 \qquad (5.2.1)$$

subjected to

$$\begin{aligned} 0.1\% \le \sigma \le 5\% \\ 1e-4 \le d \le 2e-3 \end{aligned} \qquad (5.2.2)$$

where $\|\cdot\|$ denotes the 2-norm, and the i subscripts represent a particular data point at frequency f_i.

The numerical procedure used for this nonlinear least-square data fitting (NLLSF) is a modification of the basic Gauss-Newton procedure (Coleman, 1994, Coleman, 1996). This procedure is simply an algorithm which when given an initial guess, i.e. (1%, 1e-3), will find an appropriate search direction and step size, and therefore a better guess for the vector (σ, d). The procedure is then applied in an iterative fashion until the searching gradient is sufficiently small, within some specified tolerance.

After the data fitting is done, the quality of the fit is evaluated by the coefficient of determination, also known as pseudo-R^2, of the absorption coefficient α. The pseudo-R^2 is defined as

$$R^2 = 1 - \frac{SS_{residual}}{SS_{total}} \tag{5.2.3}$$

where $SS_{residual}$ is the sum-of-squares for distance of each measured point from the best-fit curve, while SS_{total} is the sum-of-squares for distance of each measured point from the mean of all measured data. The pseudo-R^2 is a fraction between 0 and 1, and has no units. Higher values indicate that the model fits the data better. The Pseudo-R^2 value indicates how well the curve approximates the measured points, but does not indicate whether the fit is unique.

In order to evaluate how certain the best-fit parameters are, the confidence region should be calculated and examined. The precision the parameter fit can also be evaluated by computing the confidence region of vector (σ, d) for certain confidence probability. The boundary of the confidence region can be determined by calculating the mean and covariance matrix of the bivariate vector (σ, d) (Chew, 1966, Rencher, 1995, Schultz, 2007). For bivariate problems, the boundary of the confidence region is defined as:

$$n\begin{pmatrix}\sigma-\mu_\sigma & d-\mu_d\end{pmatrix}\cdot\left(\mathrm{cov}(\sigma,d)\right)^{-1}\cdot\begin{pmatrix}\sigma-\mu_\sigma\\ d-\mu_d\end{pmatrix}=\chi^2(1-\gamma,2) \tag{5.2.4}$$

where n is the number of measured absorption coefficient (i.e. frequency lines), and σ and d are unknown boundaries of the confidence region for porosity and hole diameter, respectively. μ_σ and μ_d are the means of all candidate porosities and hole diameters for the given absorption coefficients. $\mathrm{cov}(\sigma,d)$ is the covariance matrix and $\chi^2(1-\gamma,2)$ is the bivariate Chi-Square Value for given confidence probability γ. The equation is a quadratic and represents an ellipse. A higher confidence probability means that it is more likely for the confidence region to include the best-fit value. For a given confidence level, a smaller confidence region implies that the model is more likely to uniquely fit the data. A

flow chart (Figure 5.6) summarizes the process for estimating the effective geometric parameters.

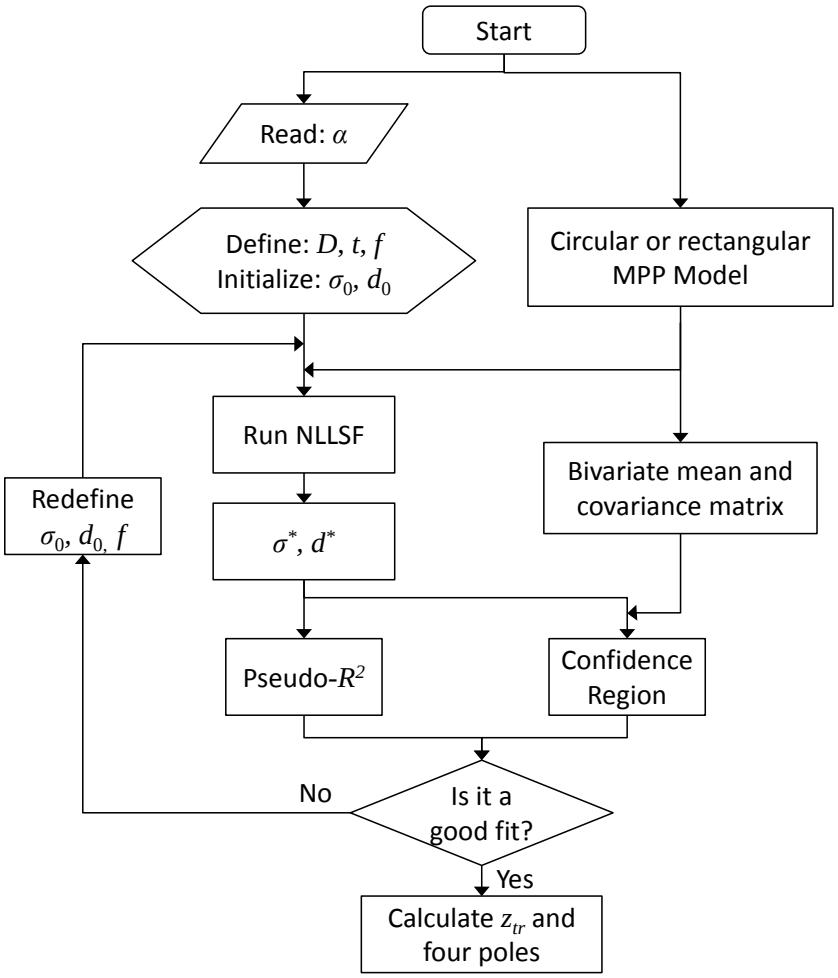

Figure 5.6 Flow chart of geometric parameter estimation algorithm.

5.2.3 Numerical Considerations and Results

The procedure described above was used to estimate the geometric parameters of an MPP absorber with slit-shaped perforations with 1 mm thickness, as shown in Figure 5.3. Porosity measured using a light meter is 1%, and the averaged measured slit width is 0.2 mm. Absorption coefficient was measured from 100 Hz up to 5000 Hz with 6.25 Hz increments using the two-microphone method in a 1.370 inch diameter impedance tube. In order to minimize the effect of measurement error at low and high frequencies, only frequencies from 500 Hz up to 4000 Hz are chosen for data fitting. The porosity and hole diameter estimated

using the circular hole model (Equation 3.2.2), are 4.4% and 0.22 mm, respectively. The rectangular slit model (Equation 3.2.7) yields 3.7% porosity and 0.13 mm slit width. It was anticipated that the estimates for porosity and slit dimension would be small for the rectangular slit model because resistance of rectangular slit is smaller than that of circular perforation. Figure 5.7 compares the measured absorption coefficient and fitted results. Notice that both models fit the measured data well.

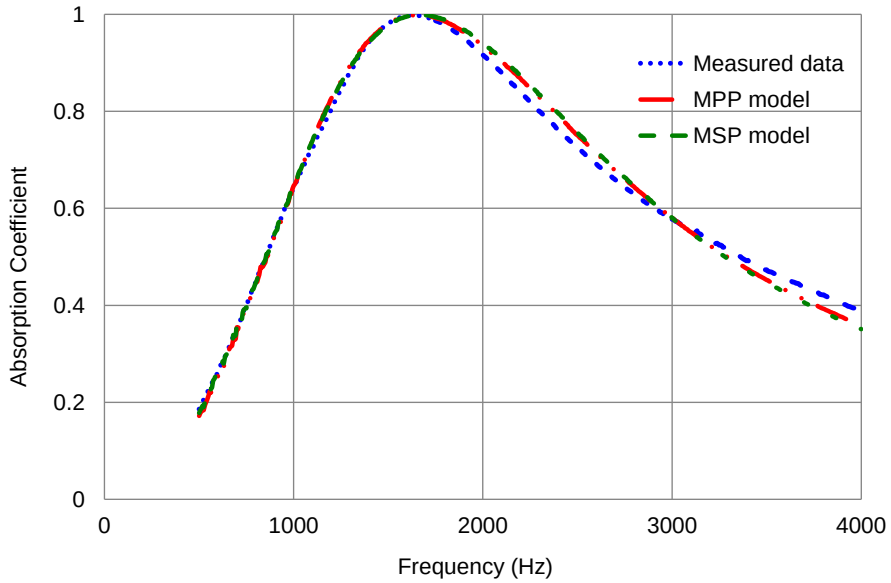

Figure 5.7 Comparison between measured and fitted absorption coefficients.

The pseudo-R^2 for the least squares curve fit was 99.87% and 99.81% for the circular and rectangular shaped perforate models, respectively. Confidence region in (σ, d) plane for fitting using the circular-shaped perforate model is shown in Figure 5.8. Notice that the best-fit point falls into the ellipses for both the 95% and 68% confidence regions. This indicates that the estimated parameters fit the data well and suggest that the algorithm is suitable for precise estimation of geometric parameters.

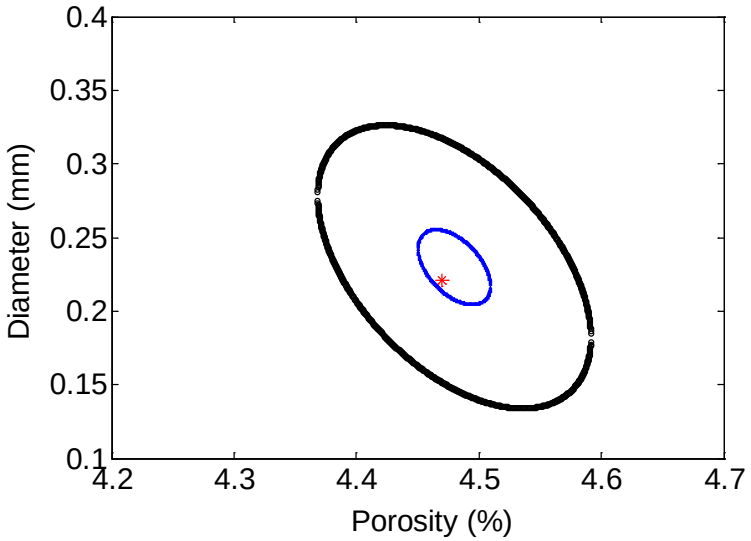

Figure 5.8 Confidence region for (σ, d) bivariate model fitting.

Once the geometric parameters are estimated, the transfer impedance can be calculated. Figure 5.9 compares the measures and calculated transfer impedance. Both the real and imaginary parts of the impedance compare well to the measured values.

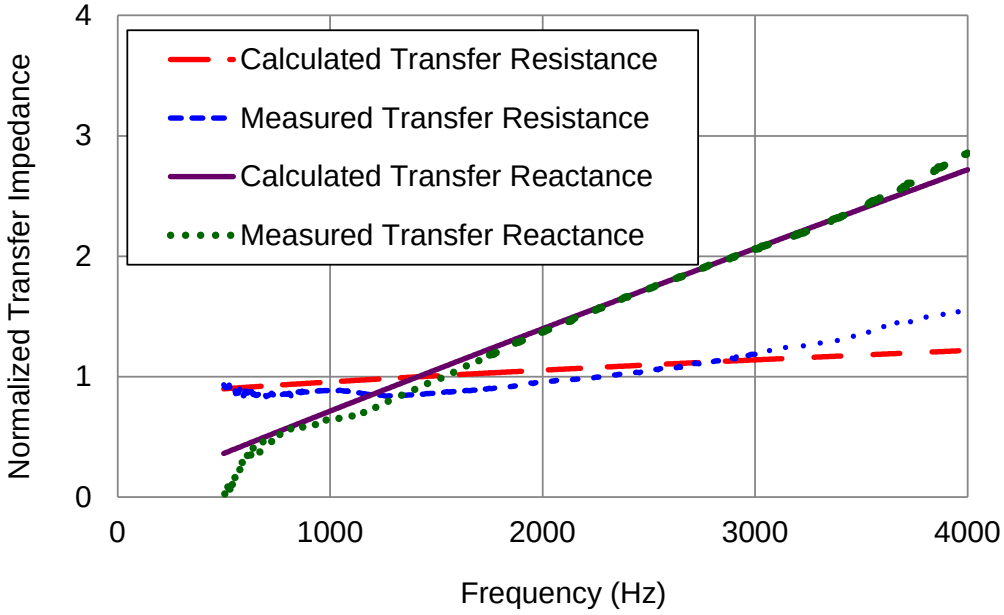

Figure 5.9 Comparison between measured and predicted transfer impedances.

One advantage of this method is that it can extrapolate the measured data to low frequencies. Transfer impedance data measured using the aforementioned

subtraction method is noisy at low frequencies due to low output from the loudspeaker and small differences between the sound pressures measured at the two microphone locations at low frequencies. For example, the transfer impedance of a MPP absorber with slit-shaped perforations with 1.5 mm thickness measured in a 4 inch diameter impedance tube is noisy below 300 Hz. By applying this method to fit the measured absorption coefficient from 300 Hz up to 2000 Hz, the hole diameter is estimated to be 0.24 mm and porosity is 2.95%. The fitted curve compares well to the measured absorption coefficient, as shown in Figure 5.10. The estimated parameters can then be used to calculate the transfer impedance at low frequencies. The predicted transfer impedance will be much smoother than the measured data below 300 Hz. This is illustrated in Figure 5.11.

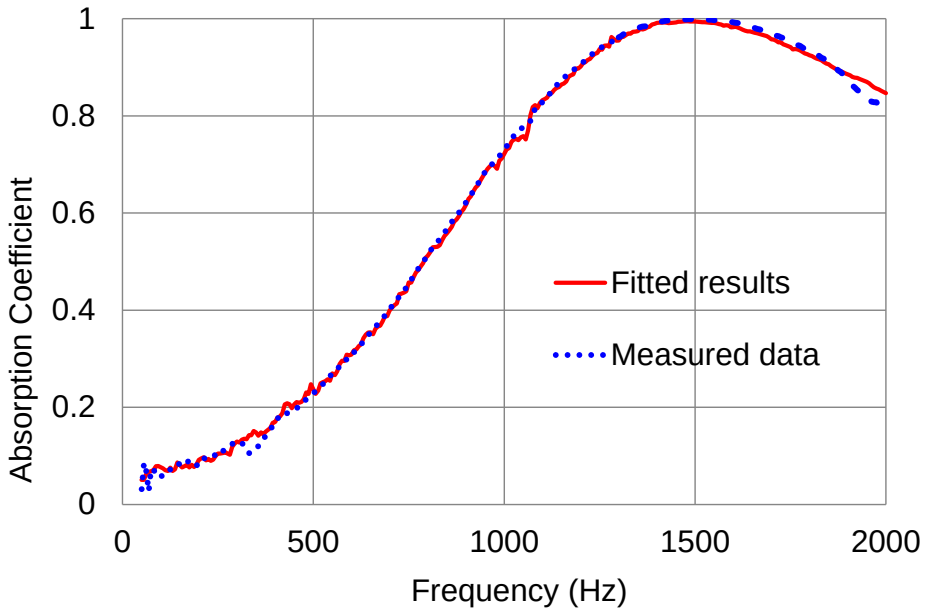

Figure 5.10 Comparison between measured and fitted absorption coefficients.

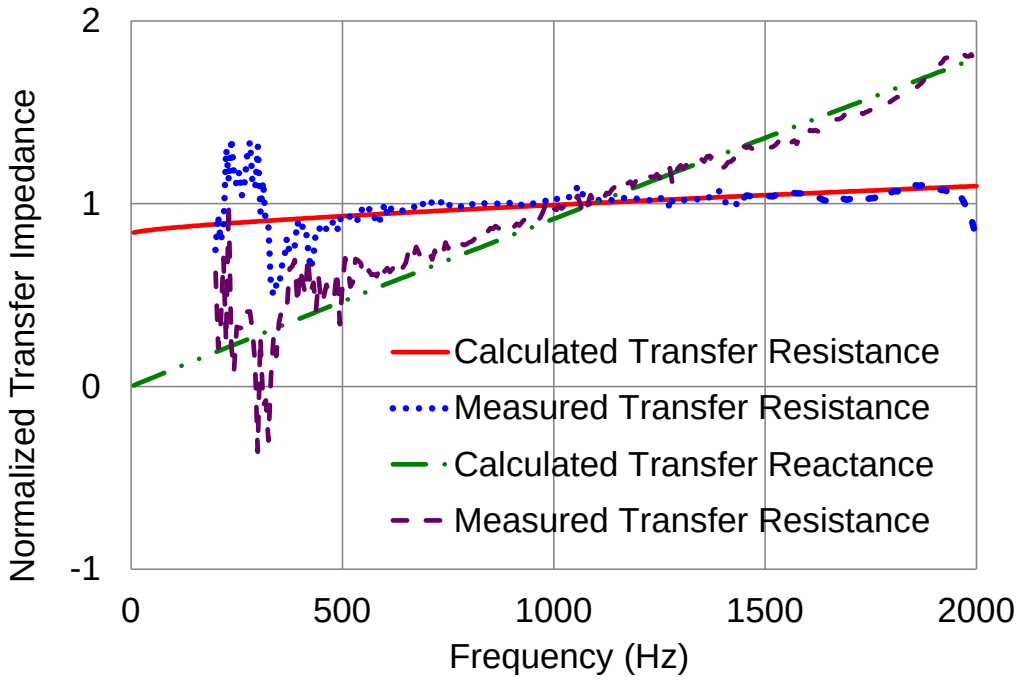

Figure 5.11 Comparison between measured and predicted transfer impedances.

In summary, MPP absorbers with slit-shaped perforations are difficult to model due to the fact that geometric parameters, i.e. slit size and porosity, are difficult to measure. An inverse method using a nonlinear least square data fitting algorithm was developed to estimate geometric parameters from the measured absorption coefficient data. Both the circular and rectangular perforation models can be used in the algorithm. The estimated geometric parameters can then be used to calculate transfer impedance and transfer matrix with good agreement compare to measured data. The same algorithm is used to aid in understanding the effect of dust and fluid contamination on the performance of MPP absorbers in the next section.

5.3 Effect of Dust and Fluid Contamination

As mentioned earlier, MPP absorbers are rugged, non-combustible, and do not deteriorate over time. This makes them a very attractive option for long-term use in harsh and corrosive environments. For example, it has been reported that MPP absorbers were used in noise barriers on mining sites (Pan, 2004), in

engine enclosures as an acoustical heat shield (Corin, 2005), and inside mufflers (Masson, 2008). However, after being exposed to these hostile environments for a certain amount of time, the MPP absorber openings are very likely to be filled with different types of contamination. Contamination can be either dust, dirt or fluid (i.e. oil, water). To our knowledge, there have been no prior studies to assess MPP performance when contaminated. Naturally, this effect will be important for engine enclosures, sound barriers and other industrial applications. By understanding this effect and the mechanism behind it, cleaning protocols can be established or absorbers can be designed to function well for known levels of contaminant accumulation.

In order to study the contamination effect, effective parameters can be estimated that predict the absorptive performance of a contaminated MPP absorber. Transfer impedances and absorption coefficients of MPP absorbers with and without contamination were measured and compared to determine the effect of contamination on performance. This was followed by simulation to explain the effect of contamination.

5.3.1 Dust contamination

Charcoal and aluminum oxide powder were chosen as dust contamination materials. The particle sizes of charcoal powder and aluminum oxide are approximately 40 and 80 microns, respectively. In order to allow the powder to accumulate evenly in an MPP slit, an airbrush was used to blow the powder inside a spray booth. The MPP was mounted in a direction normal to the flow. The flow speed was adjusted so that it would accumulate while not dislodging standing dust in the slit. The setup for this accumulation process is shown in Figure 5.12. After a certain amount of accumulation, the panel was removed from the booth and excess dust on the surface was carefully brushed off. Figure 5.13 shows MPP absorbers with slit-shaped perforations with different levels of charcoal dust accumulation.

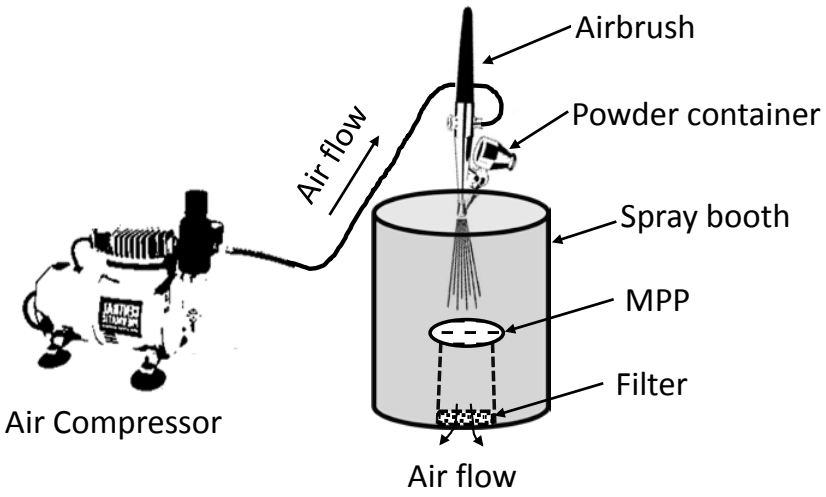

Figure 5.12 Setup for dust accumulating on MPP.

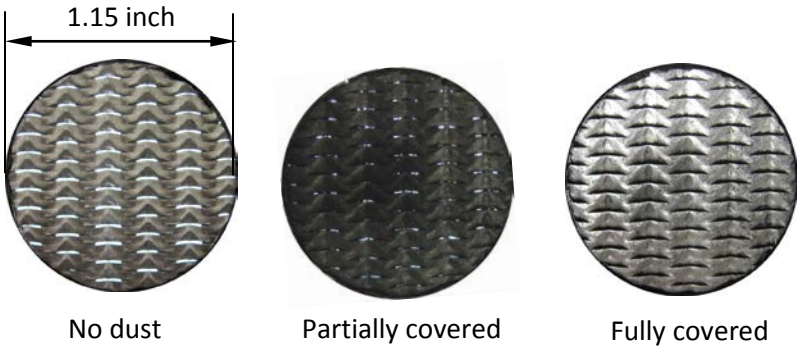

Figure 5.13 MPP with different levels of dust contamination.

Dust accumulation was quantified by placing a panel in between a luminance meter and a light pad, and measuring the light intensity through the panel. An estimate of the contamination was determined by measuring the light transmittance, which is the ratio of light intensities with and without the panel. The level of dust contamination can be estimate by comparing the porosities of the clean and contaminated samples. Though this process is prone to error, measurement using lumination can be used to quantify different accumulation levels in a relative sense.

Figure 5.14 Vertical impedance tube measurement setup.

After measuring the contamination level, the absorption coefficient and transfer impedance of the panel can be measured in the impedance tube. Normally, the impedance tube is placed horizontally on a flat surface. In this case, the impedance tube was hung vertically so that the accumulated dust in the slit was undisturbed during the measurement. The measurement setup is shown in Figure 5.14.

Figures 5.15 and 5.16 show the transfer resistance and reactance respectively of an MPP (1 mm thick with 1% porosity estimated from light transmittance), respectively with different levels of charcoal dust accumulation. Accumulation levels from 0% to 100% are defined as percentage of perforation filled with dust. It is the ratio between light transmittances with and without contamination. Figure 5.17 shows the corresponding absorption coefficients with a 1 inch backing cavity.

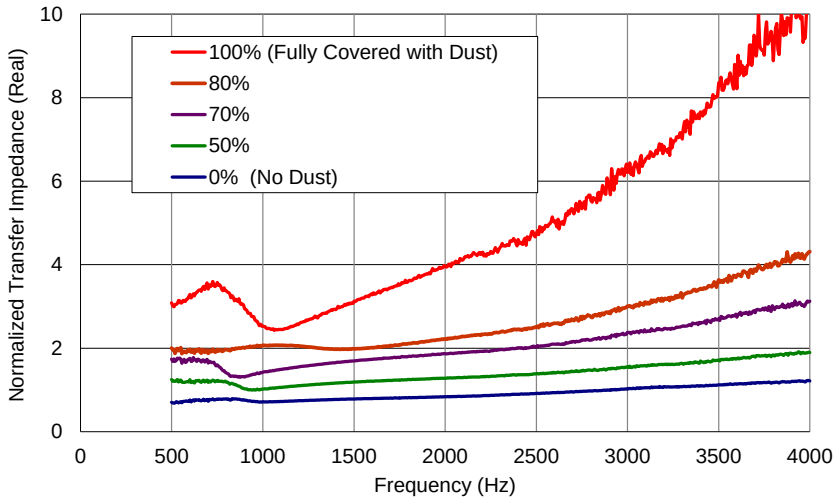

Figure 5.15 Transfer resistance of MPP with different levels of dust contamination.

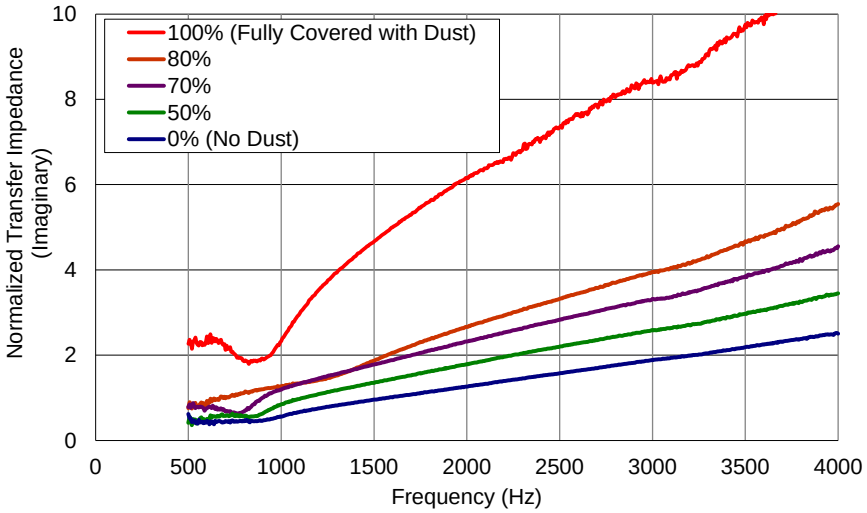

Figure 5.16 Transfer reactance of MPP with different levels of dust contamination.

It can be observed from Figures 5.15 and 5.16 that dust contamination increases both the resistive and reactive parts of the transfer impedance. Dust contamination decreases the absorption and shifts the absorption band lower in frequency, as shown in Figure 5.17. This demonstrates that dust contamination can compromise the performance. Similar results were obtained for aluminum oxide contamination.

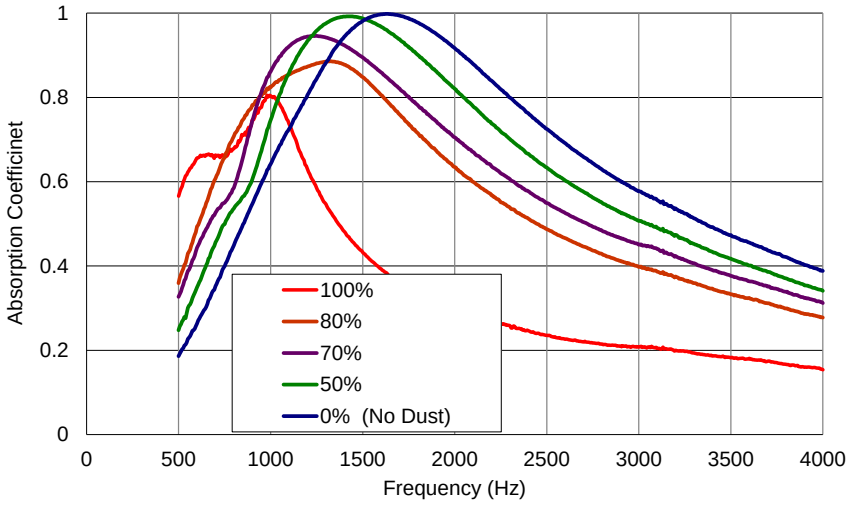

Figure 5.17 Absorption coefficients of MPP with different levels of dust contamination.

However, dust contamination does not necessarily decrease the absorption coefficient. In some cases, dust contamination might actually improve the absorption. For example, for a very thin MPP, the small thickness limits its resistance. When placed 1 inch in front of a wall, the peak value of its absorption coefficient is around 0.75 as shown in Figure 5.18.

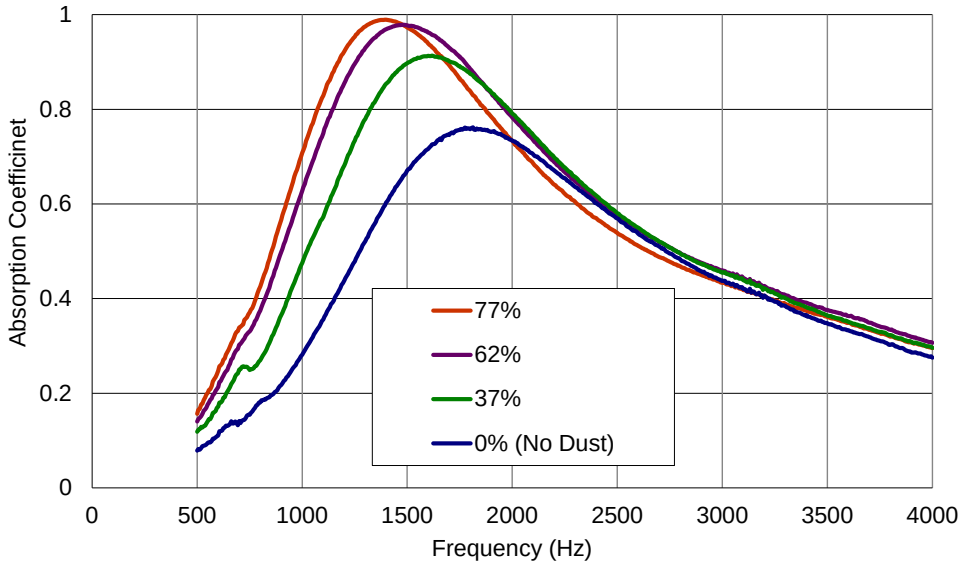

Figure 5.18 Dust contamination improves the acoustic performance of a thin MPP.

With dust contamination, the peak value is increased from 0.75 to nearly 1.0 and the absorbing band is broadened. Notice that the peak absorption shifts to lower frequencies. In order to obtain a peak value around 1400 Hz without contamination, a cavity depth of 1.5 inches is required as shown in Figure 5.18. Contamination enables the MPP to provide better acoustic performance while reducing the volume of the absorber by a third. This suggests that if the dust accumulation level is known in advance, it can be included as a design parameter so that the uncontaminated MPP porosity and slit dimensions are optimized in advance.

5.3.2 Fluid contamination

Distilled water and gasoline were used to investigate the effect of fluid contamination. The fluid is first sprayed onto the panel until the slit is fully filled and then the surface is carefully wiped with cloth. Light transmittance measurement is skipped since the fluid is somewhat transparent. The panel was measured in an impedance tube. After each measurement, there is a vaporization step to gradually reduce the amount of fluid in the slit. Vaporization is accomplished by slowly blowing hot air (80 ºC) on the panel.

An MPP absorber with slit-shaped perforations (1 mm thick with 1% porosity estimated from light transmittance) was used to investigate the effect of fluid contamination. Figures 5.19 and 5.20 show the transfer resistance and reactance respectively with water contamination.

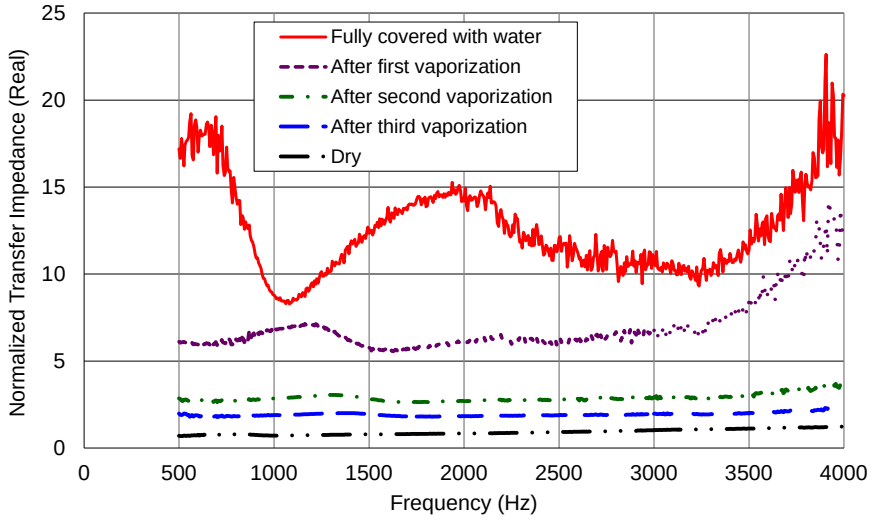

Figure 5.19 Transfer resistance of MPP with water contamination.

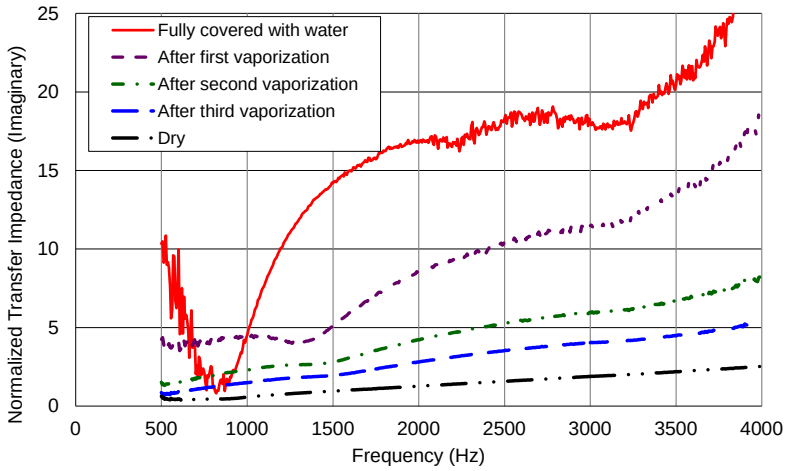

Figure 5.20 Transfer reactance of MPP with water contamination.

Figure 5.21 shows corresponding absorption coefficients of the MPP absorber with a 1 inch backing cavity. Similar to the effect of dust contamination, fluid contamination increases both the transfer resistance and reactance. The results suggest that fluid contamination has a larger effect than dust contamination though the trend is similar. Similar results were obtained for gasoline contamination.

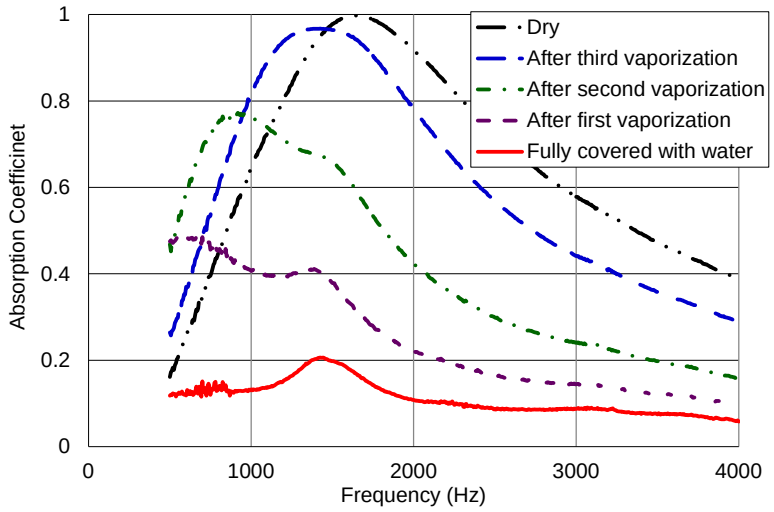

Figure 5.21 Absorption coefficients of MPP with different levels of fluid contamination.

5.3.3 Simulation

In the previous section, a least square approach was developed to evaluate the effective parameters for irregular-shaped slit MPP absorbers based on Maa's equation and the measured absorption coefficient. It was assumed that a MPP absorber with slit-shaped perforations could be simulated in Maa's equation, which assumes circular-shaped perforations, using an effective porosity and hole diameter. It was hypothesized that the effect of contamination is equivalent to reducing the porosity and hole diameter simultaneously, while the effect of fluid contamination is equivalent to increasing the dynamic viscous factor in the perforation.

In order to test the first hypothesis, the effective parameters estimation approach was applied to measured absorption coefficients for different levels of dust accumulation. The target parameters are still effective porosity and hole diameter. The porosity measured using the light intensity approach is used to indicate the dust accumulation levels. Notice that this porosity is not an accurate measure of dust level and serves merely as an indicator in a relative sense. Figures 5.22 and

5.23 show comparisons between simulated and measured transfer impedance and absorption, respectively. The simulated results are calculated by substituting effective parameters into Maa's equation. Notice the good agreement between simulation and measurement.

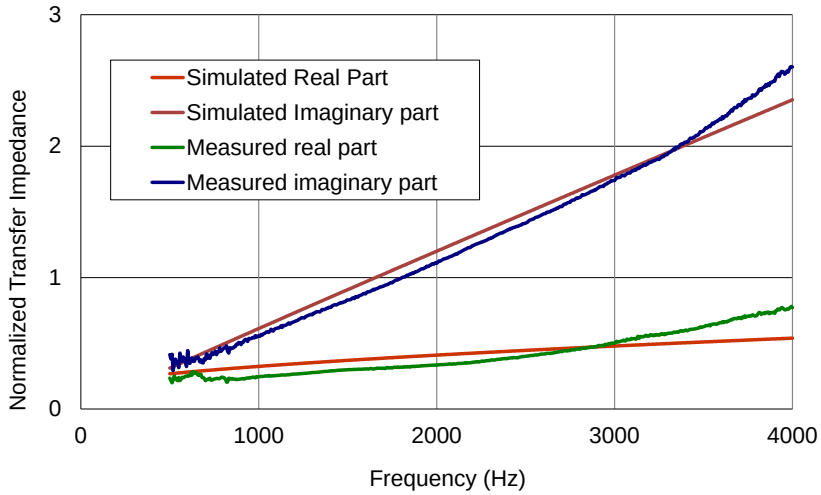

Figure 5.22 Transfer impedance comparison for MPP with dust contamination.

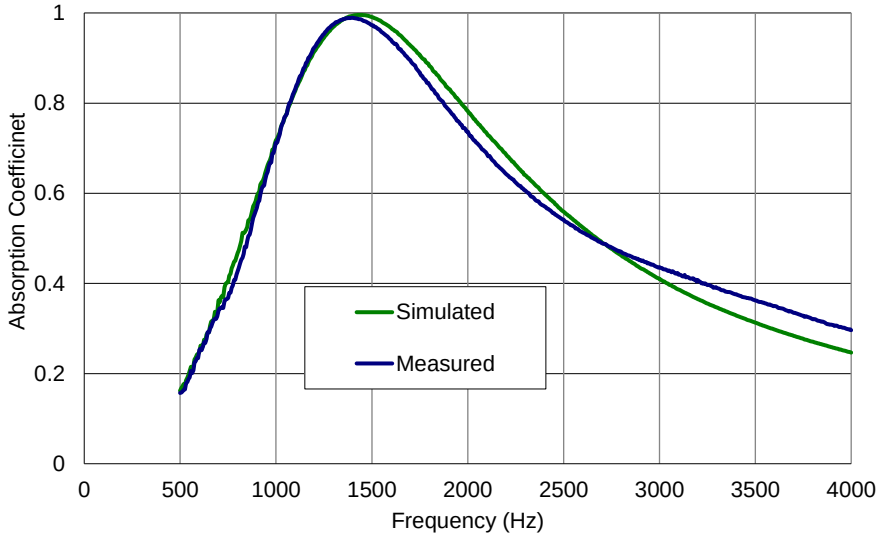

Figure 5.23 Absorption coefficient comparison for MPP with dust contamination.

By applying this approach for different levels of dust accumulation, the estimated effective parameters can be obtained in each case. Figure 5.24 shows the measured absorption coefficients and measured accumulation levels.

Accumulation levels from 0% to 77% are defined as percentage of perforation filled with dust. Additionally, the corresponding fitted absorption coefficients, and estimated porosity and hole diameter are also shown. Notice the good agreement between measured and fitted absorption coefficients. It can be observed that the dust contamination reduces both the effective porosity and hole diameter simultaneously, which confirms the hypothesis.

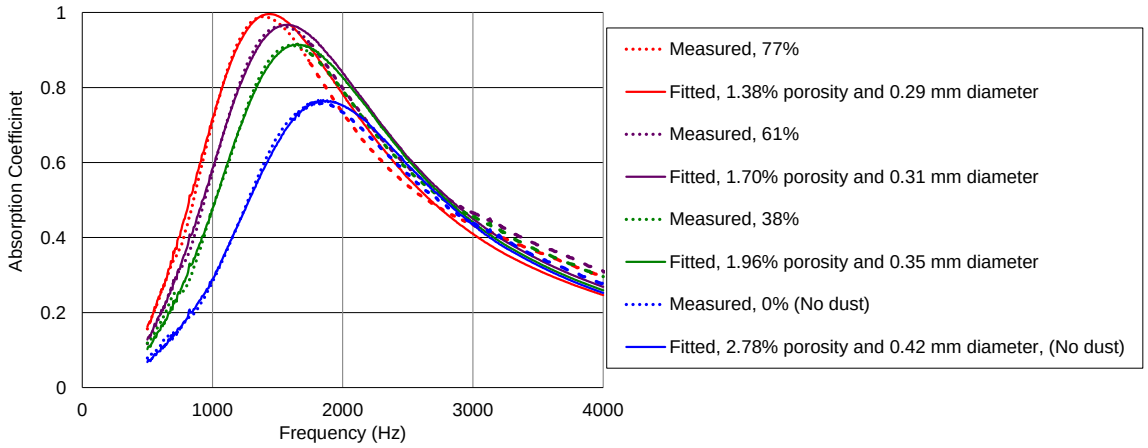

Figure 5.24 Estimated parameters and corresponding absorption coefficient prediction.

It seemed that the aforementioned least square approach would be a suitable candidate for estimating the amount of fluid contamination inside of the perforations. In order to estimate the amount of fluid contamination, the target effective parameter is the percentage of the perforation filled with fluid. In the perforation, there are two acoustic paths with two different fluid viscous factors: one is through air (viscous factor 1.83×10^{-5} $\mathrm{Pa}\cdot\mathrm{s}$) and the other is through the fluid or water (8.9×10^{-4} $\mathrm{Pa}\cdot\mathrm{s}$). These two paths are in parallel with each other. Therefore the transfer impedance of each portion of perforation occupied by different fluids can be individually calculated based on viscous factor and the percentage of perforation occupied. Overall transfer impedance can be calculated based on equivalent circuit analogy of impedances. The equivalent transfer impedance is

$$z_{tr} = \frac{z_{tr\_air}(\eta_1, 1-x) \cdot z_{tr\_fluid}(\eta_2, x)}{z_{tr\_air}(\eta_1, 1-x) + z_{tr\_fluid}(\eta_2, x)} \tag{5.3.1}$$

where x is the percentage of the perforation filled with fluid, it varies from 0%, i.e. dry, to 100%, i.e. fully covered with fluid. The least square data fitting problem can be stated as:

$$\min_x \left\| \alpha(x) - \alpha_{measured} \right\|_2^2 = \min_x \sum_i \left(\alpha(x, f_i) - \alpha_{measured}(f_i) \right)^2 \tag{5.3.2}$$

subjected to $0 \le x \le 1$, where $\|\cdot\|$ denotes the 2-norm, and the i subscripts represent a particular data point at frequency f_i. Figure 5.25 shows a comparison between measured and simulated absorption coefficients.

As shown in Figure 5.25, the simulated results suggest that there is 0.1% of perforation filled with water when the panel is dry, and 99% of perforation filled with water when the panel is fully covered with water. Using this approach, it's evident that the estimated percentages accurately represent the acoustic performance of the contaminated absorber.

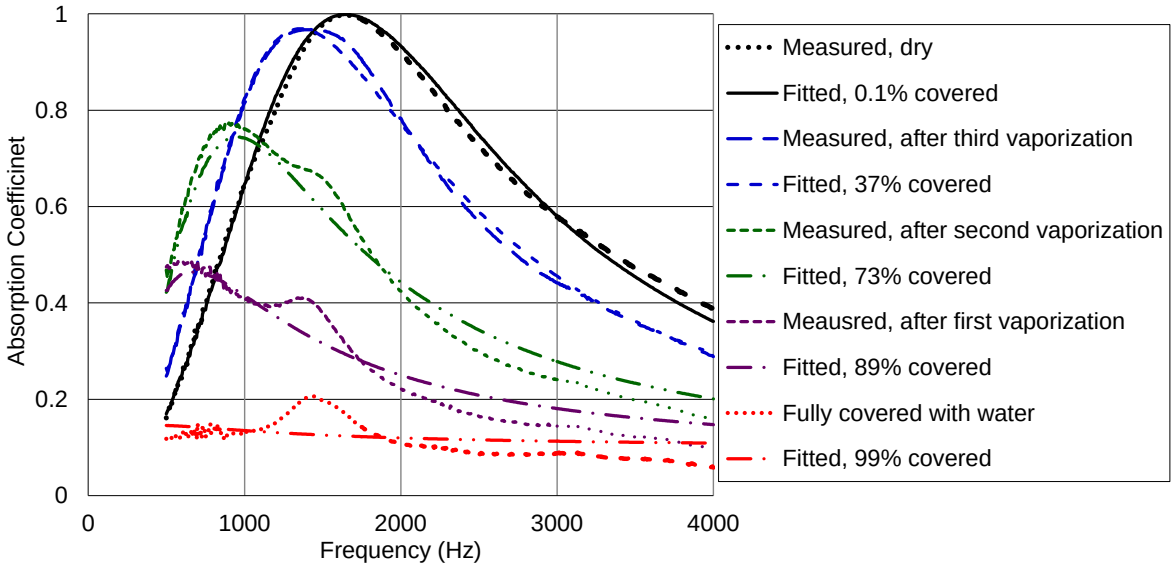

Figure 5.25 Measured and simulated absorption coefficients comparison.

In summary, dust and fluid contamination increase both the transfer resistance and reactance. Both contamination effects can be simulated by varying effective parameters which plausibly explain the effect. Simulations suggest dust

contamination reduces both the effective porosity and hole diameter simultaneously, while fluid contamination leads to a parallel impedance in the hole through the air and fluid. Results demonstrate that contaminations may compromise or improve the acoustic performance depending on the panel design and the contamination accumulation levels. By understanding this effect and the mechanism behind it, cleaning protocols can be established or absorbers can be designed to function well for known levels of contaminant accumulation.

5.4 Enhancing Microperforated Panel Attenuation by Partitioning the Adjoining Cavity

5.4.1 Application of MPP as lining in HVAC duct

An experimental study was undertaken to compare the performance of a MPP to that of open cell foam in a silencer. In this case, the MPP was of the micro-slit absorber type. A 1 m x 0.5 m x 0.5 m silencer was constructed as shown in Figure 5.26. A 1 m x 0.5 m micro-slit absorber with 2.5% porosity and 1.2 mm thickness was attached to one side of the plenum as shown. The depth of the air cavity was intentionally set to 30 mm so that maximum attenuation was anticipated around 1500 Hz. A piece of wood was inserted into the middle of the plenum to obstruct the line-of-sight sound path between inlet and outlet ducts. During the experiment, the sound pressure level at the inlet and outlet of the plenum was measured so that the noise reduction could be obtained.

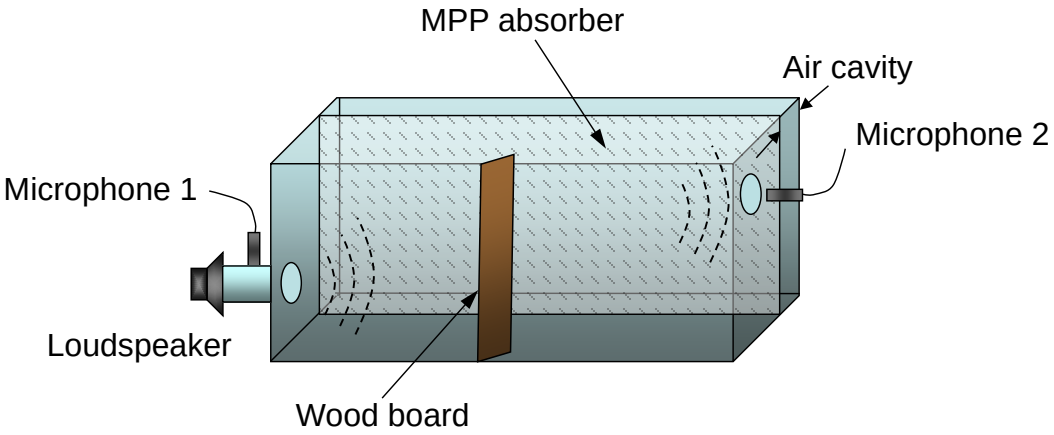

Figure 5.26 Experiment configuration for MPP in silencer.

The noise reduction of the silencer without the MPP was compared to that of open cell PUR foam with the same thickness (30 mm). Thus, both the MPP and foam occupied the same volume in the silencer. Figure 5.27 shows the inside of the silencer with the accompanying MPP and foam.

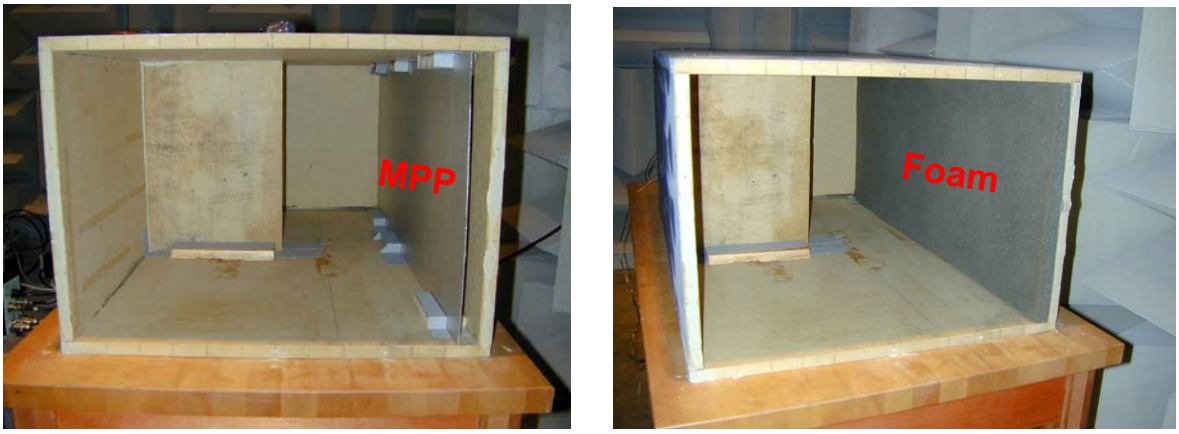

Figure 5.27 Silencer with MPP and foam lining.

Figure 5.28 shows a comparison of the noise reduction. The baseline without any MPP or foam absorber is also included. Notice that the MPP improves upon the baseline configuration especially at frequencies above 1000 Hz. However, the noise reduction accomplished using a foam absorber having the same thickness is approximately 3 dB higher than that of the MPP.

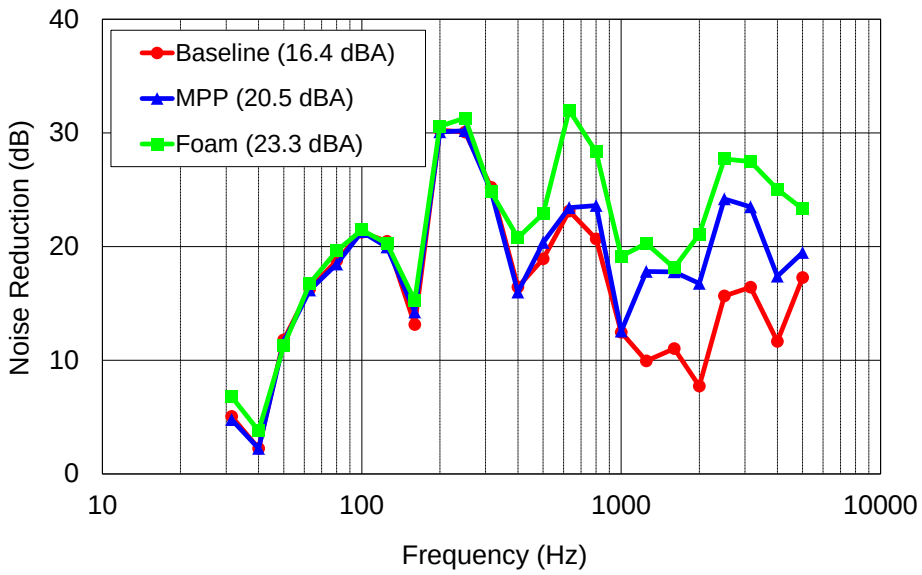

Figure 5.28 Noise reduction comparison.

Figure 5.29 shows a comparison of the absorption measured in an impedance tube for the foam and MPP used in the aforementioned experiment. The absorption of the normal incident sound wave was measured using the ASTM E-1050 standard. Notice that the measurement indicates a high absorption coefficient of close to 1.0 for the MPP at approximately 1500 Hz. Though normal incidence of the sound is expected in the impedance tube, oblique incidence is expected within the silencer. Thus, the high absorption coefficient measured in the tube is not achievable in practice for a silencer. The noise reduction difference between the MPP and foam can be explained by considering the sound wave propagation in the lateral or transverse direction. Foam is an isotropic and porous material with high flow resistivity. It can be assumed to be locally reacting because there is almost no sound propagation in the transverse direction. However, the sound propagation for an MPP in the transverse direction cannot be ignored. Modes in the backing cavity will be excited adversely affecting the noise reduction performance of the MPP.

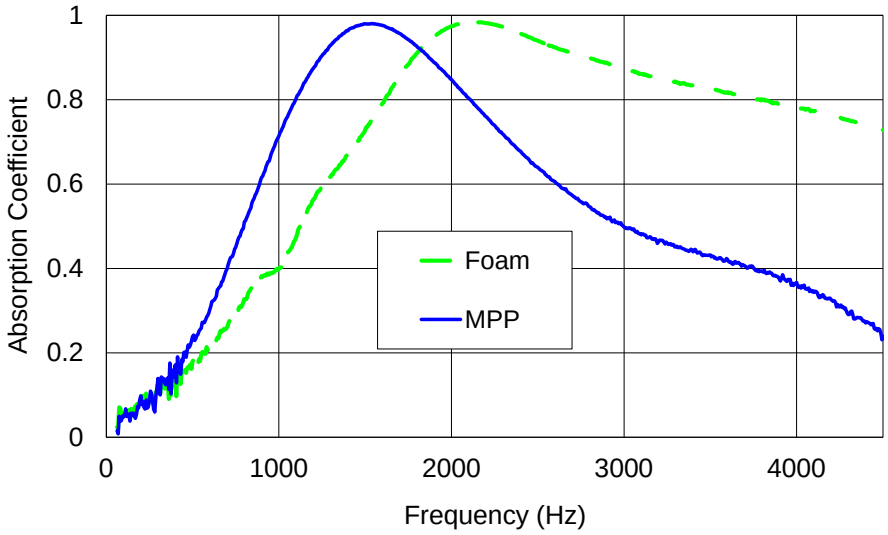

Figure 5.29 Absorption comparison between foam and MPP.

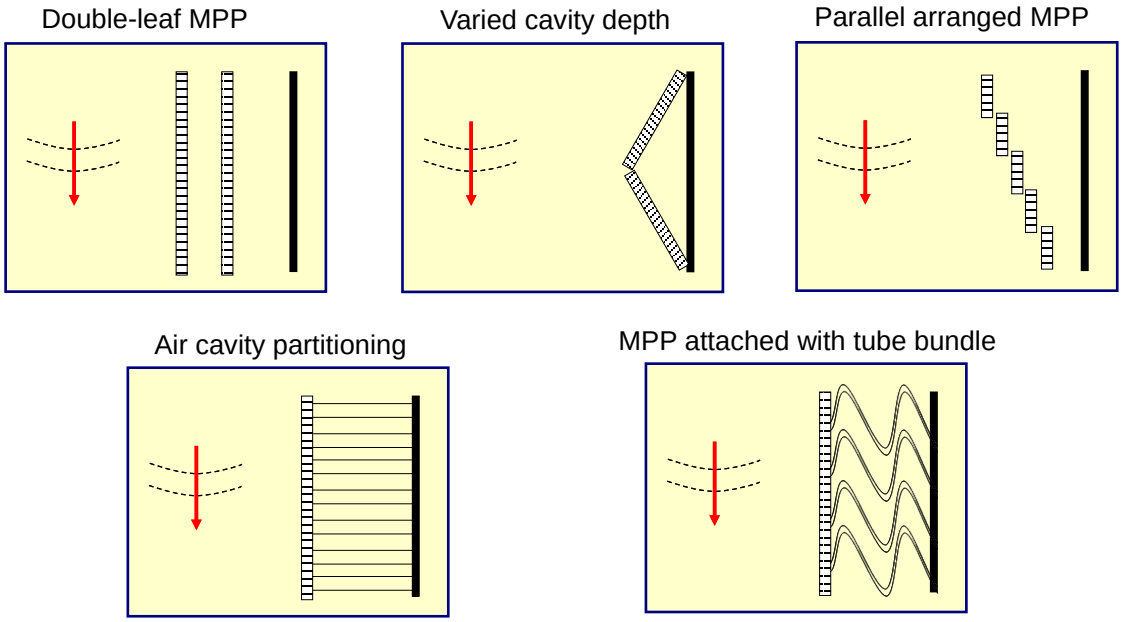

Figure 5.30 A summary of various improvement strategies.

In order to improve the MPP performance, various strategies to treat the air cavity have been proposed and examined (Zhang, 1998, Yairi, 2005, Sum, 2006). These include partitioning the air cavity, arranging absorbers in parallel while varying cavity depths, layering absorbers, and introducing tube bundles to the back of the MPP. These enhancing strategies are summarized in Figure 5.30.

Yairi et al (2005) discovered that partitioning the air cavity was especially effective. Partitioning the backing cavity is the focus of this study. The results in this section agreed with what Yairi et al observed.

5.4.2 Partitioning the Backing Cavity

Partitioning the air cavity was considered to improve the noise reduction of the MPP. To implement this strategy, a honeycomb structure, with 30 mm depth and a cell size of 40 mm x 40 mm was inserted behind the MPP. The MPP was affixed to the front of the cardboard partitioning. It should be noted that the honeycomb structure itself provided almost no noise reduction by itself. The Experimental setup is shown in Figure 5.31. The figure also shows a schematic of a grazing sound wave.

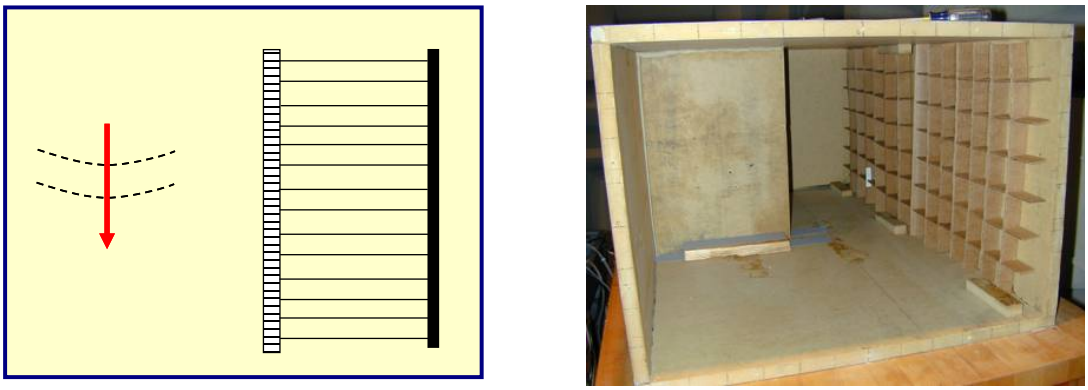

Figure 5.31 illustration and experimental setup of silencer with partitioned cavity.

Figure 5.32 shows a comparison of the noise reduction with a partitioned cavity. Notice that partitioning the cavity improves the noise reduction by close to 2 dB.

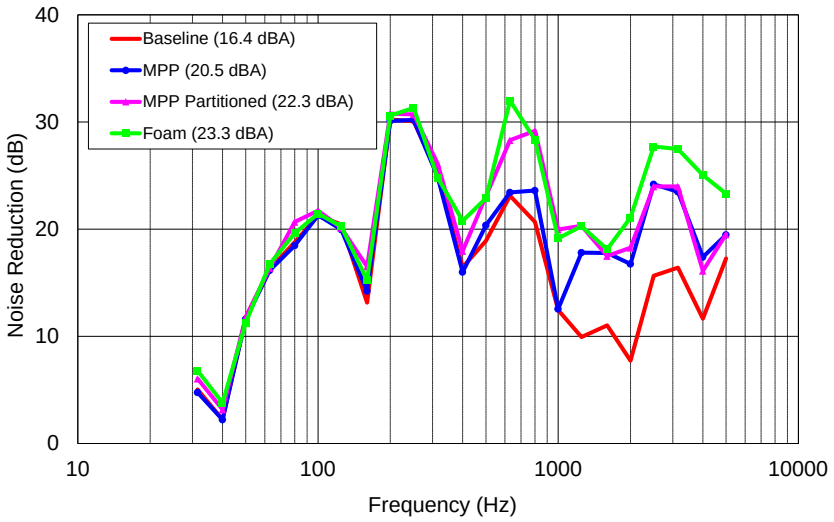

Figure 5.32 Comparison of noise reduction for MPP with partitioned cavity.

It is hypothesized that partitioning prevents grazing sound propagation behind the MPP, and forces the particle velocity to be normal to the panel. Thus, the panel becomes locally reacting at higher frequencies. Figure 5.33 illustrates the hypothesized effect. The next section explores this hypothesis in further detail (Astley, 1987).

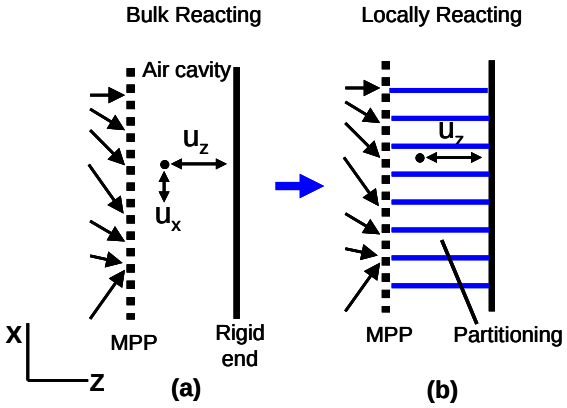

Figure 5.33 Schematic showing the effect of adding portioning behind the MPP.

The effect of partitioning the air cavity has been noticed by several researchers. Toyoda and Takahashi investigated the effect of subdividing the adjoining air cavity on the oblique incident transmission loss of an MPP (Toyoda, 2008). Their results suggested that partitioning the air cavity improved the transmission loss at mid-frequencies by means of providing a motion-constraint condition to the

particles so that the acoustic wave could only propagate normal to the MPP. Yairi et al (2005) tested the MPP's with an alternative honeycomb partitioning in the adjoining cavity. Agreeing with Toyoda and Takahashi, they showed that the honeycomb affected only the oblique incidence absorption coefficient and had a minimal effect on normal incidence absorption.

Hillereau et al (Hillereau, 2005) considered a more complicated case where honeycomb cell walls themselves were also porous. They studied the sound attenuation of an ordinary perforated panel under grazing incidence, and concluded that the variation of the honeycomb porosity had a significant impact on the acoustic attenuation of a given perforated facing panel. In this situation, the partitioning cannot be simplified as a device that merely forces the oblique incident wave into a normal incident wave in the cell.

The purpose of this section is to experimentally investigate the effect of partitioning the adjoining air cavity on plenum acoustics. Yairi and Toyoda's work investigated the physics of an MPP with adjoining cavity for different incident wave angles. The current work builds on this by looking at the effect of the MPP and adjoining cavity on the plenum cavity (the cavity of interest). The partitioning behind the MPP is non-porous though it is light and not rigid.

The objective of this work was to better understand acoustic behavior inside a plenum with and without honeycomb partitioning. Fenech et al (Fenech, 2006) conducted a similar study where the effect of a MPP on the acoustic modes inside of a closed cavity was investigated. They noted that the MPP was effective at damping the acoustic cavity modes normal to the MPP but ineffective at damping modes tangential to the MPP. This paper examines the significance of partitioning the adjoining cavity on the acoustic modes in a plenum. Figure 5.34 shows an end view of the silencer with the honeycomb partitioning of the air cavity. For this investigation, a loudspeaker was attached via a short tube to a plenum having dimensions 0.96 m x 0.57 m x 0.42 m. The experimental setup is shown in Figure 5.35.

Figure 5.34 Photograph showing cardboard partitioning in the end of cavity behind the MPP.

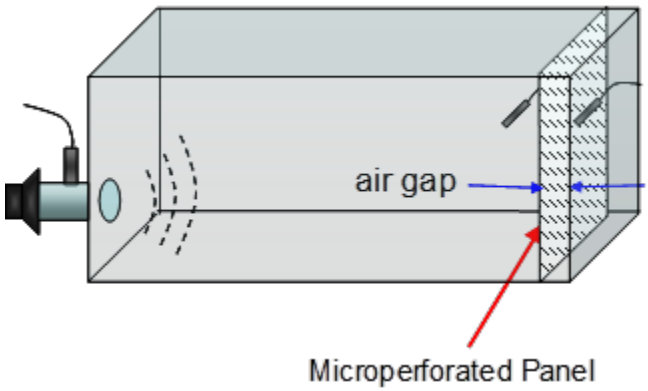

Figure 5.35 Schematic showing measurement setup.

The MPP utilized had slit-shaped perforations. The transfer impedance was measured in impedance tube using the impedance subtraction method and is shown in Figure 5.36.

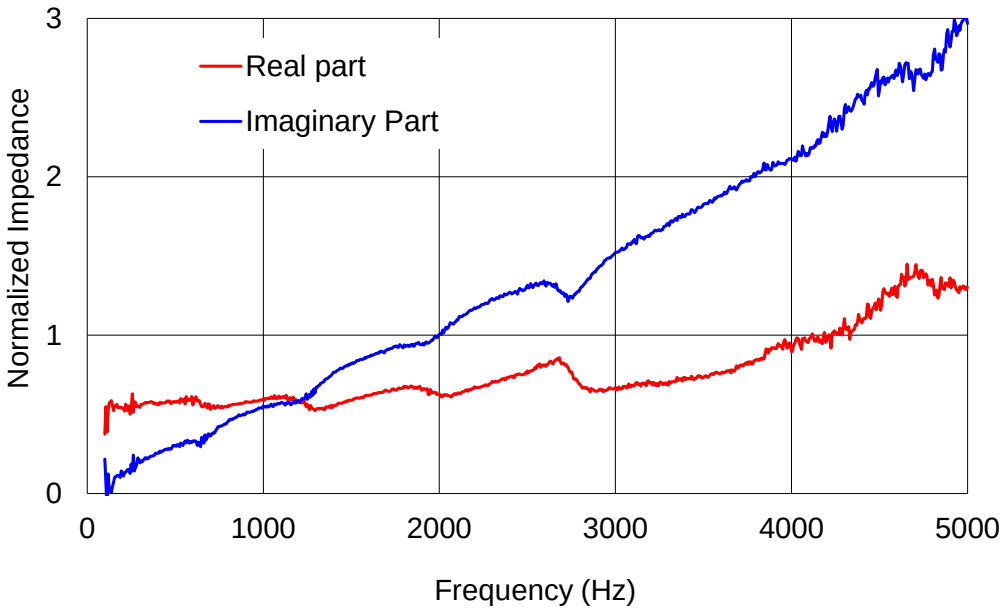

Figure 5.36 Measured Transfer Impedance of an aluminum micro-slit Absorber.

Figure 5.37 compares the normal incident absorption coefficient of an MPP with 65 mm cavity predicted using the transfer impedance with that measured directly using the two-microphone method (ASTM, 1998).

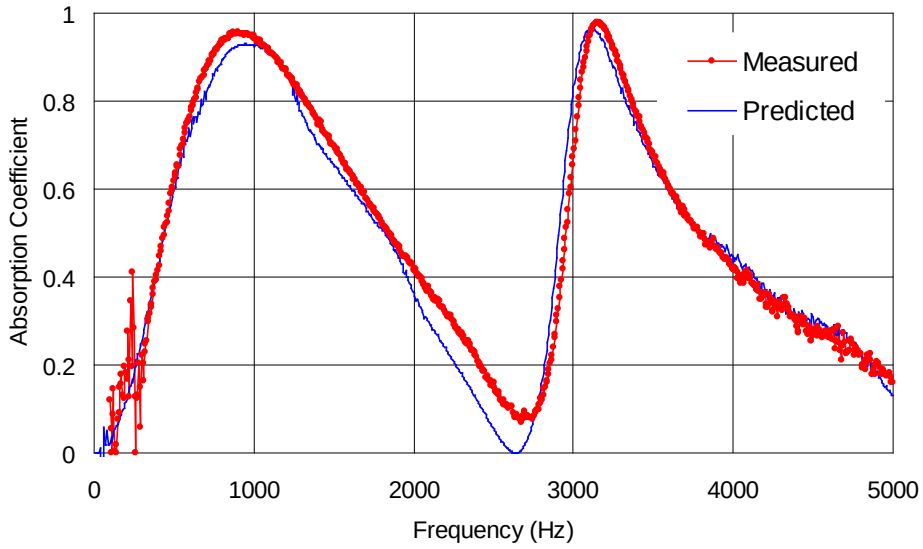

Figure 5.37 Normal incident absorption coefficient of MPP with 65 mm air cavity.

The MPP treatment was placed on the side of the plenum opposite the source. Several different configurations were applied and tested. These included three cases:

- Untreated.
- MPP absorber with 65 mm back cavity and no partitioning.
- MPP absorber with 65 mm back cavity with a cardboard partitioning. Cells are honeycomb shaped. If the partitioning is placed in the plenum without a MPP facing, negligible additional attenuation was noted. This suggested that the cardboard did not absorb the sound.

For each condition, sound pressure was measured at a plane located 95 mm from the treated end of the plenum (30 mm anterior to the MPP with a 65 mm adjoining cavity depth). In each case, the measurement plane consisted of 54 points. Measurement points were spaced 3.8 cm and 5.6 cm apart in the horizontal and vertical directions, respectively.

The natural frequencies of the plenum can be calculated using

$$f(l,m,n) = \frac{c}{2}\sqrt{\left(\frac{l}{L}\right)^2 + \left(\frac{m}{W}\right)^2 + \left(\frac{n}{H}\right)^2} \tag{5.4.1}$$

in which, l, m, n are mode indices indicating the x, y, and z directions, respectively. L, W, and H indicate the respective length, width and height of the plenum. The modes involving a single dimension are termed axial modes. For example, this would include the (1,0,0) and (0,2,0) modes. Tangential modes involve 2 dimensions (i.e the (1,0,1) and (0,2,1) modes). Oblique modes involve 3 dimensions (i.e. the (1,1,1) or (2,1,2) modes). The error between measured and predicted natural frequencies is less than 5 Hz.

Figure 5.38 demonstrates the attenuation due to introducing an MPP absorber. In this plot, a type of insertion loss is shown. The difference was determined between a spatial average of pressure (from 54 sound pressure measurements) on a plane 30 mm anterior to the MPP absorber and a baseline case with no MPP absorber treatment. This insertion loss is shown in 1/12 Octave bands. The figure also includes a curve showing the effect of partitioning added posterior

to the MPP absorber. As anticipated, introducing partitioning improves the effectiveness of the treatment. The overall insertion loss of the MPP absorber without posterior partitioning is 1.5 dB while adding partitioning improves the performance by 3.2 dB. Overall insertion loss is calculated by determining the overall spatially averaged sound pressure on the measurement plane for the treated and untreated cases and taking the difference. Notice the distinct lower frequency peaks due to the acoustic modes in the plenum. At higher frequencies, the response is quasi diffuse in nature, and the attenuation of the MPP absorber is less irregular.

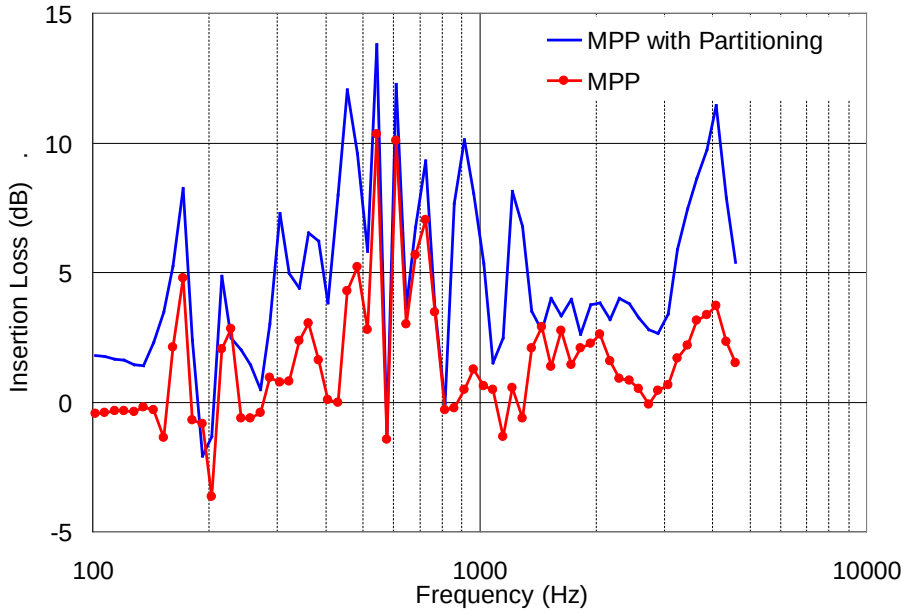

Figure 5.38 Insertion loss comparison in 1/12 Octave bands.

Figure 5.39 shows the narrowband insertion loss from 0 to 1000 Hz, and also notes the acoustic modes which correspond to some of the more prominent insertion loss peaks. Observe that the insertion loss peaks and nadirs occur at acoustic resonances and anti-resonances respectively.

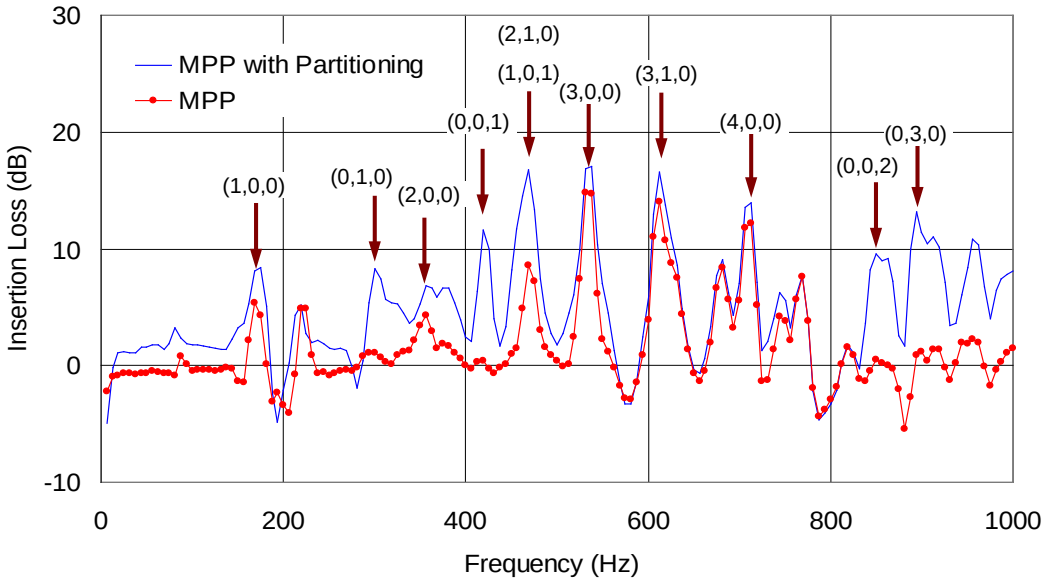

Figure 5.39 Insertion loss below 1000 Hz including corresponding modes in narrow bands.

This information is summarized in Table 5.1. Table 5.1 shows the insertion loss at different modal frequencies for the MPP with and without partitioning. The table separates the modes by their different behavior (i.e. axial, tangential or oblique).

Notice that the MPP is effective without partitioning for axial modes in the x-direction (11.2 dB average insertion loss). This corresponds to the effect noticed by Fenech et al (Fenech, 2006). This can be likened to a normal incident wave being absorbed. In contrast, axial modes in the y- and z- directions have an average insertion loss of less than 1 dB without partitioning posterior to the MPP. Notice that partitioning improves the attenuation by over 8 dB for axial modes in the y- and z- directions. However, the effect is modest for modes in the x-direction (2.2 dB). The results suggest that the partitioning disrupts the mode shape in the neighborhood of the MPP. This will be illustrated via contour maps in the subsequent section.

The tangential and oblique modes further support this mode disruption premise. Notice that the insertion loss improves by over 8 dB for tangential modes that do

not involve the x-direction. However, the insertion loss gains are more modest for tangential and oblique modes involving the x-direction (4.4 dB improvement).

Table 5.1. Insertion Loss at Modal Frequencies for MPP with and without Partitioning.

	x	y	z	Frequency (Hz)	MPP Insertion Loss (dB)	MPP with Partitioning Insertion Loss (dB)	MPP Insertion Loss (averaged)	MPP with Partitioning Insertion Loss (averaged)
Axial modes in x direction	1	0	0	178	5.4	8.1	11.2 dB	13.3 dB (improve 2.2 dB)
	2	0	0	357	4.3	6.8		
	3	0	0	535	14.7	17.0		
	4	0	0	713	12.2	13.9		
Axial modes in y and z	0	1	0	301	0.7	7.5	0.6 dB	8.8 dB (improve 8.1 dB)
	0	0	1	418	0.4	11.6		
	(0,2,0), (0,0,2),etc. Total 6 modes							
Tangential modes in y and z	0	1	1	515	0.1	4.5		
	0	1	2	889	-2.7	9.9		
	(0,2,1),(0,3,1), etc. total 6 modes							
Tangential modes involves x	1	1	0	350	3.4	5.3	4.3 dB	8.8 dB (improve 4.4 dB)
	1	0	1	455	1.5	11.7		
	(2,1,0),(2,0,1), etc. total 19 modes							
Oblique modes involves x, y and z	1	1	1	545	6.2	10.3		
	2	1	1	627	8.8	10.9		
	(3,1,1),(1,2,1), etc. total 19 modes							

Figure 5.40 shows a measured sound pressure contour map (for a plane 30 mm anterior to the MPP absorber) at a frequency corresponding to the (0,0,1) mode in the z- direction. Contour maps are shown for the aforementioned three conditions (untreated, MPP absorber, MPP absorber with partitioning). Notice that the contour maps are essentially identical for the first two conditions. However, introducing partitioning reduces the sound pressure while also disrupting the acoustic mode.

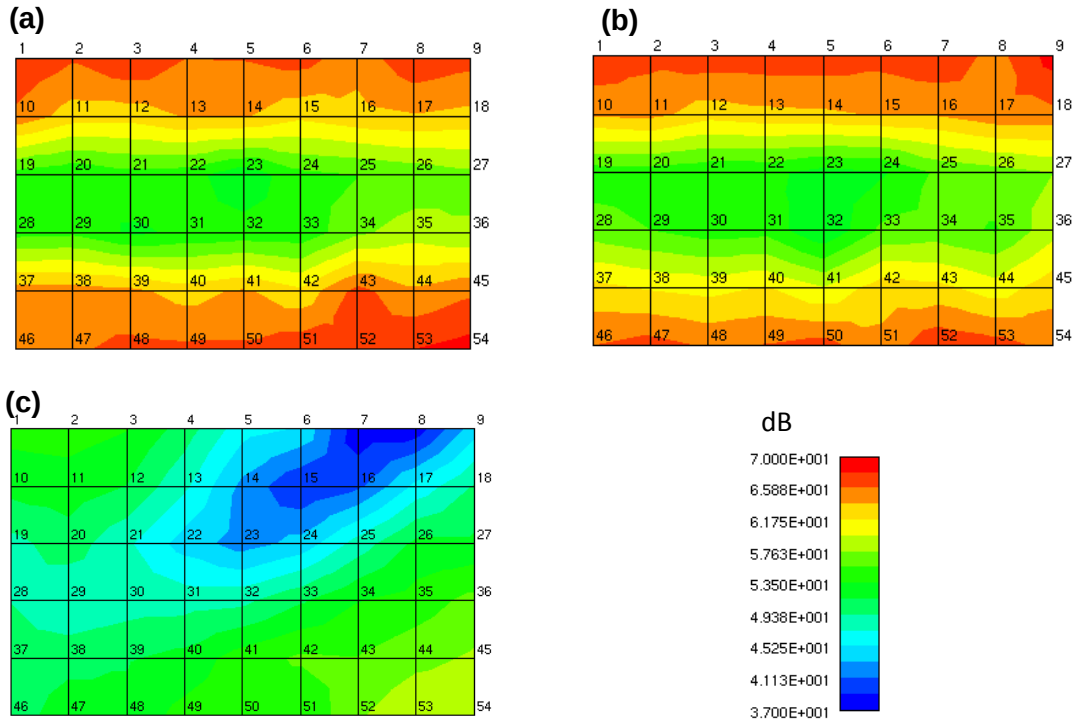

Figure 5.40 Measured Sound pressure contour map at 418 Hz, corresponding to *z* - axial mode (0, 0, 1). (a) untreated, (b) with MPP absorber, (c) MPP absorber with partitioning.

5.4.3 BEM Simulation of the MPP with Cavity Partitioning

Since the measurement was made on single plane, a BEM simulation was conducted in order to better understand the modal behavior inside of the duct. Simulations were conducted for the three cases mentioned earlier. The indirect BEM (Vlahopoulos, 2000) was used for each simulation. The MPP itself was modeled via a transfer impedance relationship. This transfer impedance was defined on the boundary elements representing the MPP.

The BEM mesh with MPP and partitioning is shown in Figure 5.41. The mesh consisted of 6532 nodes and 4845 elements. The partitioning was modeled as being square in cross-section instead of hexagonal due to ease of discretization. The cells were approximately 5.25 cm in length and height which was less than the acoustic wavelength for the maximum frequency of interest (34.3 cm). It was

assumed that the MPP, the partitioning, and the sides of the plenum were rigid. However, a small amount of absorption was added to the plenum cavity for each case by using a complex speed of sound with a small imaginary component as described in reference (Herrin, 2006).

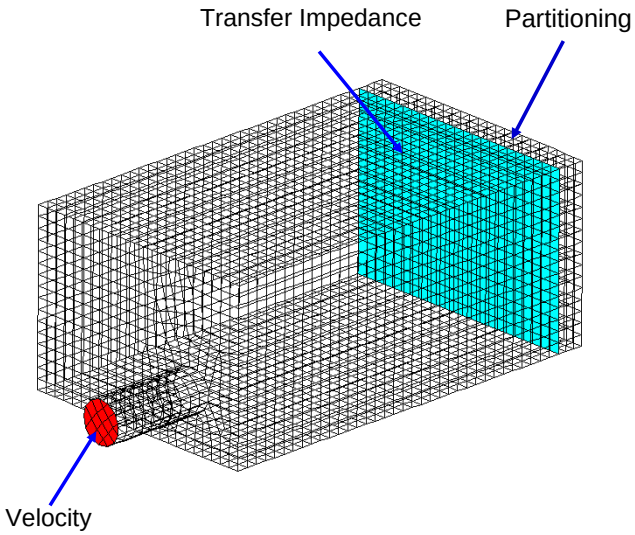

Figure 5.41 BEM mesh of Plenum with MPP and partitioning.

Figure 5.42 shows insertion loss for the MPP with partitioning. The measured results are compared to BEM simulation. Notice the good agreement in the results between 300 and 1000 Hz. In particular, the BEM simulation correctly predicts most of the peaks and nadirs in the insertion loss. Below 300 Hz, the simulation did not compare well.

This might partially be due to background noise since a bookshelf loudspeaker was used and it produces little sound power at low frequencies. Furthermore, the measurement results are questionable at low frequencies because it is not expected that the MPP would provide much attenuation below the first mode of the plenum since the measured absorption was quite low. It is also possible that the cardboard partitioning provides a small amount of absorption at low frequencies. Nevertheless, the good agreement above 300 Hz suggests that the model is realistic.

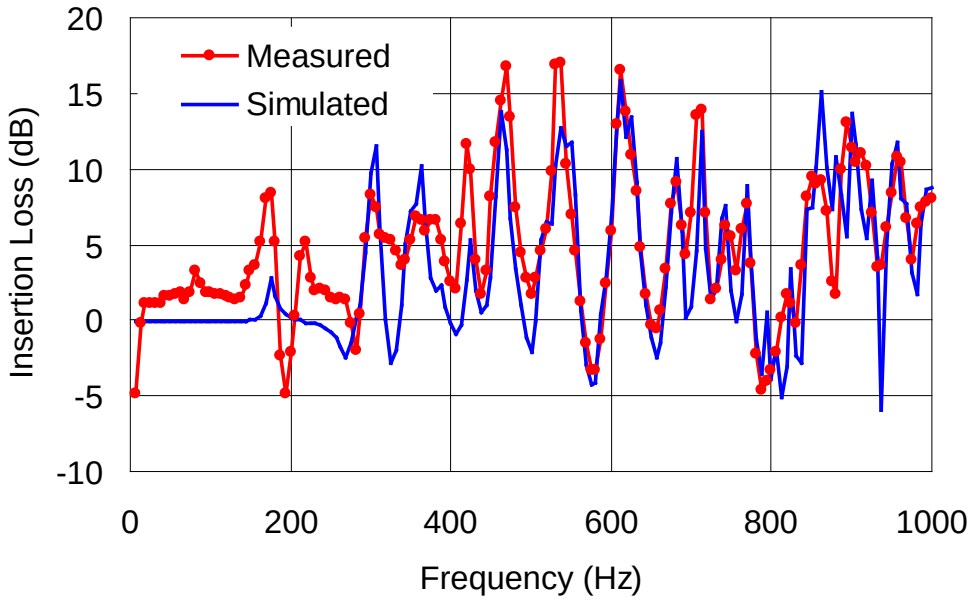

Figure 5.42 Insertion loss Comparison of MPP with Partitioning.

Notice the negative insertion loss in both the measurement and simulation at several frequencies. This is because the MPP adds damping to the cavity at both the resonances and anti-resonances. At the anti-resonances, this manifests itself as a negative insertion loss. In both simulation and the measurement, plenum resonant frequencies shifted little. The MPP and adjoining cavity may have little effect because the cavity depth (6.5 cm) is small compared to the dimensions of the plenum.

Figure 5.43 shows BEM sound pressure contour plots inside of the plenum. Several field point planes were constructed along the length of the plenum as indicated in the figure. Results are shown for the (0,1,0) mode.

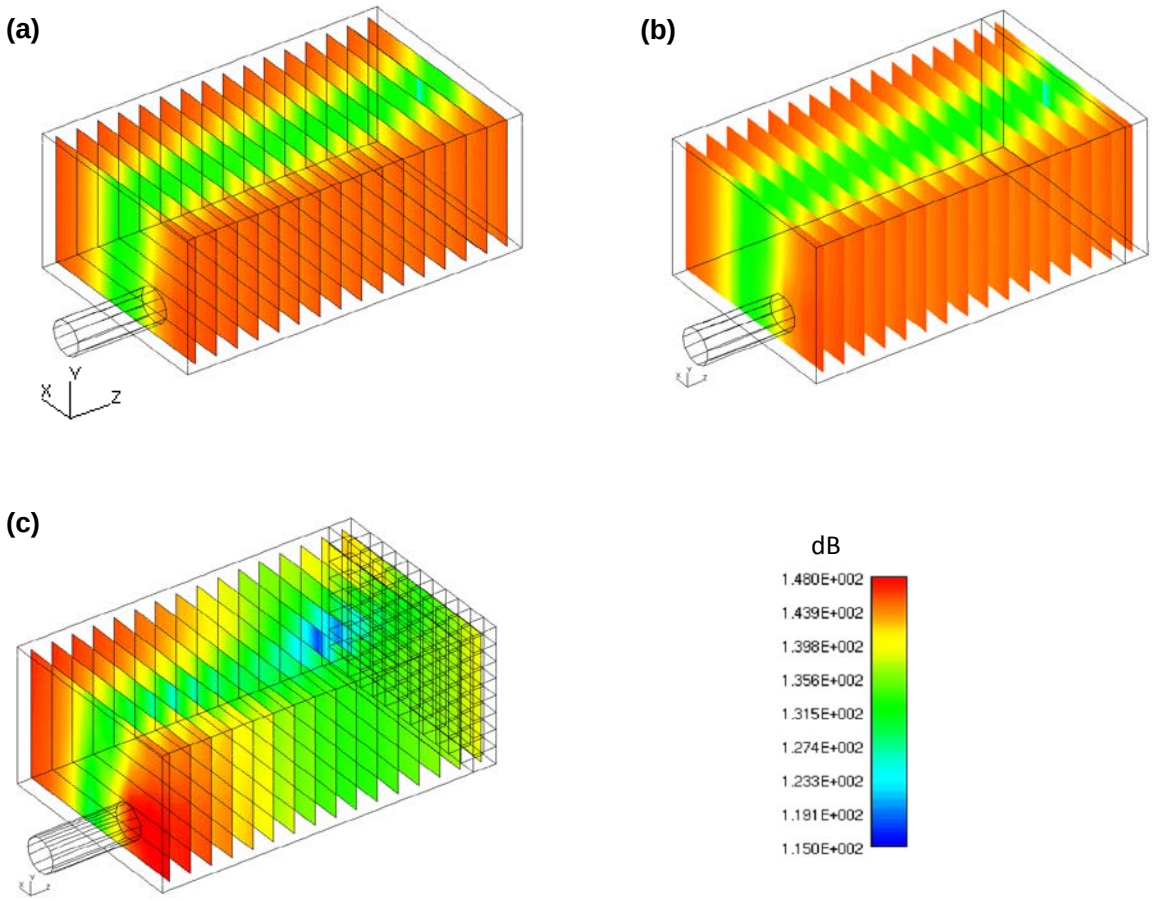

Figure 5.43 Simulated Sound pressure contour map at 294 Hz, corresponding to y - axial mode (0, 1, 0). (a) untreated, (b) with MPP absorber, (c) MPP absorber with partitioning.

Figures 5.43 (a) and (b) show the contour plots for the sound pressure for the untreated and MPP unpartitioned cases. Notice that the MPP has very little effect because the particle velocity in the direction normal to the MPP panel is quite low. This suggests that the pressure difference between sides of the panel will also be low. Figure 5.43(c) shows the sound pressure contour for the MPP with partitioning. The partitioning insures that the (0,1,0) mode behavior will not manifest itself behind the MPP. Furthermore, this leads to a higher particle velocity in the perforate resulting in energy dissipation or damping in the perforate. Notice that the sound pressure is low close to the MPP but the (0,1,0) mode is still present close to the source (further from the MPP).

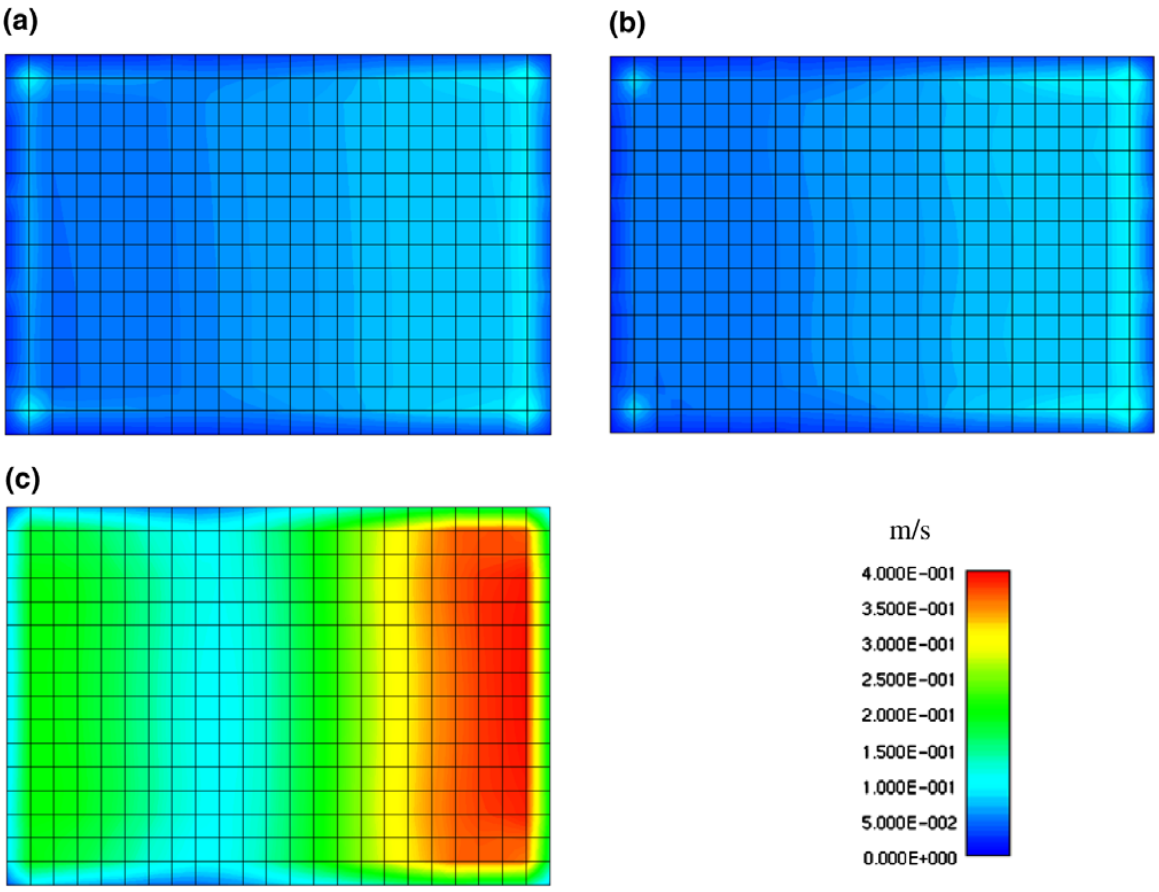

Figure 5.44. BEM simulated particle velocity (normal to the MPP) contour map at 294 Hz, corresponding to y-axial mode (0, 1, 0). (a) Untreated, (b) with MPP absorber, (c) MPP absorber with partitioning.

Figure 5.44 shows particle velocity (normal to the MPP) on a plane 25 cm anterior to the MPP. Note that particle velocity is not shown right on the BEM mesh since field point results for particle velocity is inaccurate when located on the BEM mesh itself. Nevertheless, 2.5 cm is much less than an acoustic wavelength at 295 Hz so the results shown should approximate the particle velocity at the MPP. Notice that the unpartitioned MPP (Figure 5.44 b) has very little effect because the particle velocity in the direction normal to the MPP panel is quite low (nearly the same as for the untreated case shown in Figure 5.44 a). This suggests that the pressure difference between sides of the panel is low. The partitioning insures that the (0,1,0) mode behavior will not manifest itself behind

the MPP. This leads to a higher particle velocity in the perforate (Figure 5.44c) resulting in greater energy dissipation or damping in the perforate.

As a summary, the effect of adding a partition in the back cavity of an MPP absorber has been investigated. The results indicate that partitioning improves the performance of the absorber by disrupting wave propagation behind the MPP that would be present without it. The effect is particularly noticeable at low frequencies where the acoustic response is resonant in nature. In that case, partitioning improved the MPP performance by over 8 dB for the example included in this paper. However, attenuation gains are more modest if the modes propagate perpendicular or oblique to the MPP absorber (less than 5 dB). Contour maps at a few frequencies of interest confirmed the hypothesis.

Additionally, a BEM analysis was conducted to simulate the effect of the MPP plus air cavity. Analyses were conducted with and without partitioning in the adjoining cavity. The simulation agreed well with experimental results when it was assumed that the MPP could be modeled via a transfer impedance boundary condition. The simulation illustrated that the MPP was most effective when the particle velocity (in the direction normal to the MPP) in the perforations was high.

CHAPTER 6
APPLICATION OF MOEBIUS TRANSFORMATION TO ACOUSTIC IMPEDANCES

The *Moebius transformation* maps straight lines or circles in one complex domain into straight lines or circles in another complex plane. This chapter will demonstrate that the acoustic response will trace a circle in the complex plane for straight line or circular modifications to mechanical or acoustical impedance. This is due to the fact that the equations relating the acoustic response to the modification are in a form consistent with the Moebius transformation. This is demonstrated for series and parallel mechanical and acoustic impedances. The principles for the case of mechanical impedance are in essence equivalent to what has been termed the *generalized Vincent circle*.

6.1 Moebius Transformation and its Properties

A Moebius transformation of one complex variable z is a mapping of the form

$$M(z) = \frac{az + b}{cz + d} \tag{6.1.1}$$

where a, b, c and d are complex constants and satisfy $ad\text{-}bc \neq 0$.

A Moebius transformation can be decomposed into a sequence of simple transformations, as shown below (Needham 1997).

$$\left.\begin{array}{ll} \text{(i)} & z \mapsto z + \dfrac{d}{c}, \text{ which is a translation;} \\ \text{(ii)} & z \mapsto (1/z), \text{ which is a complex inversion;} \\ \text{(iii)} & z \mapsto -\dfrac{ad - bc}{c^2} z, \text{ which is a dialation and a rotation;} \\ \text{(iv)} & z \mapsto z + \dfrac{a}{c}, \text{ which is another translation.} \end{array}\right\} \tag{6.1.2}$$

Of the four transformations above, the complex inversion mapping holds the key to understanding the transformation. The image of $z = re^{i\theta}$ under complex inversion is $(1/r)e^{-i\theta}$: the new length is the reciprocal of the original, and the new angle is the negative of the original. A point outside the unit circle C is mapped to a point inside C, and vice versa, as shown in Figure 6.1.

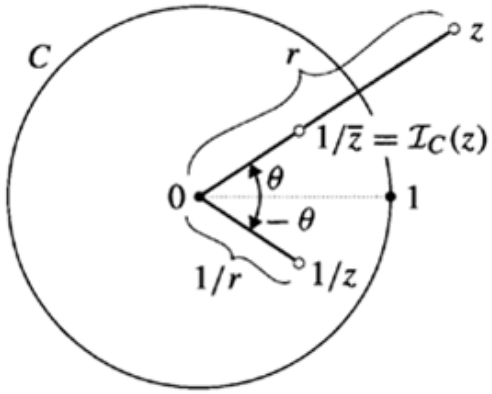

Figure 6.1 Illustration of complex inversion for a single point (Needham 1997).

One special property of a complex inversion is the preservation of generalized circles. A generalized circle is either a circle or a line, the latter being considered as a circle through the point at infinity. This property can be stated in the following manner. If a line L does not pass through the center q of unit circle K, the inversion in K maps L to a circle that passes through center q. This property is illustrated in Figure 6.2.

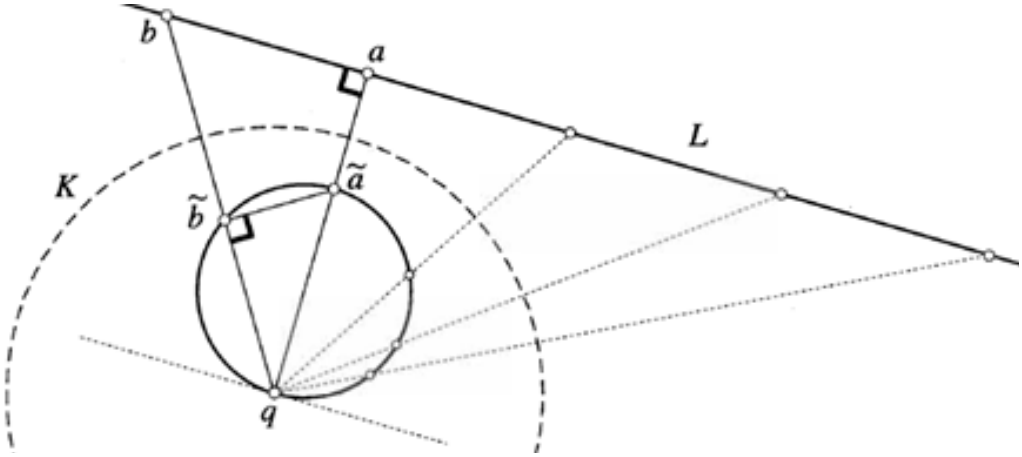

Figure 6.2 Illustration of preservation of generalized circle (Needham 1997).

Note that a Moebius transformation does not necessarily map lines to circles; it can also map lines to lines or circles to circles.

6.2 Review of Vincent Circle and its Application

6.2.1 The Vincent Circle

Discovered by A. H. Vincent of Westland Helicopters in 1972, it was apparently overlooked in the intervening years until a recent paper by Tehrani et al (2006). Vincent limited his scope to structures excited at a single point and assumed a stiffness modification between two positions on a structure. Tehrani et al (2006) made an important contribution by discovering that the principle could be generalized to a dynamic stiffness modification in one dimension thereby incorporating mass and damping modifications.

The development of the method that follows is similar to that shown by Done and Hughes (1975) over 30 years ago. Figure 6.3 shows a schematic of a structure with a modification (in this case a spring) between points r and s. The structure is excited at a point p and the response will be computed at a point q. Done and Hughes supposed that point q was on the structure and the response was a structural vibration. However, the derivation shown herein will assume a structural force at point p and an acoustic response at a point q. Whether the excitation or the response is structural or acoustic has little bearing on the applicability of the principle. It will be shown later that the modification need not be structural. Assuming acoustic plane waves, a modification to the admittance is equally valid. However, the modification should be one-dimensional whether structural or acoustic.

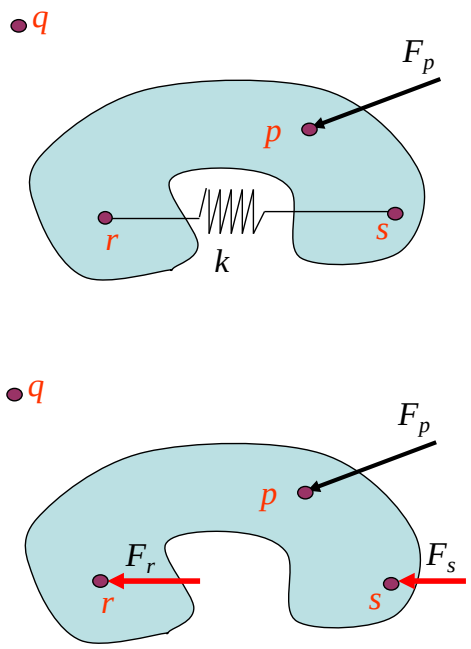

Figure 6.3 Schematic to illustrate the development of the Vincent Circle principle.

Assume that the spring is replaced by two forces F_r and F_s. In that case, the vibrational responses at points r and s, and the acoustic response at point q can be written in terms of the applied forces F_p, F_r, and F_s. Thus,

$$p_q = H_{qp}F_p + H_{qr}F_r + H_{qs}F_s \tag{6.2.1a}$$

$$x_r = H_{rp}F_p + H_{rr}F_r + H_{rs}F_s \tag{6.2.1b}$$

$$x_s = H_{sp}F_p + H_{sr}F_r + H_{ss}F_s \tag{6.2.1c}$$

where H_{ij} are the unmodified transfer functions between the vibration or acoustic responses at point i and the forces or inputs at point j.

Note that the forces F_r and F_s can be expressed in terms of the spring stiffness k and the displacement responses x_r and x_s as

$$F_r = k(x_s - x_r) = -F_s \tag{6.2.2}$$

and then substituted into Equation 6.2.1. This results in a set of 3 simultaneous equations with 3 unknown responses x_r, x_s, and p_q. Solving for the modified transfer function (p_q/F_p), the following expression is obtained

$$\frac{p_q}{F_p} = H_{qp} + \frac{k\left(H_{sp} - H_{rp}\right)\left(H_{qr} - H_{qs}\right)}{1 + k\left(H_{rr} + H_{ss} - H_{rs} - H_{sr}\right)} \tag{6.2.3}$$

Tehrani et al (2006) observed that Equation 6.2.3 is a particular case of the Moebius Transformation. It is recommended that the reader consult the aforementioned paper by Tehrani et al (2006) for a more complete discussion of the Moebius Transformation.

What is most relevant to this discussion is that Equation 6.2.3 can be written in the form

$$a = b + \frac{Dc}{1 + Dd} \tag{6.2.4}$$

Where a, b, c, and d are complex numbers defined as

$$a = \frac{p_q}{F_p} \tag{6.2.5a}$$

$$b = H_{qp} \tag{6.2.5b}$$

$$c = \left(H_{sp} - H_{rp}\right)\left(H_{qr} - H_{qs}\right) \tag{6.2.5c}$$

$$d = \left(H_{rr} + H_{ss} - H_{rs} - H_{sr}\right) \tag{6.2.5d}$$

And D is the modification (k in Equation 6.2.3). A characteristic of the Moebius Transformation is that the complex number a will trace a circle in the complex plane as a real or imaginary D varies from plus to minus infinity given that b, c, and d are complex numbers. For a real modification, Done and Hughes (1975) showed that the radius ρ and center ξ of this circle can be expressed as

$$\rho = \left| \frac{c}{2\ \mathrm{imag}(d)} \right| \tag{6.2.6}$$

and

$$\xi = b - \frac{jc\rho}{|c|} \tag{6.2.7}$$

respectively. If D is purely imaginary (i.e. a viscous damper modification), the radius ρ and center ξ of this circle can be expressed as

$$\rho = \left| \frac{c}{2\,real(d)} \right| \tag{6.2.8}$$

and

$$\xi = b + \frac{c\rho}{|c|} \tag{6.2.9}$$

respectively. As mentioned previously, Tehrani et al (2006) noted that the modification D is a dynamic stiffness modification. Thus,

$$D = k - \omega^2 m + j\omega c_D \tag{6.2.10}$$

in which k, m and c_D are stiffness, mass and damping respectively.

The minimum value of a in Equation 6.2.4, which corresponds to the possible maximum suppression of the response, should be the point on the circle closest to the origin of the complex plane. Hence, the approach is ideal for selecting a passive control mechanism for minimizing noise at a particular frequency.

6.2.2 Application to Two Series or Parallel Impedances

It is also interesting to consider two separate cases where z_m is replaced by two impedances z_{m1} and z_{m2} in series or in parallel. Utilizing the equivalence of Equations 6.2.1 and 6.2.5 shown earlier, Equation 6.2.4 can be written in the form

$$\frac{p_q}{F_p} = \frac{\alpha_1 Z_M + \beta_1}{\gamma_1 Z_M + \delta_1} \tag{6.2.11}$$

where $\alpha_1, \beta_1, \gamma_1$ and δ_1 are complex constants. Now, if Z_M in Equation 6.2.11 is replaced by two impedances Z_{M1} and Z_{M2} placed in series so that

$$Z_M = \frac{Z_{M1} \cdot Z_{M2}}{Z_{M1} + Z_{M2}} \tag{6.2.12}$$

Equation 6.2.12 can be written in the form

$$\frac{p_q}{F_p} = \frac{\alpha_2 Z_M + \beta_2}{\gamma_2 Z_M + \delta_2} \tag{6.2.13}$$

where

$$\alpha_2 = \alpha_1 Z_{M2} + \beta_1 \tag{6.2.14a}$$

$$\beta_2 = \beta_1 Z_{M2} \tag{6.2.14b}$$

$$\gamma_2 = \gamma_1 Z_{M2} + \delta_1 \tag{6.2.14c}$$

$$\delta_2 = \delta_1 Z_{M2} \tag{6.2.14d}$$

Note that Equation 6.2.13 is in the form of the Moebius transformation shown in Equation 6.2.11. Thus, the transfer function relating p_q to F_p will trace a circle in the complex plane for straight line modifications in the complex plane to either Z_{M1} or Z_{M2}.

A similar expression can be developed for the case of impedances in parallel. Replace Z_M by two impedances Z_{M1} and Z_{M2} in parallel so that

$$Z_M = Z_{M1} + Z_{M2} \tag{6.2.15}$$

Equation 6.2.11 can be rewritten in the form of equation 6.2.13 where

$$\alpha_2 = \alpha_1 \tag{6.2.16a}$$

$$\beta_2 = \alpha_1 Z_{M1} + \beta_1 \tag{6.2.16b}$$

$$\gamma_2 = \gamma_1 \tag{6.2.16c}$$

$$\delta_2 = \gamma_1 Z_{M2} + \delta_1 \tag{6.2.16d}$$

Thus, modifying particular impedance in a combination of series and parallel impedances will map the response or transfer function relating p_q to F_p to a circle in the complex plane.

6.3 Application to Acoustic Impedance

The Moebius transformation may also be applied to acoustic impedance. This will be demonstrated using a development very similar to that for mechanical impedance. Referring to Figure 6.4, assume that a velocity source is applied (v_p) at point p and the response of interest is the pressure at point q (p_q). In this case, the modification is the acoustic admittance at position r (Y_r). This assumes plane wave behavior at positions r and p though not necessarily at q.

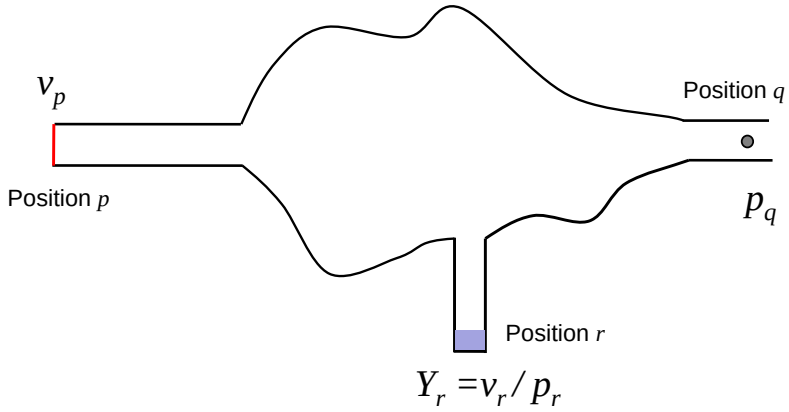

Figure 6.4 Schematic to illustrate the application of the Moebius transformation to acoustic impedance

The modified pressure at point q (p_q) can be expressed as

$$p_q = H_{qp} v_p + H_{qr} v_r \tag{6.3.1a}$$

$$p_r = H_{rp} v_p + H_{rr} v_r \tag{6.3.1b}$$

where H_{ij} are the unmodified transfer functions between the sound pressure responses at point i and the particle velocities point j. The particle velocity at position r (v_r) can be expressed in terms of the admittance as

$$v_r = Y_r p_r \ . \tag{6.3.2}$$

When the identity in Equation 6.2.20 is used in Equations 6.2.19a and 6.2.19b, one obtains

$$\frac{p_q}{v_p} = H_{qp} + \frac{Y_r H_{rp} H_{qr}}{1 - Y_r H_{rr}} \tag{6.3.3}$$

which once again has the same form as Equation 6.2.4. As noted earlier, modifications of the admittance Y_r or its reciprocal (the impedance Z_r) along a line or circle in the complex plane will map circles in the complex plane for $p_q v_p$.

Additionally, the Moebius transformation can be proven to be applicable to both series and parallel acoustic impedances using the identical analysis in Equations 6.2.11 to 6.16. In duct acoustics, series and parallel acoustic impedances are commonly denoted as transfer (used for modeling perforates) and branch (used for modeling side branches) impedances.

Fahy (2001) noted that the specific acoustic impedances at positions (shown in Figure 6.5) upstream (z_1) and downstream (z_2) could be related to one another via the expression

$$z_1 = \frac{z_2 + j \tan(kL)}{j \tan(kL) z_2 + 1} \tag{6.3.4}$$

where k is the acoustic wavenumber and L is the distance separating positions 1 and 2. Plane wave propagation of sound is assumed in the duct. Note that the expression is already in the form of the Moebius transformation for both modifications of $\tan(kL)$ and z_2. Fahy previously demonstrated that z_1 traces a circle in the complex plane as $\tan(kL)$ varies from minus to plus infinity though not by utilizing the Moebius transformation. Similarly, it is apparent that if z_2 is modified along a straight line or circle, z_1 will similarly trace a circle in the complex plane according to the Moebius transformation.

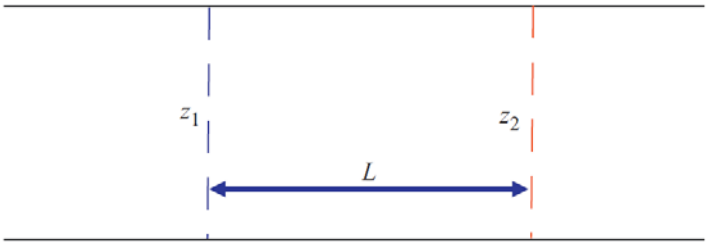

Figure 6.5 Schematic showing impedance at two locations in a duct separated by length L.

6.4 Application to Duct Systems

A separate development is shown for the special cases of acoustic impedances in duct systems. This development is based on the transfer matrix methodology summarized by Munjal (1987). At lower frequencies, the duct cross-sectional dimensions are small compared to the acoustic wavelength. Accordingly, it can be assumed that plane waves propagate inside the duct system simplifying the analysis. In this case, a duct system can be described as an acoustic network using the well known transfer matrix. The transfer matrix is composed of four-pole parameters A, B, C, and D is defined according to the matrix equation

$$\begin{Bmatrix} p_1 \\ \rho_0 S_1 v_1 \end{Bmatrix} = \begin{bmatrix} A & B \\ C & D \end{bmatrix} \begin{Bmatrix} p_2 \\ \rho_0 S_2 v_2 \end{Bmatrix} \tag{6.4.1}$$

where p_1 and p_2 are sound pressures and v_1 and v_2 are particle velocities.

The four-pole parameters for certain components like rigid-walled straight pipes or ducts are well-known (Munjal, 1987). However, numerical or experimental methods must be used to determine the four-pole parameters of more sophisticated components like large expansion chambers and elbows.

Figure 6.6 shows a duct system including the source (Z_S) and termination impedance (Z_T). A_T, B_T, C_T, and D_T are the overall four-pole parameters including the effect of the inlet and outlet pipes.

The source pressure p_S can be related the load pressure p_L via

$$p_S = p_L\left(1+\frac{Z_S}{Z_L}\right) \tag{6.4.2}$$

where Z_S and Z_L are the source and load impedances respectively. In turn, the load and termination impedances can be expressed as

$$Z_L = \frac{p_2}{\rho_2 S_2 v_2} \tag{6.4.3}$$

and

$$Z_T = \frac{p_1}{\rho_1 S_1 v_1}\ . \tag{6.4.4}$$

By inserting Equations 6.4.3 and 6.4.4 into Equation 6.4.2, the pressure at the termination (p_T which is identical to p_1) can be expressed as

$$p_T = \frac{p_S Z_T}{A_T Z_T + B_T + C_T Z_S Z_T + D_T Z_S} \tag{6.4.5}$$

where p_S is the source pressure. Note that Equation 6.4.5 is already in the form of the Moebius transformation (Equation 6.2.11) for modifications to either source or termination impedance. If the modification is for source impedance, the complex constants identified in Equation 6.2.11 can be expressed as

$$Z = \frac{p_T}{p_S} \tag{6.4.6a}$$

$$\alpha = 0 \tag{6.4.6b}$$

$$\beta = Z_T \tag{6.4.6c}$$

$$\gamma = C_T Z_T + D_T \tag{6.4.6d}$$

$$\delta = A_T Z_T + B_T\ . \tag{6.4.6e}$$

Similarly, if the termination impedance is modified, the complex constants can be expressed as

$$Z = \frac{p_T}{p_S} \tag{6.4.7a}$$

$$\alpha = 1 \tag{6.4.7b}$$

$$\beta = 0 \tag{6.4.7c}$$

$$\gamma = A_T + C_T Z_S \tag{6.4.7d}$$

$$\delta = B_T + D_T Z_S\ . \tag{6.4.7e}$$

Furthermore, the Moebius transformation is also directly applicable to a series or branch impedance inserted into a duct system as shown in Figure 6.6. In that case the pressure and particle velocity on the inlet side (indicated by the subscript 1) of the panel can be related to that at the outlet (indicated by the subscript 2) by

$$\begin{Bmatrix} p_1 \\ \rho_0 S_1 v_1 \end{Bmatrix} = \begin{bmatrix} 1 & Z_{tr} \\ 0 & 1 \end{bmatrix} \begin{Bmatrix} p_2 \\ \rho_0 S_2 v_2 \end{Bmatrix} \tag{6.4.8}$$

where Z_{tr} is the transfer impedance.

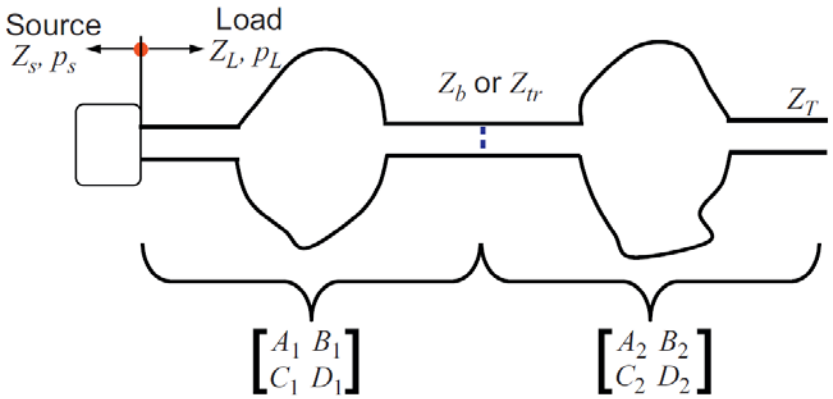

Figure 6.6 Schematic showing a parallel (z_b) or series (z_{tr}) impedance inserted into an acoustic system.

The four pole parameters for the duct work to the left of the transfer impedance are given as A_1, B_1, C_1, and D_1 and to right of the transfer impedance as A_2, B_2, C_2, and D_2. By determining the overall transfer matrix by multiplying the transfer matrices together and then inserting into Equation 6.4.5, the transfer function relating p_T to p_S can be expressed in the form of the Moebius transformation (Equation 6.2.11) with

$$Z = \frac{p_T}{p_S} \tag{6.4.9a}$$

$$\alpha = 0 \tag{6.4.9b}$$

$$\beta = Z_T \tag{6.4.9c}$$

$$\gamma = A_1 C_2 Z_T + A_1 D_2 + C_1 C_2 Z_s Z_T + C_1 D_2 Z_s \quad (6.4.9d)$$

$$\gamma = (A_1 A_2 + B_1 C_2) Z_T + (A_1 B_2 + B_1 D_2) + (C_1 A_2 + C_2 D_1) Z_S Z_T + (C_1 B_2 + D_1 D_2) Z_S \quad (6.4.9e)$$

The Moebius transformation is also directly applicable to a side branch with impedance Z_B inserted into a duct system as shown in Figure 6.6. In this case, the four pole parameters describing the relationship between the inlet and outlet sides of the side branch can be expressed as

$$\begin{Bmatrix} p_1 \\ \rho_0 S_1 v_1 \end{Bmatrix} = \begin{bmatrix} 1 & 0 \\ Z_B & 1 \end{bmatrix} \begin{Bmatrix} p_2 \\ \rho_0 S_2 v_2 \end{Bmatrix}. \quad (6.4.10)$$

By calculating the overall four-pole parameters and then inserting into Equation 6.4.5, the resulting transfer function relating p_T to p_S can be expressed in the form of the Moebius transformation (Equation 6.2.11) with

$$Z = \frac{p_T}{p_S} \quad (6.4.11a)$$

$$\alpha = Z_T \quad (6.4.11b)$$

$$\beta = 0 \quad (6.4.11c)$$

$$\gamma = (A_1 A_2 + B_1 C_2) Z_T + (A_1 B_2 + B_1 D_2) + (C_1 A_2 + C_2 D_1) Z_S Z_T + (C_1 B_2 + D_1 D_2) Z_S \quad (6.4.11d)$$

$$\delta = A_2 B_1 Z_T + B_1 B_2 + A_2 D_1 Z_S Z_T + B_2 D_1 Z_S . \quad (6.4.11e)$$

The application of the Moebius transformation is demonstrated on the duct system shown in Figure 6.7. Dimensions are shown in the figure. The duct system consists of source, termination, transfer, and branch impedances. The fluid was assumed to be aire with characteristic impedance of 415 Rayls. Plane wave behavior was assumed and all responses were computed making use of transfer matrix theory. All analysis was conducted at 1000 Hz.

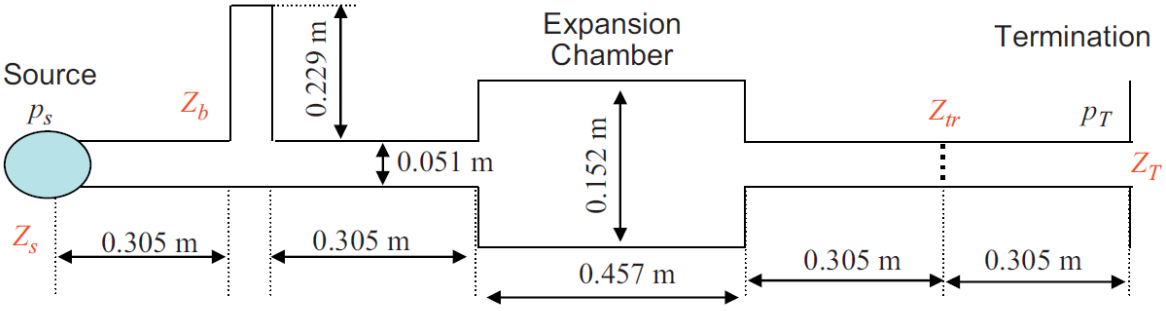

Figure 6.7 Duct system including dimensions utilized for demonstration of Moebius transformation.

6.4.1 Source Impedance Modification

The initial value for source impedance is defined as $\rho c(1-i)/\sqrt{2}$, based on Munjal's empirical equations (Munjal 2008). The transfer function between source strength (Ps) and radiated pressure (Pt) is simulated for a source impedance modification. Figure 6.8 shows the variation of real and imaginary parts of transfer function with respect to the variation of the real part of source impedance. On the right side of the figure, the projection of transfer function is plotted as '+' on the complex plane. The real part of the source impedance was modified from -20 to 20 while the imaginary part was held constant. Notice that the projection of transfer function between Pt and Ps on a complex plane traces a circle. A similar plot is shown in Figure 6.9 for a modification to the imaginary part of the source impedance.

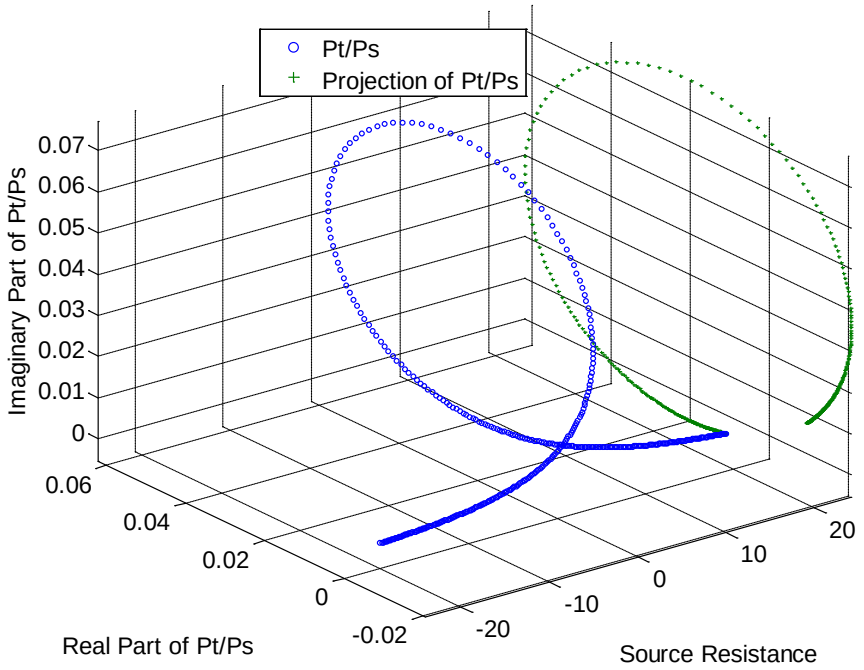

Figure 6.8 Transfer function between Pt and Ps plotted for a modification to source resistance.

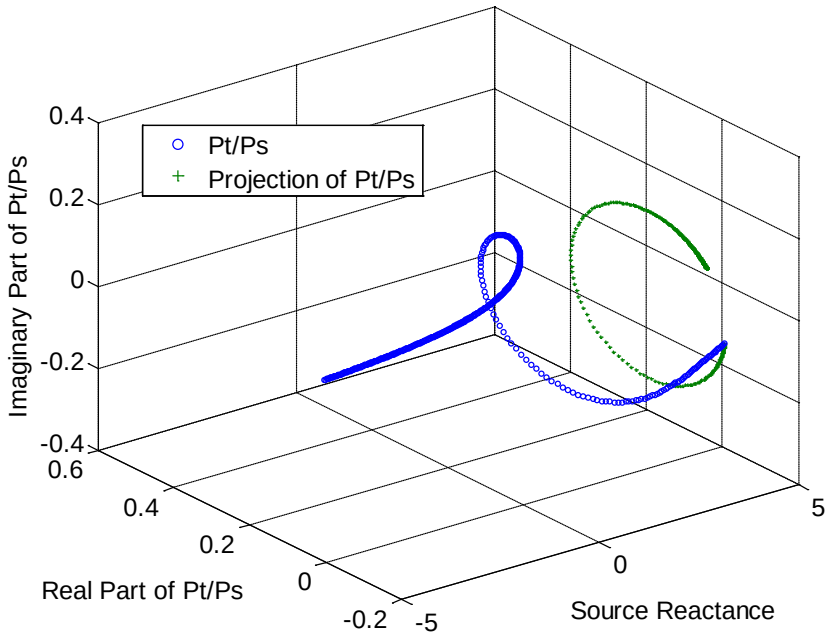

Figure 6.9 Transfer function between Pt and Ps plotted for a modification to source reactance.

6.4.2 Parallel Impedance Modification

An example of a parallel impedance is a closed side branch (i.e. quarter wave tube). The specific acoustic impedance can be expressed as

$$z_b = -i\rho c \cot(kL) \tag{6.4.12}$$

where L is the length of the close side branch.

The transfer function between the source strength (Ps) and radiated pressure (Pt) is simulated for a side branch modification. The diameter of the side branch is 2 inches and the initial length of the side branch is 9 inches, and the length is varied from 0 to 15 inches. Figure 6.10 shows the variation of real and imaginary parts of transfer function with respect to the variation of the side branch length. Notice that the projection of the transfer function between Pt and Ps on a complex plane traces a circle.

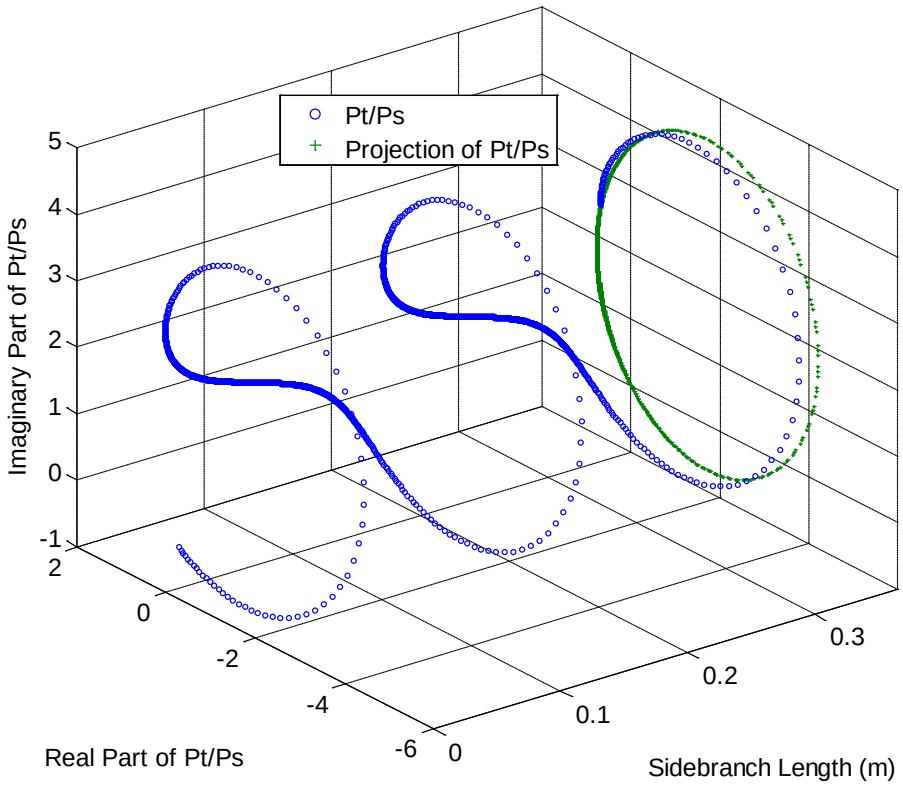

Figure 6.10 Transfer function between Pt and Ps plotted for a modification to side branch length.

6.4.3 Transfer Impedance Modification

The initial value for transfer impedance is defined as $\rho c(0.65+0.9i)$, based on measured transfer impedance of a MPP at 1000 Hz. The transfer function between source strength (Ps) and radiated pressure (Pt) is simulated for a transfer impedance modification. Figure 6.11 shows the variation of real and imaginary parts of transfer function with respect to the variation of the real part of transfer impedance. On the right side of the figure, the projection of the transfer function is plotted as '+' on the complex plane. The real part of the transfer impedance was modified from -20 to 20 while the imaginary part was held constant. Notice that the projection of the transfer function between Pt and Ps on a complex plane traces a circle. Figure 6.12 shows the variation of the transfer function for modification on imaginary part of the transfer impedance. Similar result was also obtained for imaginary part of transfer impedance.

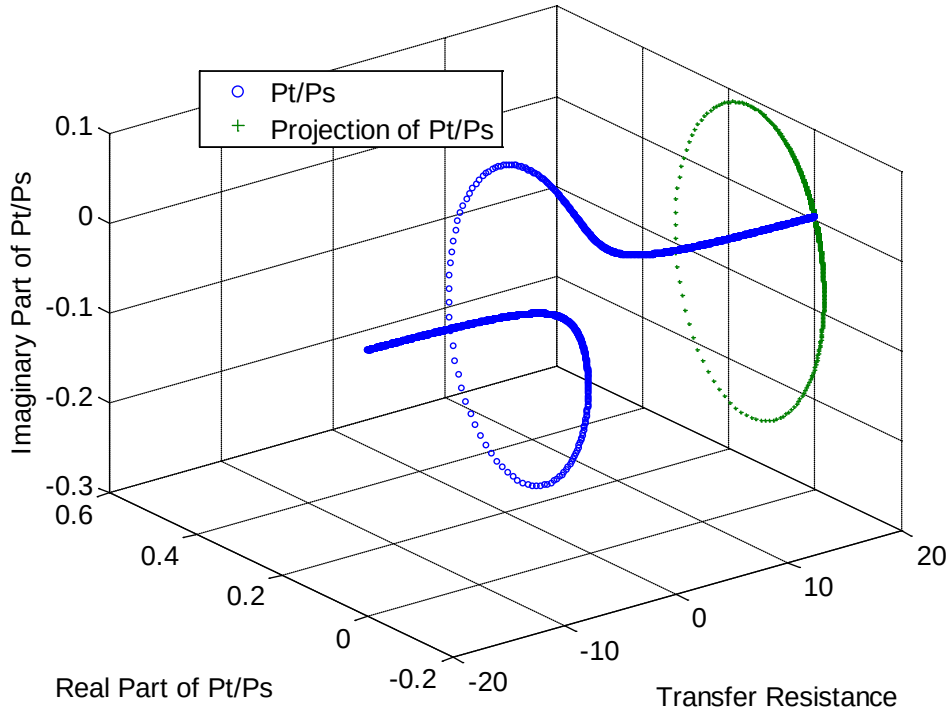

Figure 6.11 Transfer function between Pt and Ps plotted for a modification to transfer resistance.

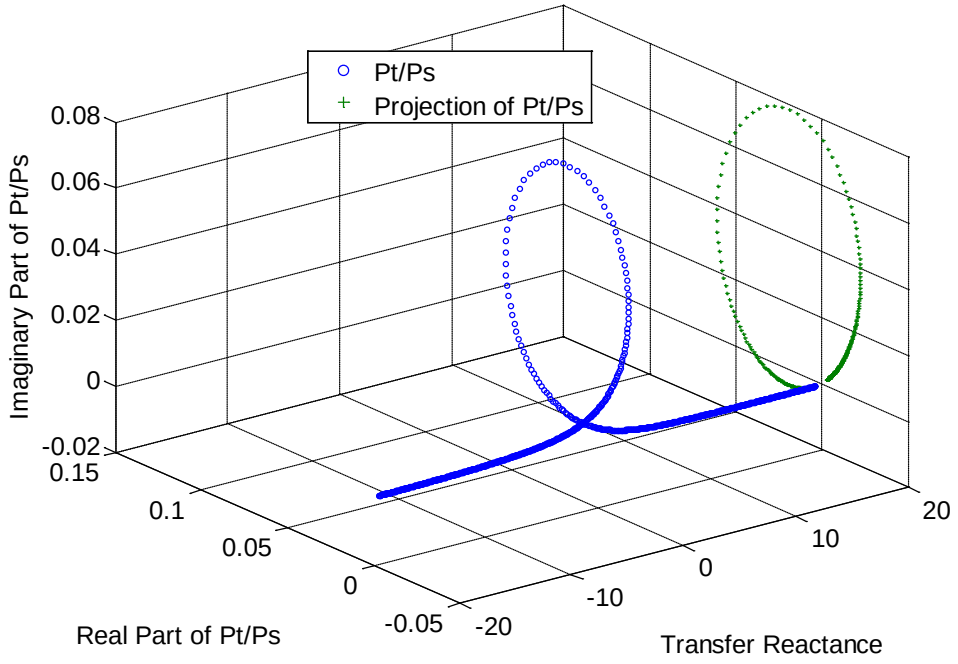

Figure 6.12 Transfer function between Pt and Ps plotted for a modification to transfer reactance.

6.4.4 Termination Impedance Modification

The initial value for termination impedance is defined as $\rho c(0.43+0.79i)$, based on the theoretical model for a flanged termination at 1000 Hz. The impedance of a flanged termination impedance can be expressed as

$$z_t = \frac{1}{2}(kr)^2 + i\frac{8}{3\pi}kr \tag{6.4.13}$$

where r is the radius of the duct (Kinsler, 1999).

The transfer function between source strength (Ps) and radiated pressure (Pt) is simulated for a termination impedance modification. Figure 6.13 shows the variation of real and imaginary parts of transfer function with respect to the variation of the real part of termination impedance. On the right side of the figure, the projection of transfer function is plotted as '+' on the complex plane. The real part of the termination impedance was modified from -20 to 20 while the imaginary part was held constant. Notice that the projection of transfer function

between Pt and Ps on a complex plane traces a circle. Figure 6.14 shows variations of transfer function for modification on imaginary part of termination impedance. Similar result was obtained for imaginary part of termination impedance.

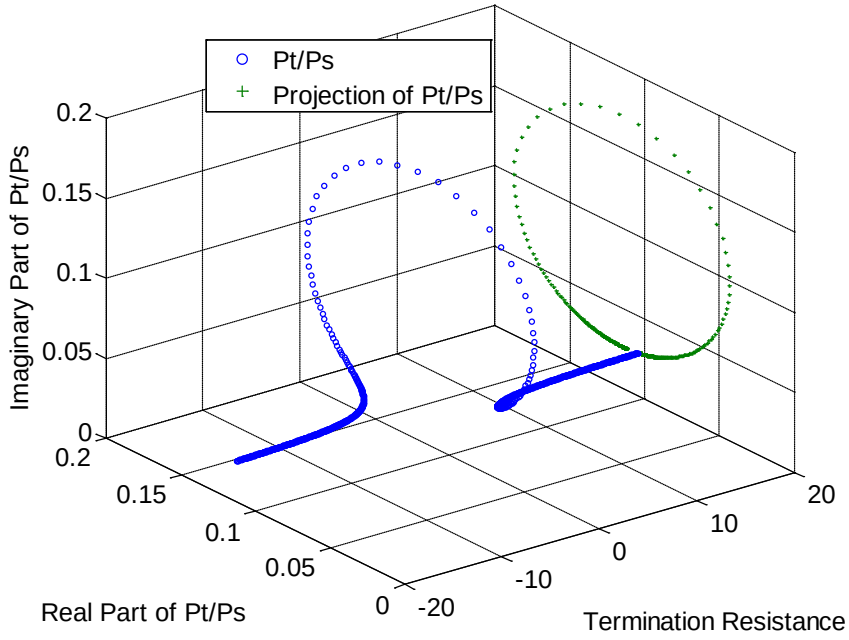

Figure 6.13 Transfer function between Pt and Ps plotted for a modification to termination resistance.

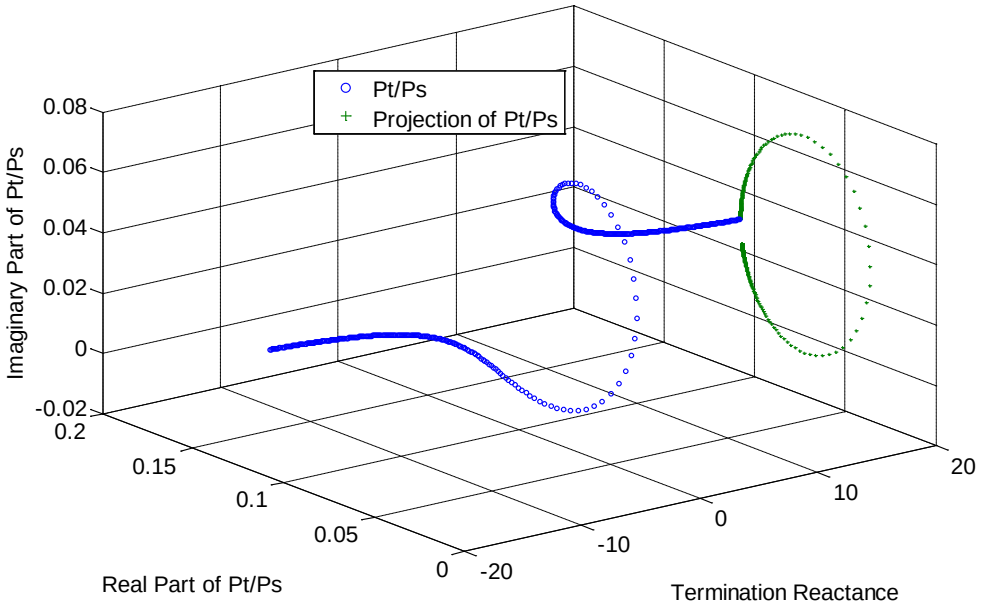

Figure 6.14 Transfer function between Pt and Ps plotted for a modification to termination reactance.

The previous simulation is done by modifying one part of the complex number while holding the other part constant. In real applications, both real and imaginary parts of impedance will change simultaneously. In order to study the effect of modifying both parts of a impedance, a more general form of Moebius transformation is investigated. In this case, both real and imaginary parts of the termination impedance were modified from -20 to 20.The transfer function between source strength (Ps) and radiated pressure (Pt) is simulated for this termination impedance modification. Each termination impedance in the plane shown in Figure 6.15 (a) was transformed into a transfer function in Figure 6.15 (b). This particular shape of transfer function in Figure 6.18 (b) is a result of complex inversion. In the short animation Arnold (2007) created to explain the Moebius transformation, he explained that the complex inversion turns the square plane inside out. This effect is illustrated by a sequence of animations shown in Figure 6.16. Figure 6.17 shows the variation of real and imaginary parts of transfer function with respect to the variation of the imaginary part of termination impedance.

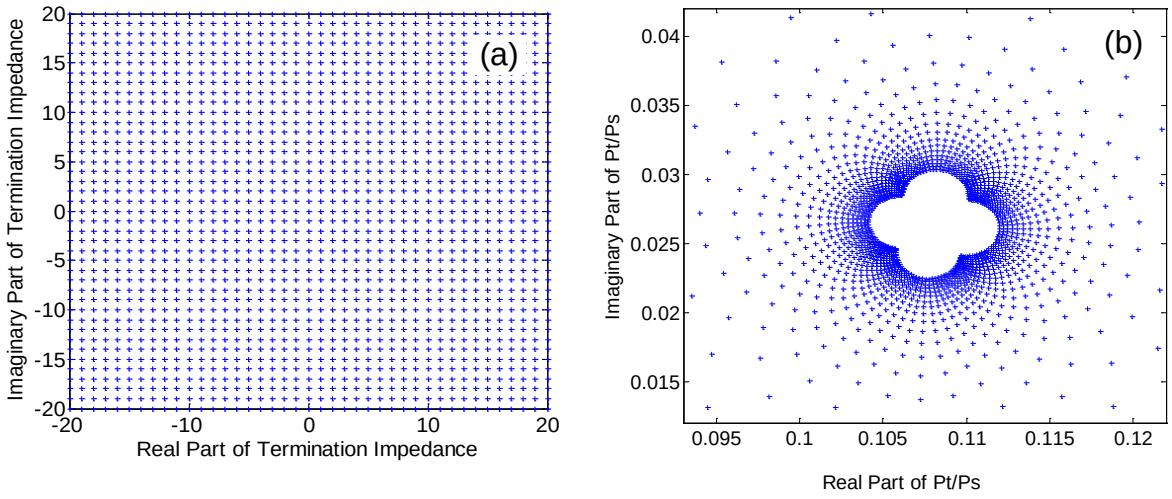

Figure 6.15 Termination impedances (a) were transformed into a transfer functions (b).

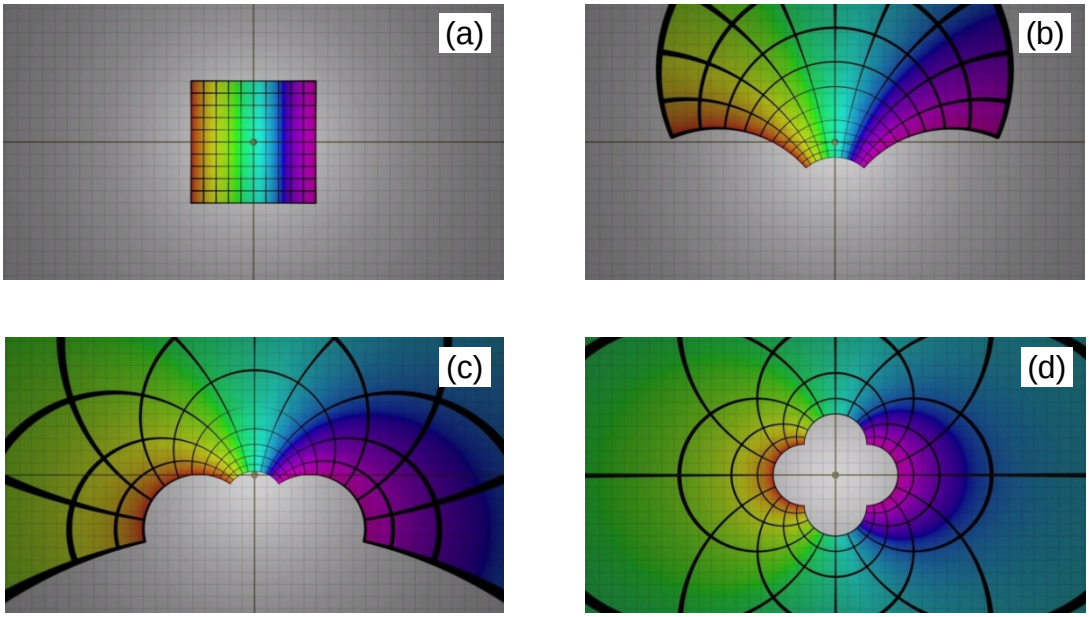

Figure 6.16 The sequence showing that complex inversion turns a square plane inside out (Arnold, 2007).

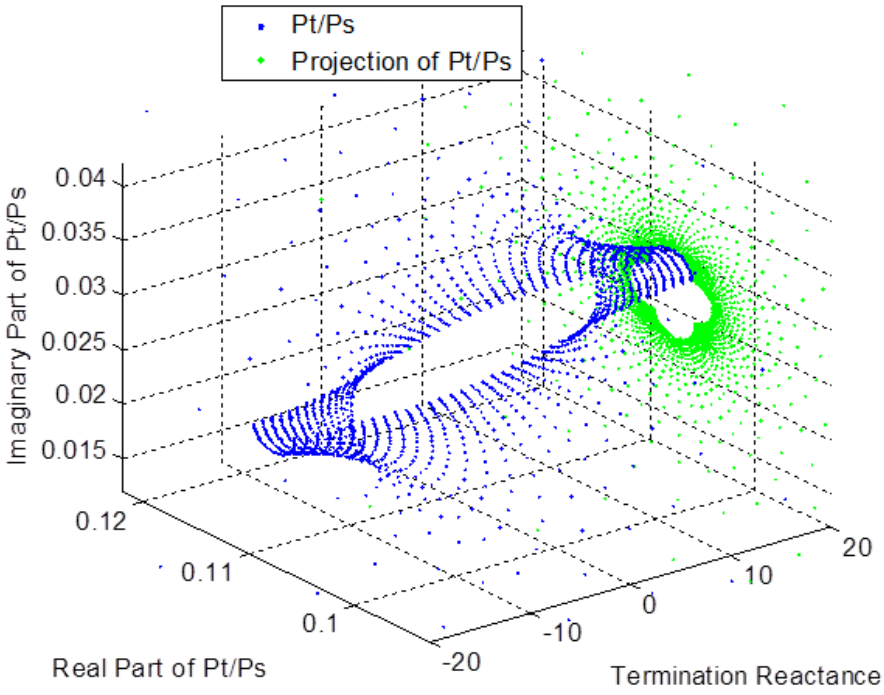

Figure 6.17 Transfer function between Pt and Ps plotted for a modification to both real and imaginary parts of termination impedance.

6.4.5 Expansion Chamber Length Modification

The transfer matrix of an expansion chamber can be expressed as

$$T = \begin{bmatrix} \cos(kL) & \frac{i \cdot \rho c}{m} \sin(kL) \\ \frac{i \cdot m}{\rho c} \sin(kL) & \cos(kL) \end{bmatrix} \tag{6.4.14}$$

where L is the length of the chamber and m is the area ratio. Modification to the length will change the four poles by changing sin(kL) and cos(kL). The transfer function between source strength (Ps) and radiated pressure (Pt) is simulated for an expansion chamber length modification. The diameter of the chamber is 6 inches and the initial length of the chamber is 18 inches. Then the length is varied from 0 to 22 inches. Figure 6.18 shows the variation of real and imaginary parts of transfer function with respect to the variation of the chamber length. Notice that the projection of transfer function between Pt and Ps on a complex plane does not trace a circle, but instead traces a curve called “an elliptic lemniscate of Booth” and it is the image of an ellipse under inversion with respect to its center (Coffman, 2006).

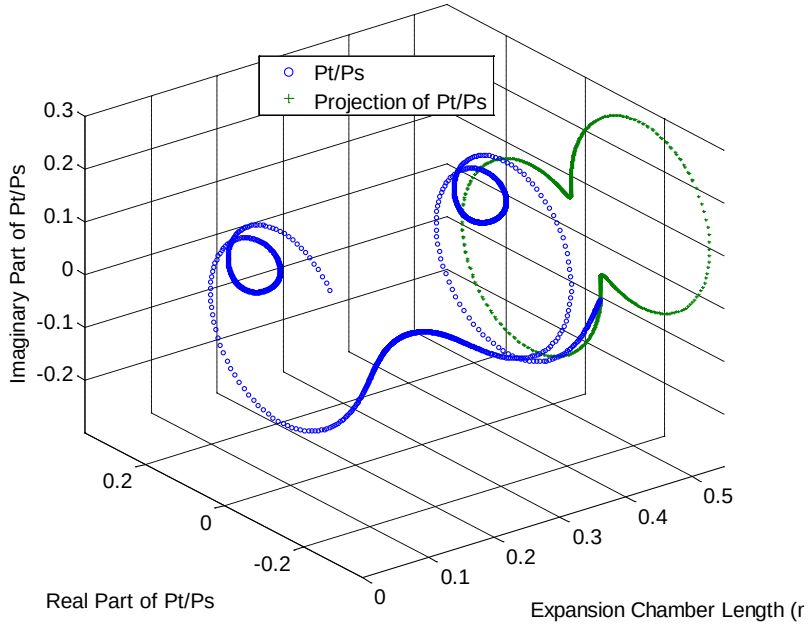

Figure 6.18 Transfer function between Pt and Ps plotted for a modification to expansion chamber length.

In order to explain the effect of modifying the chamber length, the simplest form of the duct system was constructed. Source and termination impedances are directly attached to the inlet and outlet of the simple expansion chamber. Substituting Equation 6.4.14 to Equation 6.4.5 yields:

$$\frac{p_t}{p_s} = \frac{Z_T}{\left(Z_T + Z_S\right)\cdot\cos\left(kL\right) + \left(\frac{i\cdot\rho c}{m} + Z_T Z_S \frac{i\cdot m}{\rho c}\right)\cdot\sin\left(kL\right)} \tag{6.4.15}$$

Modifying chamber length will change four poles simultaneously, which can be viewed as a combination of $\sin(kL)$ and $\cos(kL)$. Therefore, the variable for Moebius transformation in Equation 6.4.15 is

$$z = \alpha\cos\left(kL\right) + \beta\sin\left(kL\right) \tag{6.4.16}$$

where α and β are

$$\alpha = Z_T + Z_S \tag{6.4.17a}$$

$$\beta = \frac{i\cdot\rho c}{m} + Z_T Z_S \frac{i\cdot m}{\rho c} \tag{6.4.17b}$$

In this case, the complex constants of Moebius transformation as shown in Equation 6.1.1 are:

$$a = 0;\ \ b = Z_T;\ \ c = 1;\ \ d = 0 \tag{6.4.18}$$

Variable z is essentially an elliptic function of kL, as shown in blue in Figure 6.19. The complex inversion of z is shown in green. This plot explains the reason of transfer function tracing an elliptic lemniscate of Booth with chamber length variation.

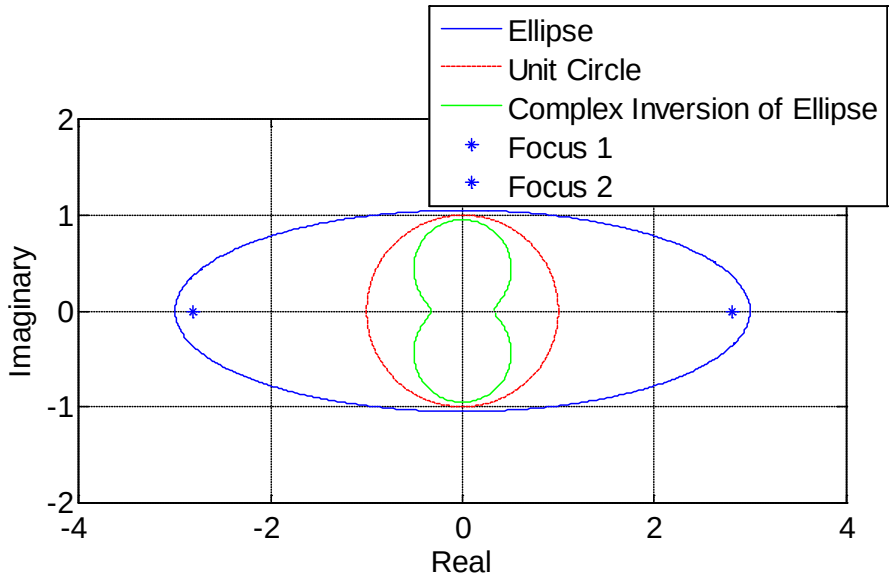

Figure 6.19 Complex conversion of an ellipse is an elliptic lemniscate of Booth.

6.5 Summary

It has been demonstrated that the Moebius transformation – which maps straight lines and circles in one complex domain to circles in another complex domain – is a mathematical tool that can be employed to aid in determining and understanding the impact of mechanical and acoustic impedance modifications on a vibro-acoustic system. The Moebius transformation is applicable to both series and parallel impedance modifications. This was shown to be especially enlightening for understanding the impact of impedance modifications to the response in waveguides. Acoustic impedance modifications in ducts are more easily controlled than mechanical impedances. As was previously noted, the method is amenable to any parallel or series impedance modification. For the case of a side branch, the impedance can be most easily adjusted by adjusting the length. Modifications in series impedances like source, transfer and termination impedances are also simulated to demonstrate the Moebius transformation.

One potential application is to select the impedance utilizing the Moebius transformation such that the acoustic response is optimized. However, the application is limited to analysis in single frequency and in a single degree of freedom.

CHAPTER 7
CONCLUSIONS AND RECOMMENDATIONS

In 1-Dimensional acoustic waveguides where the wavelength of the wave is much greater than the cross-sectional dimensions of the duct, the wave motion is quite analogous to the flow of electric current in a transmission line. One can make use of the well-established electrical circuit representation for acoustic elements because of the complete analogies between electrical system variables and acoustical ones. The analogy is very useful in understanding behavior of combinations of acoustic elements. This is made possible by studying combinations of their impedances. In 1-D acoustic waveguides, lumped acoustic impedance can be used to model geometric discontinuities, acoustic elements, etc. Based on electro-acoustic analogy, the combinations of lumped acoustic elements can be represented by either parallel impedances or series impedances. When modeled as parallel impedances, the acoustic elements share the same sound pressure at the junction. Meanwhile, when modeled as series impedances, the acoustic elements share the same particle velocity at the junction. Therefore, the combined admittance for parallel impedances equals the sum of the admittances of acoustic elements; while the combined impedance for series impedance equals the sum of the impedances of acoustic elements. In 1-D waveguides, example of parallel impedances is the combination of a Helmholtz resonator and its upstream and downstream elements; example of series impedances is the combination of a perforated plate and its upstream and downstream elements.

The research of this dissertation is focused on two types of series impedances, namely source impedance and transfer impedance. By utilizing their common characteristics as series impedances, the current research attempted to investigate source and transfer impedances under one category. The wave decomposition approach was applied to measure both source and transfer impedances. The Moebius transformation was used to investigate the influence of modifications of both source and transfer impedances on the system response.

The primary contributions and recommendations for future research for each topic of series impedance will be summarized.

7.1 Source Impedance

Source impedance, together with source strength, is used to characterize the acoustic sources connected to 1-D waveguides. Examples include the engine intake and exhaust, air moving devices in HVAC ducts, and pumps in hydraulic systems, etc. Source impedance can be modeled as internal impedance using a circuit analogy concept. Based on the circuit analogy, measurement methods such as the two-load method (Kathuriya, 1979) were developed and applied to measure the source impedance.

In the current research, an incident wave decomposition method for measuring source impedance and source strength was developed. This method was purely based on acoustic concepts instead of the equivalent circuit analogy. Compared to the source strength defined using the circuit analogy concept, which has no physical meaning, the outgoing source strength measured using this method represents a real acoustic component in a duct system, i.e. the acoustic source strength with an anechoic termination. The incident wave decomposition method was validated theoretically and experimentally.

The load effect based on condition number analysis was conducted for load combinations using different duct lengths. The study shows that, for wave decomposition method, selecting different duct lengths to modify acoustic load has little effect on the frequency wide source impedance accuracy. However, duct lengths could be strategically selected so as to enhance measurement accuracy in particular frequency bands. Furthermore, error analysis for wave decomposition method was conducted both theoretically and numerically. Error analysis suggests that changing the termination configuration can improve measurement accuracy if the two terminations produce very different acoustic loads. If possible, near anechoic and open flange load combinations should

improve measurement accuracy reducing the possibility of negative source resistance.

Finally, measured source impedance, together with termination impedance, was applied to predict the insertion loss of a small engine muffler with good agreement with measured data.

It is suggested that further source impedance work could be focused on the combination of the acoustic reciprocity principle and the wave decomposition method. The reciprocity principle states that the transfer functions between a source and receiver are identical if their positions are interchanged (Fahy, 2001). The combination may produce a new test method which measures the sound pressures outside of the duct and calculates the source impedances indirectly.

7.2 Transfer Impedance of Micro-perforated Panel (MPP) Absorbers

Transfer impedance can be used to characterize most of thin permeable materials such as protective cloths in muffler linings, perforated and micro-perforated panel absorbers, etc. MPP absorbers are novel acoustical materials which can be used as alternatives to traditional absorbing materials such as fibers and foams. Due to pore diameters sub-millimeter in size, MPP absorbers provide acoustic resistance which enhances the sound attenuation. Its acoustic performance is determined by the perforation size, porosity, panel thickness and air cavity depth posterior to it. In current research, a parametric study based on Maa's equation (Maa, 1975) provided directions for manufacturers to control MPP geometric parameters in order to obtain the desired acoustic performance.

For MPP manufactures, cutting circular-shaped perforations is normally accomplished by using either a laser or a drill press (Yoo, 2008). As a result, high manufacturing costs preclude their use in most products. However, lower cost MPP absorbers with irregular slit-shaped perforations are being produced that perform similar. For MPP with irregular slit-shape, geometric parameters such as slit size and porosity are difficult to measure. Thus, it is impossible to correlate the manufacturing parameters to the acoustic performance for MPP with irregular

slit shape. Because of the very reason, the acoustic performance of MPP with irregular slit shape is usually achieved by try-and-error approach which is very time-consuming.

In current research, an inverse method using a nonlinear least square data fitting algorithm was developed to estimate “effective” geometric parameters from measured absorption coefficient data. Both circular-perforation and rectangular-slit models were validated in the algorithm. The “effective” geometric parameters were used to further calculate transfer impedance with good agreement with the measured data. The merit of this approach is that it generates the “effective” geometric parameters based on the acoustic performance when the “actual” geometric parameters are unavailable. Just like the “actual” parameters, these “effective” parameters can be used to direct the manufacturing in order to obtain the desired acoustic performance.

This inverse approach was also used to aid to understand the effect of dust and fluid contamination on the performance of MPP absorbers. Experiments suggest that dust and fluid contamination increase both transfer resistance and reactance. By applying the inverse approach to the measured absorption, the effective parameters of contaminated absorber was obtained. The inverse calculation suggests that dust contamination reduces both the “effective” porosity and perforation size simultaneously, while fluid contamination leads to parallel impedance in the hole through the air and fluid. By understanding the effect and the mechanism behind it, cleaning protocols can be established or MPP absorbers can be designed to function well for known levels of contaminant accumulation.

It is suggested that further effective parameter study could be focused on reducing the “effective” parameters to one: flow resistance of MPP absorbers. The empirical equations that relate flow resistivity and characteristic impedance of porous materials were developed (Wu, 1988). Based on the same concept, an empirical equation can be developed to relate flow resistance and transfer impedance of MPP absorbers.

7.3 Enhancement of MPP Performance in Duct

In the current research, application of MPP absorbers with adjoining air cavity as noise treatment in duct system was investigated. An improvement strategy, partitioning the air cavity, was studied experimentally and numerically. For MPP absorber with and without partitioning, the sound pressures inside the duct was measured and compared. The results indicate that partitioning improves the performance of the absorber by disrupting wave propagation behind the MPP that would be present without it. The effect is particularly noticeable at low frequencies where the acoustic response is resonant in nature. Boundary element analysis was conducted to simulate the effect of the MPP absorbers with air cavity. Analyses were conducted with and without partitioning in the adjoining cavity. The simulation agreed well with experimental results when it was assumed that the MPP could be modeled via a transfer impedance boundary condition. The simulation illustrated that the MPP was most effective when the particle velocity (in the direction normal to the MPP) in the perforations was high.

It is suggested that further MPP work could be focused on HVAC and muffler applications. The impact of partitioning could also be evaluated for engine enclosures, aircraft fuselages and building interiors.

7.4 Application of Moebius Transformation to Impedance Modification

In current research, the influence of modifications of both source and transfer impedances on the system response was studied using the Moebius transformation. It was demonstrated that the Moebius transformation – which maps straight lines and circles in one complex domain to circles in another complex domain – was a mathematical tool that can be employed to aid in determining and understanding the impact of acoustic impedance modifications on a vibro-acoustic system. The Moebius transformation is applicable to

modifications of any parallel or series impedances. Other acoustic elements including termination impedance, parallel impedance, and muffler were modified to study the system response. For the case of parallel impedances, i.e. side branch, the impedance can be most easily adjusted by adjusting the length. For the case of muffler, the modification was achieved by adjusting the length of a simple expansion chamber.

The methodology of the Moebius Transformation warrants further investigation and might be especially helpful if implemented in more advanced duct acoustic optimization schemes. The approach seems to be especially promising to provide intuition in engine exhaust acoustic system design.

REFERENCES

M. Abom and H. Boden, (1988). “Error Analysis of Two-microphone Measurements in Ducts with Flow”, *Journal of the Acoustical Society of America*, Vol. 83, pp. 2429-2438.

S. Allam and M. Abom, (2005). “Acoustic Modeling and Testing of Diesel Particulate Filters”, *Journal of Sound and Vibration*, Vol. 288, pp. 255-273.

S. Allam, Y. Guo, and M. Abom, (2009). “Acoustical Study of Micro-Perforated Plates for Vehicle Applications”, *2009 SAE Noise and Vibration Conference Proceedings*, St. Charles, IL.

J. F. Allard, (1993). *Propagation of Sound in Porous Media: Modelling Sound Absorbing Materials*, Chapman & Hall, London.

H.S. Alves, (1986). *Characterization of noise sources in ducts*, M. Sc. Thesis, University of Calgary

H.S. Alves and A.G. Doige, (1987). “A Three-load Method for Noise Source Characterization in Ducts”, *NOISE-CON 87,* pp. 329–334.

D. Arnold and J. Rogness, (2007). “Mobius Transformation Revealed”, *http://www.ima.umn.edu/~arnold/moebius/.*

R. Astley, (1987). “A comparative note on the effects of local versus bulk reaction models for air moving ducts lined on all sides” *Journal of sound and vibration,* Vol. 117, pp. 191-197.

ASTM E1050 (1998). Standard Test Method for Impedance and Absorption of Acoustical Material Using a Tube, Two Microphones and a Digital Frequency Analysis System.

ASTM C384 (2003). Standard Test Method for Impedance and Absorption of Acoustical Materials by the Impedance Tube Method.

ASTM E2611 (2009). Standard Test Method for Measurement of Normal Incidence Sound Transmission of Acoustical Materials Based on the Transfer Matrix Method.

N. Atalla, F. Sgard, (2007). “Modelling of perforated plates and screens using rigid frame porous models”, *Journal of Sound and Vibration*, Vol. 303, pp. 195–208.

B. Bauer, (1977). “Impedance Theory and Measurement on Porous Acoustic Liners”, *Journal of Aircraft*, Vol. 14, pp. 720-728.

M. Bockhoff, (2007). “Design of low noise machinery”, Chapter 66 In: M. Crocker, Editor, *Handbook of Noise and Vibration Control*, Wiley, New Jersey pp. 794–804.

H. Boden and M. Abom, (1986). “Influence of Errors on the Two-microphone Method for Measuring Acoustic Properties in Ducts”, *Journal of the Acoustical Society of America*, Vol. 79, pp. 541-549.

H. Boden, (1988). “Error Analysis for the Two-load method used to Measure the Source Characteristics of Fluid Machines”, *Journal of Sound and Vibration*, Vol.126, pp. 173-177.

H. Boden, (1991). “The Multiple Load Method for Measuring the Source Characteristics of Time-variant Sources”, *Journal of Sound and Vibration*, Vol.148, pp.437-253.

H. Boden, (1992). “Characterisation of IC-engines as Sources of Exhaust and Intake Noise”, *Proceedings of the 25th ISATA Conference on Mechatronics*.

H. Boden and M. Abom, (1995). “Modelling of Fluid Machines as Sources of Sound in Duct and Pipe Systems”, *Acta Acoustica*, Vol. 3, pp.549-560.

H. Boden and R.Glav, (2007). “Exhaust and Intake Noise and Acoustical Design of Mufflers and Silenecers”, in *Handbook of Noise and Vibration Control*, ed. by Crocker, M. J., John Wiley & Sons.

H. Boden, (2007). “Recent Advances in IC-Engine Acoustic Source Characterization”. *Proceedings of the ICSV14*, Cairns, Australia,

P. Bonfiglio and F. Pompoli, (2008). “A single measurement approach for the determination of the normal incidence transmission loss”, *Journal of the Acoustical Society of America*, Vol. 124, pp. 1577-1583.

V. Chew, (1966). “Confidence, prediction, and tolerance regions for the multivariate normal distribution”, *Journal of American Statistical Association*, Vol. 61, pp. 605-617.

J. Chuang, (1978). “Cross-spectral Method of Measuring Acoustic Intensity without Error caused by Instrument Phase Mismatch”, *Journal of the Acoustical Society of America*, Vol. 64, pp. 1613-1616.

J. Y. Chung and D. A. Blaser, (1980). "Transfer function method of measuring in-duct acoustic properties. I. Theory, II. Experiment ", *Journal of the Acoustical Society of America*, Vol. 68, pp. 907–913.

A. Coffman and M. Frantz, (2003). “Ellipses in the Inversive Plane”, *MAA Indiana Section Meeting Proceedings*.

T. F. Coleman, Y. Li, (1994). “On the Convergence of Reflective Newton Methods for Large-Scale Nonlinear Minimization Subject to Bounds”, *Mathematical Programming*, Vol. 67, pp. 189-224.

T. F. Coleman, Y. Li, (1996). “An Interior, Trust Region Approach for Nonlinear Minimization Subject to Bounds”, *SIAM Journal on Optimization*, Vol. 6, pp. 418–445.

R. Corin and L. Weste, (2005). “Sound of silence”, *iVT International*, pp. 105-107.

J. Coulon and A. Garcia, (1993). “Some Remarks about the Four-Load Method for Measuring Source Impedance”, *Journal of Sound and Vibration*, Vol. 164, pp. 375-379.

I.B. Crandall, (1927). *Theory of Vibrating Systems and Sound*, D. Van Nostrand & Co. Inc., New York.

M. J. Crocker and N. I. Ivanov, (1993). *Noise and Vibration Control in Vehicles*, Politechnica, St. Petersburg.

M. Crocker, (2007). “Introduction to Principles of Noise and Vibration Control”, Chapter 54 in: M. Crocker, Editor, *Handbook of Noise and Vibration Control*, Wiley, New Jersey pp. 649-667.

A. Cummings, (1986). “The effects of grazing turbulent pipe-flow on the impedance of an orifice,” *Acustica*, Vol. 61, pp. 233–242.

Davies P.O.A.L, (1991). “Transmission matrix representation of exhaust system acoustic characeristics”, *Journal of Sound and Vibration*, Vol. 151, pp. 333-338

P. Dean, (1976). “On the In-situ Control of Acoutsic Liner Attenuation”, *Transactions of the ASME, Journal of Engineering for Power*.

J. Demmel, (1997). Linear Equation Solving, Chap. 2 in *Applied Numerical Linear Algebra*, SIAM.

L. Desmons and J. Hardy, (1994). “A Least Squares Method for Evaluation of Characteristics of Acoustical Sources”, *Journal of Sound and Vibration*, Vol. 175, pp. 365-376.

L. Desmons, J. Hardy, and Y. Auregan, (1995). “Determination of the Acoustical Source Characterisristics of an Internal Combustion Engine by Using Several Calibrated Loads”, *Journal of Sound and Vibration,* Vol. 179, pp. 869-878.

G. T. S. Done and A. D. Hughes, (1975). “The response of a vibrating structure as a function of vibrating parameters,” *Journal of Sound and Vibration*, Vol. 38, pp. 255-266.

K. Edge and D. Johston, (1990). “The ‘Secondary Source’ Method for the Measurement of Pump Pressure Ripple Characteristics. I. Description of Method, II. Experimental Results”, *Proceedings of the Institution of Mechanical Engineers* , Vol. 204, pp. 33-46.

D. Egolf and R. Leonard, (1977). “Experimental Scheme for Analyzing the Dynamic Behavior of Electroacoustic Transducers”, *Journal of the Acoustical Society of America*, Vol. 62, pp. 1013–1023.

T. Elnady and H. Boden, (2003). “On the Modeling of the Acoustic Impedance of Perforates with Flow”, *9th AIAA/CEAS Aeroacoustics Conference Proceedings*, Hilton Head, SC.

F. Fahy, (2001). *Foundations of Engineering Acoustics*. Academic Press, London.

B, Fenech, (2004). *Damping the Acoustic Modes in a Closed Cavity Using a Micro-Perforated Plate*, Master Thesis, Technical University of Denmark

B. Fenech, G. Keith, F. Jacobsen, (2006). “The use of microperforated plates to attenuate cavity resonances”, *Journal of the Acoustical Society of America*, Vol. 120, pp. 1851-1858.

H. V. Fuchs, X. Zha, (1997). “Acylic-glass Sound Absorbers in the Plenum of the Deutscher Bundestag”, *Applied Acoustics*, Vol. 51, pp. 211-217.

A. Galaitsis and E. Bender, (1975). “Measurement of the Acoustic Impedance of an Internal Combustion Engine (A)”, *Journal of the Acoustical Society of America*, Vol. 58, S8.

R. Glav and M. Abom, (1997). “A General Formalism for Analyzing Acoustic Two-port Networks”, *Journal of Sound and Vibration*, Vol. 202, pp. 739-747.

D. Herrin, Z. Tao, A. Carter, and J. Liu, (2006). “Using Numerical Methods to Analyze Multicomponent HVAC Systems”, *ASHRAE Transaction*, Vol. 112.

R. Hota and M. Munjal, (2008). "Intake source characterization of a compression ignition engine: Empirical expressions", *Noise Control Engineering Journal*, Vol. 56, pp. 92-106.

R. Hota and M. Munjal, (2009). “Aero-acoustic Source Characteristics of a Compression Ignition Engine: Empirical Expressions Obtained by Means of a Numerical Multi-Load Method”, *International Journal of Aeroacoustics.*

R. Hota and M. Munjal, (2010)." Acoustic Source Characteristics of the Exhaust and Intake Systems of a Spark Ignition Engine", *Proceedings of Internoise 2010*, Lisbon, Portugal.

N. Hillereau, A. A. Syed, E. J. Gutmark, (2005). “Measurements of the acoustic attenuation by single layer acoustic liners constructed with simulated porous honeycomb cores”, *Journal of Sound and Vibration*, Vol. 286, pp. 21-36.

J. Ih and K. Peat, (2002). “On the Causes Negative Source Impedance in the Measurement of Intake and Exhaust Noise Sources”, *Applied Acoustics*, Vol. 63, pp. 153-171.

U. Ingard and T. Dear, (1985). “Measurement of Acoustic Flow Resistance”, *Journal of Sound and Vibration,* Vol. 103, pp. 567-572.

U. Ingard, (1953). “On the theory and design of acoustic resonators”, *Journal of the Acoustical Society of America*, Vol.25, pp. 1037-1062.

U. Ingard and H. Ising, (1967). ‘‘Acoustic nonlinearity of an orifice,’’ *Journal of the Acoustical Society of America*, Vol. 42, pp. 6–17.

U. Ingard, (2010). *Noise Reduction Analysis*, Jones and Barlett Publishers, London, United Kingdom, pp. 389-395.

ISO 10534-1, (1996), Acoustics—Determination of sound absorption coefficient and impedance in impedance tubes—Part 1: Method using standing wave ratio.

ISO 10534-2, (1998), Acoustics—Determination of sound absorption coefficient and impedance in impedance tubes—Part 2: Transfer-function method.

ISO/TR 11688-2, (1998), Acoustics—Recommended Practice for the Design of Low-Noise Machinery and Equipment—Part 2: Introduction to the Physics of Low-Noise Design.

S. Jang and J. Ih, (2000). “Refined Multiload Method for Measuring Acoustical Source Characteristics of an Intake or Exhaust System”, *Journal of the Acoustical Society of America*, Vol. 107, pp. 3217.

S. Jang and J. Ih, (2002). “On the Selection of Loads in the Multiload Method for Measuring the Acoustic Source Parameters of Duct Systems”, *Journal of the Acoustical Society of America*, Vol. 111, pp. 1171–1176.

W. Jiang. (2006). “Some numerical experimental study of microperforated panel acoustic absorbers with heterogeneous cavities” *Proceedings of ICSV13*, Vienna, Austria.

M. Kathuriya and M. Munjal, (1979). “Experimental Evaluation of the Aeroacoustic Characteristics of a Source of Pulsating Gas Flow”, *Journal of the Acoustical Society of America*, Vol. 65, pp. 240–248.

L. Kinsler, A. Frey, A. Coppens and J. Sanders. (1999). *Fundamentals of Acoustics*, John Wiley and Sons, New York, pp. 107-112

M. Knutsson and H. Boden, (2007). “IC-Engine Intake Acoustic Source Data from Non-Linear Simulations”, *Proceedings of SAE 2007 Noise and Vibration Conference and Exhibition*, St. Charles, IL.

J. W. Kooi and S. L. Sarin, (1981). “An experimental study of the acoustic impedance of Helmholtz resonator arrays under a turbulent boundary layer,” *AIAA 81–1998*.

P. K. Kundu and I. M. Cohen (2004), *Fluid Mechanics*, 3rd edition, Elsevier Academic Press, San Diego.

J. Lavrentjev, H. Boden, and M. Abom, (1992). “A Linearity Test for Acoustic One-port Sources”, *Journal of Sound and Vibration*, Vol.155, pp. 534-539.

S. Lee and J. Ih, (2003). “Empirical model of the acoustic impedance of a circular orifice in grazing mean flow”, *Journal of the Acoustical Society of America*, Vol. 114, pp. 98-113.

D. Lee and Y. Kwon, (2004). “Estimation of the Absorption Performance of Multiple Layer Perforated Panel Systems by Transfer Matrix method”, *Journal of Sound and Vibration,* Vol. 278, pp. 847-860.

G. Li, C. K. Mechefske, (2010). “A comprehensive experimental study of micro-perforated panel acoustic absorbers in MRI scanners”, *Magn. Reson. Mater. Phy.*, Vol. 23, pp. 177–185.

J. Liu, D. W. Herrin, A. F. Seybert, (2007). “Application of micro-perforated panels to attenuate noise in a Duct”. *SAE 2007 transactions journal of passenger cars: mechanical systems* 2007-01-2196; pp. 1629-1633.

J. Liu, (2008). “Absorbing Materials and Microperforated Panels”, Internal report at Vibro-Acoustic Consortium Meeting, Lexington, KY.

J. Liu and D. Herrin, (2009). “Load Effect on Source Impedance Measurement Accuracy”, *Proceedings of SAE 2009 Noise and Vibration Conference and Exhibition*, St. Charles, IL.

J. Liu, D. W. Herrin, (2010). “Enhancing Micro-perforated Panel Attenuation by Partitioning the Adjoining Cavity”, *Applied Acoustics*, Vol. 71, pp. 120-127.

J. Liu, D.W. Herrin, (2011). “Effect of Contamination on Acoustic Performance of Microperforated Panels”, *2011 SAE Noise and Vibration Conference Proceedings*, 11NVC-0211, Grand Rapids, MI.

D. Y. Maa, (1975). “Theory and design of Microperforated-panel sound-absorbing construction”, *Scientia Sinica* XVIII, pp. 55-71.

D. Y. Maa, (1996). “Microperforated Panel at High Sound Intensity”, *Shengxue Xuebao/Acta Acustica,* Vol. 21, pp. 10-14 (in Chinese).

D.Y. Maa, (1997). “Microperforated-panel wideband absorbers”, *Noise Control Engineering Journal*, Vol. 29, pp. 77-84.

D. Y. Maa, (1998). “Potential of Microperforated Panel Absorber”, *Journal of the Acoustical Society of America*, Vol. 104, pp. 2861-2866.

D. Y. Maa, (2000). “Theory of microslit absorbers”, *Acta Acustica*, 2000-06.

G. Mailing, (2007). “Noise”. In: M. Crocker, Editor, *Handbook of Noise and Vibration Control*, Wiley, New Jersey. pp. 794–804.

F. Masson, P. Kogan, and G. Herrera, (2008). “Optimization of muffler transmission loss by using microperforated panels,” *FIA2008*, Buenos Aires.

Matlab Users Manual, Mathworks, (2009).

F.P. Mechel, P.M. Mertens and W.A. Schilz, (1965). “Research on sound propagation in sound absorbent ducts with superimposed air streams”, *AMRL-TR-65-53*.

T. Melling, (1973). “The acoustic impedance of perforates at medium and high sound pressure levels,” *Journal of Sound and Vibration*, Vol. 29, pp.1–65.

T. Melling, (1973). “An impedance tube for precision measurement of acoustic impedance and insertion loss at high sound pressure levels”, *Journal of Sound and Vibration*, Vol. 28, pp. 23–54.

C. Morfey. (2001). *Dictionary of Acoustics*, Academic Press, London.

P.M. Morse and K.U. Ingard, (1968). *Theoretical Acoustics*, McGraw Hill, New York, pp. 467–607.

M.L.Munjal, (1987). *Acoustics of ducts and mufflers*, Wiley, New York,

M. L. Munjal and A. G. Doige, (1990). "Theory of two source-location method for direct experimental evaluation of the four-pole parameters of an aeroacoustic element," *Journal of Sound and Vibration*, Vol. 141, pp. 323–333.

M.L. Munjal, (2006). “Passive Silencers”, in *Noise and Vibration Control Engineering: Principles and Applications*, ed. By I. Ver and L. Beranek, John Wiley & Sons.

T. Needham, (1997). *Visual Complex Analysis*, Clarendon Press, Oxford.

J. Pan, R. Ming and J. Guo, (2004). “Wave Trapping Barriers,” *Proceedings of ACOUSTICS 2004*, Gold Coast, Australia.

K. Peat and J. Ih, (2001). “An Analystical Investigation of the Indirect Measurement Method of Estimating the Acoustic Impedance of a Time-varying Source”, *Journal of Sound and Vibration*, Vol. 244, pp. 821-835.

M. Prasad and M. Crocker, (1983). “Acoustical Source Characterization Studies on a Multi-cylinder Engine Exhaust System”, *Journal of Sound and Vibration*, Vol. 90, pp. 479-490.

M. Prasad, (1987). “A Four Load Method for Evaluation of Acoustical Source Impedance in a Duct”, *Journal of Sound and Vibration*, Vol. 114, pp. 347-356.

J. Premo, (1999). “The Application of a Time-domain Model to Investigate the Impedance of Perforate Liners including the Effects of Bias Flow”, *AIAA 99-1876*.

H. Rammal and M. Abom, (2007). “Characterization of air terminal device noise using acoustic 1-port source models”, *Journal of Sound and Vibration*, Vol. 300, pp. 727-743.

K. N. Rao and M. L. Munjal, (1986). ‘‘Experimental evaluation of impedance of perforate with grazing flow,’’ Journal of Sound and Vibration, Vol. 108, pp. 283–295.

Lord Rayleigh, (1877, reissued 1940). *Theory of Sound Vol. II*, Macmillan & Co. Ltd., London.

M. Ren and F. Jacobsen, (1993). “A Method of Measuring the Dynamic Flow Resistance and Reactance of Porous Materials”, *Appl. Acoust*., Vol. 39, pp. 265–276.

A. C. Rencher, (1995). *Methods of Multivariate Analysis*. New York, USA: Wiley: pp. 339-341.

D. Ross and M. Crocker, (1983). “Measurement of the acoustic internal source impedance of an internal combustion engine”, *Journal of the Acoustical Society of America*, Vol. 74, pp. 18-27.

T. Schultz, M. Sheplak, L. Cattafesta, (2007). “Uncertainty Analysis of the Two-microphone Method”, *Journal of Sound and Vibration*, Vol. 304, pp. 91-109.

T. Schultz, M. Sheplak, L. Cattafesta, (2007). “Multivariate uncertainty analysis and application to the frequency response function estimate”, *Journal of Sound and Vibration*, Vol. 305, pp. 116-133.

A. F. Seybert and D. F. Ross, (1977). "Experimental determination of acoustic properties using a two-microphone random-excitation technique," *Journal of the Acoustical Society of America*, Vol. 61, pp. 1362–1370.

A.F. Seybert, B. Soenarko, (1981). “Error Analysis of Spectral Estimates with Application to the Measurement of Acoustic Parameters Using Random Sound Fields in Ducts”, *Journal of the Acoustical Society of America*, Vol. 69, pp. 1190–1199.

A.F. Seybert, (2000). “Fundamentals of Linear Acoustics”, Chap. 1 in *Boundary Element Acoustics: Fundamentals and Computer Codes*, ed. by T. W. Wu, WIT Press, Southampton, UK.

L.J. Sivian, (1935). “Acoustic impedance of small orifices”, *Journal of the Acoustical Society of America*, Vol. 7, pp. 94-101.

B. Soenarko, (1980). *Error analysis of spectral estimates*, Master Thesis, University of Kentucky.

B. H. Song and J. S. Bolton, (2000). "A transfer matrix approach for estimating the characteristic impedance and wave number of limp and rigid porous materials," *Journal of the Acoustical Society of America*, Vol. 107, pp. 1131–1152.

A. Sreenath and M. Munjal, (1970). “Evaluation of Noise Attenuation Due to Exhaust Mufflers”, *Journal of Sound and Vibration*, Vol. 12, pp. 1-19.

M. Stinson and E. Shaw, (1985). “Acoustic Impedance of Small, Circular Orifices in Thin Plates”, *Journal of the Acoustical Society of America*, Vol. 77, pp. 2039-2042.

J. Sullivan, (1979). “A method of modeling perforated tube muffler components. I. Theory, II. Applications”, *Journal of the Acoustical Society of America*, Vol. 66, pp. 772-788.

K. S. Sum, J. Pan, and S. Z. Peng, (2006). “Use of parallel Microperforated panel subabsorbers for noise control in ducts”, *Proceeding of ICSV13*, Vienna, Austria.

Z. Tao, B. Zhang, D. Herrin, and A. Seybert, (2005). “Prediction of Sound-Absorbing Performance of Micro-Perforated Panels Using the Transfer Matrix Method”; *2005 SAE Noise and Vibration Conference Proceedings*, Traverse City, MI.

Z. Tao, J. Liu, D. W. Herrin, A. F. Seybert and D. Kato, (2007). “Measurement of Source Impedance for an Intake System”, *INTER-NOISE 2007*, Istanbul, Turkey.

M. G. Tehrani, W. Wang, C. Mares, and J. E. Mottershead, (2006). “The generalized Vincent circle in vibration suppression,” *Journal of Sound and Vibration*, Vol. 292, pp. 661-675.

G. Thurston, (1952). “Periodic Fluid Flow through Circular Tubes,” *Journal of the Acoustical Society of America*, Vol. 24, pp. 653-656.

M. Toyoda, D. Takahashi, (2008). “Sound transmission through a microperforated-panel structure with subdivided air cavities”, *Journal of the Acoustical Society of America*, Vol. 124, pp. 3594-3603.

H. Utsuno, T. Tanaka, T. Fujikawa, and A. F. Seybert, (1989). “Transfer function method for measuring characteristic impedance and propagation constant of porous materials,” *Journal of the Acoustical Society of America*, Vol. 86, pp. 637–643.

N. Vlahopoulos, (2000). “Indirect variational boundary element method in acoustics”, Chap. 6 in *Boundary Element Acoustics: Fundamentals and Computer Codes*, ed. by T. W. Wu, WIT Press, Southampton, UK.

K. Wood, (2003). Process of forming a microperforated polymeric film for sound absorption, U.S. Patent No. 6617002.

M. Wu. (1997). “Micro-perforated Panels for Duct Silencing”. *Noise Control Engineering Journal*, Vol. 45, pp. 69-77.

Q. Wu. (1988). “empirical relations between acoustical properties and flow resistivity of porous plastic open-cell foams”, Applied Acoustics, Vol. 25, pp. 141-148.

T. W. Wu, P. Zhang and C. Y. R. Cheng, (1998). “Boundary Element Analysis of Mufflers with an Improved Method for Deriving the Four-pole Parameters”, *Journal of Sound and Vibration*, Vol. 217, pp. 767-779.

T. W. Wu, C. Y. R. Cheng and Z. Tao, (2003). “Boundary Element Analysis of Packed Silencers with Protective Cloth and Embedded Thin Surfaces,” *Journal of Sound and Vibration*, Vol. 261, pp. 1-15.

M. Yairi, K. Sakagami, M. Morimoto, A. Minemura, (2005). “Acoustical Properties of Microperforated Panel Absorbers with Various Configurations of the Back Cavity”, *Proceeding of ICSV12*, Lisbon, Portugal.

T. Yoo, (2008). *The Modeling of Sound Absorption by Flexible Micro-perforated Panels*, Doctoral Dissertation, Purdue University.

Z. M. Zhang, X. T. Gu, (1998). “The theoretical and application study on a double layer Microperforated sound absorption structure”, *Journal of Sound and Vibration*, Vol. 215, pp. 399-405.

C. Zwikker and C.W. Kosten, (1949). *Sound Absorbing Materials*, Elsevier Publishing Co., New York.

VITA

Jinghao Liu was born in Shandong, China on March 10, 1981. He received the degree of Bachelor of Science in Mechanical Engineering from Shandong University of Technology, China in 2002. Subsequently, He received his Master of Science in Mechanical Engineering from Chongqing University, China in 2005.

In August 2005, he enrolled in the graduate school at the University of Kentucky. During his graduate years at the University of Kentucky, he has published 9 Journal articles (first author on 4) and 14 conference proceeding articles (first author on 6). His technical paper was awarded the Outstanding Student Paper Award at the 2008 National Conference on Noise Control Engineering (NOISE-CON). In April 2010, He was named Outstanding Graduate Student of the Department of Mechanical Engineering. Additionally, He received Leo Beranek Student Medal for Excellence in the Study of Noise Control from the Institute of Noise Control Engineering (INCE) in May, 2011.

Jinghao Liu